

**SYNTHESIS AND PROPERTIES OF  
NANOPARTICULATE  
TITANIUM DIOXIDE COMPOUNDS**

**By**

**MOTLALEPULA ISAAC BUTHELEZI**



A dissertation submitted in partial fulfillment of the requirements  
For the degree of Masters of Science in the Department of Chemistry,  
University of the Western Cape

**Supervisor:** Prof. D.L. Key (*University of the Western Cape*)

**2010**

# DECLARATION

I declare that “Synthesis and properties of nanoparticulate titanium dioxide compounds” is my own work, that is has not been submitted for any degree or examination in any other university, and that all sources I have used or quoted have been indicated and acknowledged by complete references.



Signature: .....

# ACKNOWLEDGEMENTS

I would really like to thank **Prof. David L. Key** for guiding me during the course of my M.Sc. I am very grateful for the time you have dedicated to me, your ideas, encouragements, great efforts suggestions and useful discussions. I highly appreciated friendly environment in which you have welcomed me. All this has been of great hard-work, support, assisting me to face and solve the challenges of my project, which I do not think I would have completed it otherwise.

I would like to extend my gratitude to **Dr. Lindiwe Khotseng, Dr. Tesfaye Waryo, Dr.Salam Titinchi and Dr. Hanna Abbo** for good guidance and Knowledge. Furthermore, to thank **Gauthier Okolongo, Julian Key, Samantha Hayward, Zelo Mangombo, Ghouwaa Philander** and other colleagues for having been very good officemates, always available for help, suggestions or just a laugh when a break was needed. I thank all my friends for motivation and support throughout the academic years.

Since this work is the result of collaborations within different departments of the University of Western Cape and other research institutes, I would like to express my appreciation to the following people:

- Mr. Adrian Josephs**, Physics department (*UWC*), for SEM, TEM and HR-TEM measurements.
- Dr Remy Bucher**, ithemba lab for XRD.
- Mr Mandla Msimanga and Dr Carlos Pineda**, ithemba lab, for RBS.
- Dr Ray Barlow**, Marine Scientist III for UV/Vis DRS.
- **Prof. Hendrik Swart**, Physics department (*UOVS*), for XPS.
- Technicians and Staff members**, Chemistry Department (*UWC*), for your assistance.

Special great thanks go to my mother (**Maria Buthelezi**) for all she has done for me and everything she have taught me. The National Research Foundation is acknowledged for financial assistance. Finally, I would like to thank Almalthy God who has made all this possible by bringing the above mentioned persons into my life.

# TABLE OF CONTENTS

## Contents

DECLARATION .....	ii
ACKNOWLEDGEMENTS.....	iii
TABLE OF CONTENTS .....	iv
KEYWORDS.....	viii
ABSTRACT .....	ix
LIST OF ABBREVIATIONS.....	xi
LIST OF FIGURES .....	xiv
LIST OF TABLES .....	xviii
CHAPTER 1 .....	1
INTRODUCTION.....	1
1Background. ....	1
1.1 Occurrence and uses of titanium dioxide. ....	1
1.2 Properties of TiO <sub>2</sub> . ....	2
(a) Structural forms of TiO <sub>2</sub> . ....	2
(b) Semiconductor properties of TiO <sub>2</sub> . ....	5
(i) Some properties of semiconductors. ....	5
(ii) TiO <sub>2</sub> an n-type Semiconductor. ....	11
(c) Photocatalytic properties of TiO <sub>2</sub> . ....	15
(i) Photocatalysis. ....	17



(ii) TiO <sub>2</sub> as a photocatalyst. ....	19
1.3 Reducing the band gap of TiO <sub>2</sub> . ....	22
1.4 Reduction of TiO <sub>2</sub> .....	24
(a) Photochemical reduction. ....	25
(b) Electrochemical reduction.....	26
(c) Cyclic voltammetry studies in non-aqueous solution. ....	27
1.5 Nanoscience and nanomaterials.....	30
1.6 Nanostructured titanium dioxide .....	32
1.7 Titanium Dioxide Nanotubes. ....	33
1.8 Fabrication of TiO <sub>2</sub> nanotubes.....	34
(a) Anodization of titanium. ....	34
(b) Other methods of synthesis of TiO <sub>2</sub> nanotubes.....	36
1.9 Aim and objectives .....	37
CHAPTER 2 .....	38
EXPERIMENTAL METHODS .....	38
2.1 Chemicals and gases. ....	38
2.2 Preparation of TiO <sub>2</sub> nanotubes.....	39
2.3 Electrochemical reduction of TiO <sub>2</sub> . ....	42
2.3.1 Using electrochemical reduction. ....	42
2.3.2 Growth of TiO <sub>2</sub> nanotubes on a Ti electrode to be used .....	43
in cyclic voltammetry studies. ....	43
2.3.3 Cyclic Voltammetry. ....	44
2.3.4 CV studies of TiO <sub>2</sub> nanotubes deposited on a Ti .....	45
electrode. ....	45
2.4 Photochemical reduction of TiO <sub>2</sub> Samples. ....	46
2.5 Doping procedure of TiO <sub>2</sub> nanotubes. ....	48
2.6 Scanning Electron Microscopy.....	48
2.6.1 Construction of a typical SEM.....	50
2.6.2 Preparation of TiO <sub>2</sub> nanotubes for SEM studies. ....	52

2.7 Transmission Electron Microscopy. ....	52
2.7.1 Preparation of TiO <sub>2</sub> nanotubes for TEM studies.....	54
2.8 X-Ray Diffraction. ....	54
2.8.1 Preparation of TiO <sub>2</sub> nanotubes for XRD studies.....	56
2.9 Rutherford Back Scattering. ....	56
2.9.1 Preparation of TiO <sub>2</sub> nanotubes for RBS studies.....	57
2.9.2 Calculation Method based on RBS. ....	58
2.10 Measurement of photocatalytic activity. ....	60
2.10.1 Methods of calculation. ....	61
2.11 UV/Vis Diffuse reflectance spectrophotometry. ....	62
2.11.1 Preparation of TiO <sub>2</sub> nanotubes for UV/Vis DRS. ....	64
2.12 X-ray photoelectron spectroscopy. ....	64
2.12.1 Preparation of TiO <sub>2</sub> nanotubes for XPS studies.....	66
2.13 Elemental analysis. ....	67
2.13.1 Preparation of TiO <sub>2</sub> nanotubes for elemental analysis. ....	67
2.14 Anodization of a titanium alloy. ....	68
CHAPTER 3 .....	69
Results and Discussion .....	69
3.1 SEM and TEM characterization of TiO <sub>2</sub> samples. ....	69
3.1.1 Non-reduced samples.....	69
3.1.1.1 Mechanistic model of TiO <sub>2</sub> nanotubes formation.....	75
3.1.2 Reduced samples.....	80
3.1.2.1 Effect of electrolyte composition in reduction process.....	89
3.2 XRD measurements. ....	91
3.3 Cyclic voltammetry (CV) studies. ....	94
3.3.1 CV in non aqueous solution.....	94
3.3.2 CV in aqueous solution.....	101
3.4 RBS Characterization.....	109
3.5 UV/Vis Diffuse Reflectance spectroscopy (DRS).....	111

Measurements.....	111
3.6 XPS Measurements.....	116
3.7 Light element analysis. ....	118
3.8 Photocatalytic efficiency measurements.....	122
CHAPTER 4.....	126
Conclusion .....	126
REFERENCES .....	128



# KEYWORDS

Titanium dioxide

Nanotube

Anodic oxidation

Electrochemical reduction

Photoelectrochemical reduction

Amorphous

Annealing

Band gap

Voltammogram

Conductivity



# ABSTRACT

An electrolytic cell was designed and constructed for the preparation of TiO<sub>2</sub> nanotubes. Conditions of anodic oxidation were established to reproducibly prepare TiO<sub>2</sub> nanotubes of average length 35-50 μm vertically orientated relative to the plain of a pure titanium metal sheet. A non-aqueous solution of ethylene glycol containing small percentage of ammonium fluoride was used as the electrolyte with an applied voltage of 60 V.

The morphology and dimensions of the nanotube arrays were studied by scanning (SEM) and transmission (TEM) electron microscopy. The effect of calcination under different conditions of temperature and atmosphere (nitrogen, argon and air) were assessed by both X-ray diffraction (XRD) and cyclic voltammetry (CV). Cyclic voltammetry studies were made possible by construction of a specially designed titanium electrode upon which the nanotubes were prepared. CV studies established a positive correlation between crystallinity and conductivity of the nanotubes.

Doping of the nanotubes with nitrogen and carbon was established by elemental analysis, X-ray photoelectron spectroscopy (XPS) and Rutherford back scattering (RBS). The effect of non-metal doping on the band gap of the TiO<sub>2</sub> nanotubes was investigated by diffuse reflectance spectroscopy (DRS).

Reduction of the nanotubes was carried out both photochemically and electrochemically in non-aqueous solution. Electrochemical reduction was investigated by CV to probe the nature of the blue colour of the nanotubes resulting from reduction

Lower valences states of titanium ( $\text{Ti}^{3+}$  and possibly  $\text{Ti}^{2+}$ ) are produced on reduction which enhances conductivity. Both reduction and increased crystallinity produce surfaces intermediate levels in the band gap region.

The photocatalytic efficiency of the reduced nanotubes appears to increase as compared to that of  $\text{TiO}_2$  powder (Degussa P25) consistent with nitrogen doping causing a narrowing of the band gap.



# LIST OF ABBREVIATIONS

Å	Angstrom [ $10^{-10}$ m]
A	Area of the Cell [ $m^2$ ]
A	Ampere
ACN or MeCN	Acetonitrile
Ag/AgCl	Silver/silver chloride reference electrode (s.s.c.e)
Ar	Argon
Ar <sup>+</sup>	Argon ion
at.%	Atomic percentage
C	Carbon
CO	Carbon monoxide
CV	Cyclic Voltammetry
d	Barrier Layer Thickness [nm]
D	Nanotube Inner Diameter
DCM	Dicloromethane
DMF	N, N-dimethylformamide
EA	Elemental Analyser
EDX	Energy Dispersive X-ray Spectroscopy
EG	Ethylene Glycol
EtOH	Ethanol
eV	Electron volt
F	Fluorine
F <sup>-</sup>	Fluorine ion
H <sup>+</sup>	Hydrogen ion
H <sub>2</sub>	Hydrogen
He	helium
He <sup>+</sup>	helium ion

H <sub>2</sub> O	Water or Ultra pure water
HRTEM	High Resolution Transmission Electron Microscopy
K <sub>3</sub> [Fe(CN) <sub>6</sub> ]	Potassium ferricyanate
KCl	Potassium Chloride
L	Nanotube Length
Li <sup>+</sup>	Lithium ion
M	Molar concentration [moles/l]
M/MO	Metal-Metal Oxide Interface
MB	Methylene Blue
MeOH	Methanol
Mg <sup>2+</sup>	Magnesium ion
MO/E	Metal Oxide-Electrolyte Interface
N <sub>2</sub>	Nitrogen
Na <sup>+</sup>	Sodium ion
NH <sub>4</sub> F	Ammonium fluoride
nm	Nanometer [10 <sup>-9</sup> m]
NO	Nitrogen monoxide
NTs	Nanotubes
O <sub>2</sub> <sup>2-</sup>	Peroxide ion
O <sup>2-</sup>	Oxide ion
O <sub>2</sub>	Oxygen
OH <sup>-</sup>	Hydroxyl ion
P	Phosphorus
Pt	Platinum
Q <sub>m</sub>	Maximum concentration of reduced sites
RBS	Rutherford Backscattering Spectroscopy
Redox	Reduction-oxidation
SC	Semiconductor
SC/E	Semiconductor-Electrolyte Interface
SEM	Scanning Electron Microscopy

Si	Silicon
S	Sulfur
SO <sub>2</sub>	Sulfur dioxide
SXI	Scanning X-ray Image
TBAP	Tetrabutylammonium perchlorate
TEM	Transmission Electron Microscopy
Ti (OH) <sub>4</sub>	Titanium tetrahydroxide
Ti	Titanium
Ti/TiO <sub>2</sub>	Titanium dioxide on Titanium metal as substrate
Ti <sup>4+</sup>	Titanium ion
TiF <sub>6</sub> <sup>2-</sup>	Titanium hexafluoride complex ion
TiO <sub>2</sub>	Titanium dioxide
TiO <sub>2</sub> nanotubes	Titanium dioxide Nanotubes (TNTs)
UHP	Ultra high purity
UV	Ultraviolet
V	Volt
V <sub>diss.</sub>	Dissolution rate of the anodic oxide
vol.%	Volume percentage
V <sub>ox</sub>	Oxidation rate (rate of formation of the anodic oxide)
W	Nanotube Wall Thickness
W	Watt
wt.%	Weight percentage
XPS	X-ray Photoelectron Spectroscopy
XRD	X-ray Diffraction
μm	Micrometer [10 <sup>-6</sup> m]

# LIST OF FIGURES

<b>Figure 1.1</b> TiO <sub>2</sub> different crystal structures: rutile (a), anatase (b) and brookite(c) .....	4
<b>Figure 1.2</b> Energy level diagrams illustrating valance band (vb), conduction band (cb), fermi energy(EF ) and energy gap(Eg) of a semiconductor .....	6
<b>Figure 1.3</b> Energy level diagrams illustrating the band bending effect in of p-type semiconductor .....	8
<b>Figure 1.4</b> Energy level diagrams illustrating the band bending effect in of n-type semiconductor .....	10
<b>Figure 1.5</b> Mechanism of photocatalysis using energy from the light .....	14
<b>Figure 1.6</b> Electrochemical system that includes electron transfer.....	28
<b>Figure 2.1</b> Diagram illustrating the components of the horizontally orientated anodising unit. The system includes a two electrode cell and a power supply. ....	41
<b>Figure 2.2</b> Diagram illustrating the components of the horizontally orientated anodising unit. The system includes a two electrodes cell and a power supply.....	43
<b>Figure 2.3</b> Diagram illustrating the components of CV apparatus. The system includes Autolab electrochemical system in conjunction with (BAS instruments) a three-electrode system and personal computer for data storage and processing. ....	46
<b>Figure 2.4</b> Diagram illustrating the components of photoreduction apparatus. ....	47
<b>Figure 2.5</b> Schematic of a SEM .....	50
<b>Figure 2.6</b> The signals generated by a primary electrons beam-specimen interaction in SEM ...	51
<b>Figure 2.7</b> Bruker-Axs D8 advance XRD. ....	55
<b>Figure 3.1</b> (Sample S1) of TiO <sub>2</sub> nanotubes, (a) View of face which was not in contact with Ti substrate (top view), (b) Cross sectional view, right side edge in image was that attached to Ti substrate. (c)View of face that was attached to Ti substrate (bottom view).....	70
<b>Figure 3.2</b> (Sample S2) of TiO <sub>2</sub> nanotubes, (a) View of face which was not in contact with Ti substrate (top view), (b) Cross sectional view, (c)View of face that was attached to Ti substrate (bottom view).....	71

<b>Figure 3.3</b> Show SEM images of of TiO <sub>2</sub> nanotubes (a) top view at 15 K magnification and (b)cross sectional view at 7K magnification of sample S1 (that was not washed in ethanol after anodization). .....	72
<b>Figure 3.4</b> TEM image of (sample S1) TiO <sub>2</sub> nanotubes at 100K magnification. ....	73
<b>Figure 3.5</b> TEM image of (sample S2) TiO <sub>2</sub> nanotubes at 100K magnification. ....	73
<b>Figure 3.6</b> Shows developing TiO <sub>2</sub> nanotubes from Ti metal substrate forming a nanotubular like array.....	76
<b>Figure 3.7</b> (Sample 1) of TiO <sub>2</sub> nanotubes, (a) View of face which was not in contact with Ti substrate (top view), (b) cross sectional view, left side edge in image was that not attached to Ti substrate (c)View of face that was attached to Ti substrate (bottom view).....	81
<b>Figure 3.8</b> (Sample 2) of TiO <sub>2</sub> nanotubes , (a) View of face which was not in contact with Ti substrate (top view), (b) cross sectional view, (c)View of face that was attached to Ti substrate (bottom view).....	82
<b>Figure 3.9</b> (Sample 3) of TiO <sub>2</sub> nanotubes, (a) View of face which was not in contact with Ti substrate (top view), (b) cross sectional view, (c)View of face that was attached to Ti substrate (bottom view).....	83
<b>Figure 3.10</b> Show SEM images of (a) top view at 13 K magnification and (b)cross sectional and top view at 3.5K magnification of TiO <sub>2</sub> nanotubes that were reduced in DMF-TBAP electrolyte solution followed by rinsing with DCM ( not washed in ethanol after anodization). ....	84
<b>Figure 3.11</b> Show SEM images of (a) top view at 15 K magnification and (b)cross sectinal view, right side edge in image was that not attached to Ti substrate, at 2K magnification of TiO <sub>2</sub> nanotubes that were reduced in ACN-TBAP electrolyte solution (not washed in ethanol after anodization). ....	85
<b>Figure 3.12</b> (Sample S3)TEM image of electrochemically reduced TiO <sub>2</sub> nanotubes in ACN at 100K magnification.....	86
<b>Figure 3.13</b> (Sample S3) TEM images of electrochemically reduced (in ACN) and annealed TiO <sub>2</sub> nanotubes at 100K magnification .....	86
<b>Figure 3.14</b> (Sample S3) HR-TEM images of electrochemically reduced in ACN and annealed TiO <sub>2</sub> nanotubes at 13.5K magnification. ....	87
<b>Figure 3.15</b> Illustrative (A) yellowish white and (B)dark blue colour of as-grown TiO <sub>2</sub> nanotubes before and after electrochemical reduction in 0.2M ACN-TBAP, respectively. ....	90

**Figure 3.16** X-ray diffraction peaks of the TiO<sub>2</sub> nanotubes arrays samples treated by various electrochemical and photochemical conditions. Sample j is a commercial Degussa P25 (80% anatase and 20% rutile) form. A and R represents anatase and rutile, respectively. ....92

**Figure 3.17** Cyclic Voltammograms of Ti/TiO<sub>2</sub> nanotubes electrode surface in 0.2 M TBAP-ACN and sweep rate was 100 mV/s under nitrogen atmosphere through potential window of [0 ~ (-)3 V], (a) Electrolyte cell/system at room temperature,(b)Electrolyte cell/system was placed in an ice bath. ....95

**Figure 3.18** Cyclic Voltammograms of Ti/TiO<sub>2</sub> nanotube electrode surface in 0.2 M TBAP-ACN and sweep rate was 100 mV/s under nitrogen atmosphere through potential window of [0.5 ~(-3) V], Electrolyte cell/system was placed in an ice bath, desiccated sample (a) and non-desiccated sample (b). ....96

**Figure 3.19** Cyclic voltammograms of Ti/TiO<sub>2</sub> nanotubes electrode surface in 0.2 M TBAP-ACN and sweep rate was 100 mV/s under nitrogen atmosphere, Electrolyte cell/system was placed in an ice bath, through various potential window (a)[0 ~ (-)2.5 V], (b)[0 ~ (-)3.0 V] and (c)[0.5 ~ (-)3.0 V]. ....97

**Figure 3.20** Cyclic Voltammograms of Ti/TiO<sub>2</sub> nanotube electrode surface in 0.2 M TBAP-ACN and sweep rate was 100 mV/s under nitrogen atmosphere through potential window of [0.5 ~(-3) V], Electrolyte cell/system was placed in an ice bath,(a) annealed sample at 280°C in nitrogen atmosphere and (b)amorphous sample .....98

**Figure 3.21** Cyclic Voltammograms of (a ,b) titanium dioxide nanotubes (Ti/TiO<sub>2</sub>) and (c) titanium (Ti) in 0.2 M TBAP-DMF or ACN and sweep rate 100 mV/s under nitrogen atmosphere through potential window of [ 0.5~ (-)3 V]. Electrolyte cell/system was placed in an ice bath. ....99

**Figure 3.22** Cyclic Voltammograms of Ti/TiO<sub>2</sub> nanotubes electrode surface in 0.2 M TBAP-ACN and sweep rate 100 mV/s under nitrogen atmosphere through potential window of [0.5 ~ (-)3 V], Electrolyte cell/system was placed in an ice bath..... 100

**Figure 3.23** Shows the band diagram for n-type single-crystal TiO<sub>2</sub> electrode based on CV measurements.(a) CV recorded for redox having redox potential above conduction band, reversibility of CV indicates metallic behavior of the electrode.(b) CV recorded for a redox having redox potential below conduction band, irreversibility of CV indicates rectifying nature of the junction.(c) Same CV for redox couples having redox potentials negative to ca. -0.3V indicating electron transfer through the surface states in this potential region ..... 102

<b>Figure 3.24</b> Shows (a) the band diagram for n-type single-crystal TiO <sub>2</sub> electrode based on CV for redox couples having redox potentials, and (b) its equivalent energy diagram vs density of states for semiconductor –electrolyte interface (SEI). .....	103
<b>Figure 3.25</b> Cyclic Voltammograms of 1M KCl and 10mM K <sub>3</sub> [Fe(CN) <sub>6</sub> ] using Ti/TiO <sub>2</sub> nanotubes as working electrode. Sweep rate was 100 mV/s of (a) amorphous TiO <sub>2</sub> nanotubes [0.9 ~ (-)0.2 V] and (b) annealed TiO <sub>2</sub> nanotubes at 280°C in nitrogen atmosphere [0.6 ~ (-) 0.2 V]. .....	106
<b>Figure 3.26</b> Cyclic Voltammograms of 1 M KCl and 10 mM K <sub>3</sub> [Fe(CN) <sub>6</sub> ] using Ti/TiO <sub>2</sub> nanotubes electrode as working electrode. Ti/TiO <sub>2</sub> nanotubes electrode were annealed in various gases. Sweep rate 100 mV/s through various potential window of (a) [0.6 ~ -0.2 V], nitrogen, (b) [1.1 ~ -0.5 V], argon and (c) [0.8 ~ -0.2 V], air.....	107
<b>Figure 3.27</b> Cyclic Voltammograms of 1 M KCl and 10 mM K <sub>3</sub> [Fe(CN) <sub>6</sub> ] using Ti/TiO <sub>2</sub> nanotubes as working electrode annealed at various temperatures. Sweep rate was 100 mV/s under nitrogen atmosphere through various potential window of (a) [0.6 ~ -0.2 V] at 280°C and (b) [1.2 ~ -0.2 V] at 380 °C .....	108
<b>Figure 3.28</b> As –anodized TiO <sub>2</sub> nanotubes of sample (R1) shows experimental and the simulated spectra in black and red, respectively. ....	109
<b>Figure 3.29</b> UV/Vis Diffuse Reflectance spectroscopy showing spectrum results of titanium dioxide nanotubes film on titanium substrate.....	112
<b>Figure 3.30</b> Tauc plots of reduced and annealed TiO <sub>2</sub> nanotubes (sample(h) in figure 3.27), showing possible fits to obtain the accurate band gap. ....	114
<b>Figure 3.31</b> XPS spectra of (reduced and annealed at 280°C in nitrogen) TiO <sub>2</sub> .....	116
nanotubes sample. ....	116
<b>Figure 3.32</b> XPS spectra of Ti 2p sample of (reduced and annealed at 280°C in nitrogen).....	117
TiO <sub>2</sub> nanotube. ....	117
<b>Figure 3.33</b> Degussa P25 (TiO <sub>2</sub> ) vs. TiO <sub>2</sub> nanotubes in 10 ppm of methylene blue (MB) solution under irradiation of UV. ....	123
<b>Figure 3.34</b> Degussa P25 (TiO <sub>2</sub> ) vs. TiO <sub>2</sub> nanotubes in 10 ppm of methylene blue solution exposed to sunlight for 3 hours.....	124
<b>Figure 3.35</b> Degussa P25 (TiO <sub>2</sub> ) Vs TiO <sub>2</sub> nanotubes in 50 ppm of methylene blue solution expose to sunlight for 3 hours.....	124

# LIST OF TABLES

<b>Table 1.1</b> Different TiO <sub>2</sub> polymorphs and some of their physical properties .....	5
<b>Table 2.1</b> Effect of NH <sub>4</sub> F concentration and H <sub>2</sub> O concentration in ethylene glycol electrolyte on the nanotube length, 60 V anodization potential and 17 hours duration .....	39
<b>Table 3.1</b> Different treatments of non reduced TiO <sub>2</sub> samples for SEM and TEM characterization. ....	69
<b>Table 3.2</b> Different treatments of reduced TiO <sub>2</sub> samples for SEM and TEM characterization. ....	80
<b>Table 3.3</b> Different treatments of TiO <sub>2</sub> nanotube and Degussa P25 (sample j) for XRD. ....	91
<b>Table 3.4</b> Different treatments of Ti/TiO <sub>2</sub> samples for RBS. ....	109
<b>Table 3.5</b> shows different treatments for Ti/TiO <sub>2</sub> samples for UV/Vis Diffuse Reflectance Spectroscopy. ....	111
<b>Table 3.6</b> Shows band gaps results of Ti/TiO <sub>2</sub> samples in figure 3.29. ....	115
<b>Table 3.7</b> shows different treatments for Ti/TiO <sub>2</sub> samples for elemental analyser (EA). ....	119
<b>Table 3.8</b> Shows elemental composition data of nitrogen and carbon of TiO <sub>2</sub> nanotubes samples (from elemental analyser) to calculate empirical formula .....	120

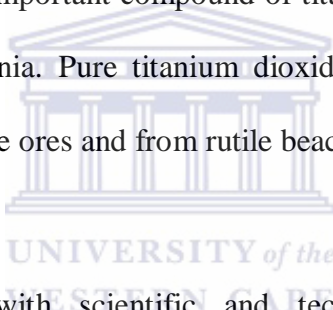
# CHAPTER 1

## INTRODUCTION

### 1Background.

#### 1.1 Occurrence and uses of titanium dioxide.

In terms of applications the most important compound of titanium is titanium dioxide, chemical formula  $\text{TiO}_2$ , also known as titania. Pure titanium dioxide does not occur in nature but is obtained from ilmenite or leucocene ores and from rutile beach sand.

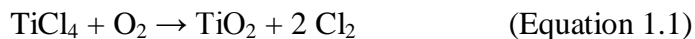


$\text{TiO}_2$  is a versatile material with scientific and technological applications such as photocatalysis[1-3], photosensitizers for photovoltaic cells [4-7], gas sensing [8-11], fabrication of solar cells [7,12], structural ceramics, optical coatings [7,13-14], as white pigment in paints and food, as a corrosion-protective coating [15-16], for removal of atmospheric pollutants and water pollutants, which is used in environmental remediation[17-18], biocompatible material for bone implants, spacer material for magnetic spin valve systems [7,13-14] and potentially in photochemical water splitting to produce hydrogen as a fuel [19-20].

Photocatalysts must be stable to the photolysis conditions, this is particularly evident when  $\text{TiO}_2$  is employed. A large number of oxidative conversions can be carried out on the catalyst without

severe degradation of the catalyst surface. One commercial form of TiO<sub>2</sub>, namely Degussa P25 is commonly used in photocatalytic experiments [21-23].

TiO<sub>2</sub> is normally produced industrially by the hydrolysis of TiCl<sub>4</sub> in a hot flame as depicted in the equation below.



The relatively short residence time (~10 ms) necessary for the conversion of TiCl<sub>4</sub> to TiO<sub>2</sub> gives a product with a high surface area (56 m<sup>2</sup>/g) and it consists of a mixture of 4:1 anatase to rutile crystalline forms [24].



## 1.2 Properties of TiO<sub>2</sub>.

### (a) Structural forms of TiO<sub>2</sub>.

Titanium dioxide has distinguishable crystalline polymorphs: anatase, rutile, and brookite. All have the same chemistry but differ in crystal structure which results in dissimilar electronic band properties.

Rutile is the most stable and common form of titanium dioxide, whereas anatase and brookite are metastable at all temperatures and convert to rutile when subjected to higher temperatures. Rutile and brookite shares several similar properties, however due to some structural differences they vary in crystal habit and cleavage, whereas crystals of anatase are very distinctive [25].

The TiO<sub>2</sub> oxides are made up of d<sup>0</sup> titanium ions at the centre of octahedral of six O<sup>2-</sup> ions. Each oxygen atom has three titanium neighbours and therefore belongs to three different octahedral. Both anatase and rutile can be described in terms of distorted TiO<sub>6</sub> octahedra, that is, Ti<sup>4+</sup> ions surrounded by six O<sup>2-</sup> ions. The rutile structure has a slight orthorhombic distortion, while the anatase octahedron is more distorted than rutile structure. Moreover, anatase has greater Ti-Ti distances than rutile (3.79 and 3.04 Å versus 3.57 and 2.96 Å) but shorter Ti-O distances (1.934 and 1.980 Å versus 1.949 and 1.980Å) [26].

In the rutile structure each octahedron is in contact with 10 neighbouring octahedrons (two sharing edge oxygen pairs and eight sharing corner oxygen atoms) while in the anatase structure each octahedron is in contact with eight neighbours (four sharing an edge and four sharing a corner). These differences in lattice structures cause different mass densities and electronic band structures between the two forms of TiO<sub>2</sub> [26].

Anatase is rare in abundance in comparison to rutile, and is also of great interest for its key role in the injection and transport of electrons in photovoltaic devices [27]. Brookite is the rarest form of the mineral, and is not easily obtained synthetically [28].

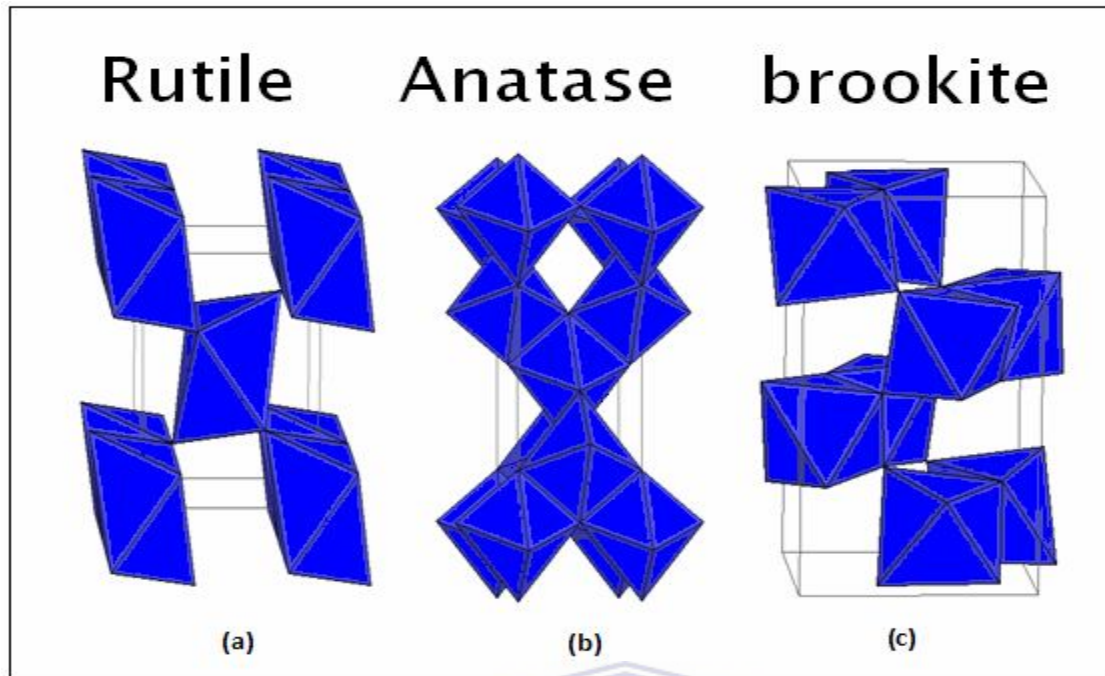
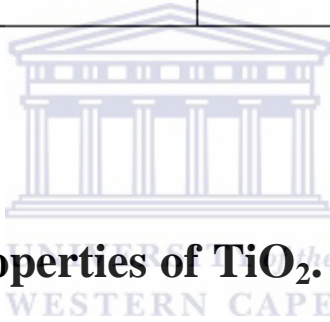


**Figure 1.1** TiO<sub>2</sub> different crystal structures: rutile (a), anatase (b) and brookite(c) [29].

Crystalline structures of TiO<sub>2</sub> have relatively wide band gaps (3.0 eV for rutile and 3.2 eV for anatase), as shown in table 1.1. However, the band gap of TiO<sub>2</sub> limits the absorption of sunlight to the ultraviolet region of the solar spectrum. Attaining useful energy conversion efficiencies requires a reduction in the electronic band gap of anatase TiO<sub>2</sub>.

*Table 1.1 Different TiO<sub>2</sub> polymorphs and some of their physical properties [28,30].*

<b>Crystalline phase</b>	<b>Crystal system</b>	<b>Density g/cm<sup>3</sup></b>	<b>Optical Band-Gap (eV)</b>	<b>Refractive index</b>
Anatase	tetragonal	3.79 – 3.84	3.19	2.52
Rutile	tetragonal	4.13 – 4.26	3.0	2.72
Brookite	orthorhombic	3.99 – 4.11	3.11	2.63



## **(b) Semiconductor properties of TiO<sub>2</sub>.**

### **(i) Some properties of semiconductors.**

Semiconductor materials, such as titanium dioxide, have energy levels in the form of valence and conduction bands, which are separated by an energy gap. Conduction requires that some electrons in the valence band are excited into the conduction band either by thermal or photo excitation. Upon excitation an unoccupied vacancy (hole) is left in the valence band. The holes and excited electrons can move in response to an applied electric field and so permit the passage of an electric current.

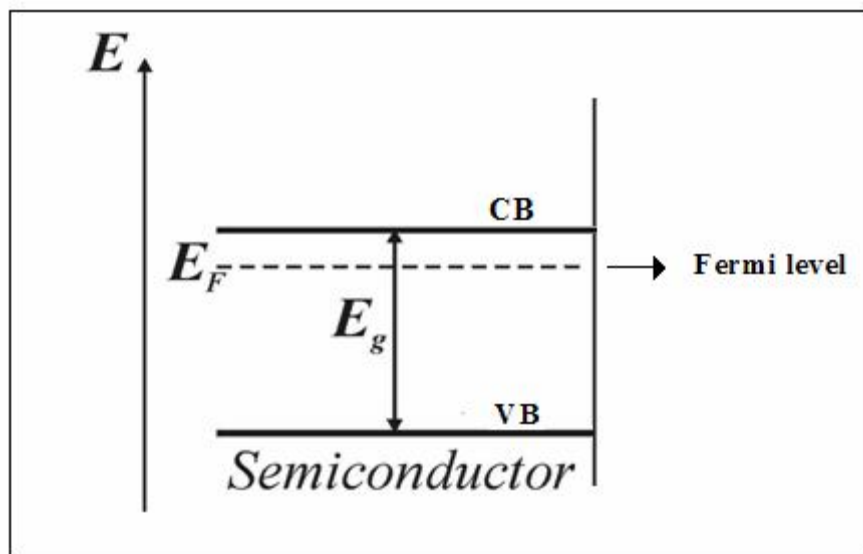


**Figure 1.2** Energy level diagrams illustrating valance band (vb), conduction band (cb), fermi energy( $E_F$ ) and energy gap( $E_g$ ) of a semiconductor.

Photocatalytic activity is strongly influenced by particle size (since smaller particles are more active than large ones), crystallinity and specific surface area. The Fermi Level is the highest occupied molecular orbital in the valence band at 0 K, so that there are many states available to accept electrons. The difference in photoactivity is also related to the Fermi levels, in which anatase is about 0.1 eV higher in energy than that of rutile. It has been reported that the anatase crystal structure has a very shallow donor level [31].

The band gap of a semiconductor is always one of two types, either a direct band gap or an indirect band gap. A direct band gap is a semiconductor in which the states of minimum energy in the conduction band and the state of maximum energy in the valence band have same momenta, so that optical transitions between free electrons and holes are allowed, while an

indirect band gap is a semiconductor in which the states of minimum energy in the conduction band and the state of maximum energy in the valence band have different momenta, and consequently optical transitions between free electrons and holes are forbidden. Indirect band gap semiconductors are used for dye-sensitized solar cell while those with direct band gaps are used for electronic device. Anatase has an indirect band gap [30,32-33].

The property of semiconductors that makes them most useful for constructing electronic devices is that their conductivity may easily be modified by introducing impurities into their crystal lattice. The process of adding controlled impurities to a semiconductor is known as doping. The amount of impurity, or dopant, added to an intrinsic (pure) semiconductor varies its level of conductivity. Doped semiconductors are often referred to as extrinsic. By adding impurity to pure semiconductors, the electrical conductivity may be varied not only by the number of impurity atoms but also, by the type of impurity atoms and the changes may be thousand folds and million folds.

In an intrinsic semiconductor, holes and electrons exist in pure material and semiconduction occurs without the introduction of any other material. Semiconduction can be controlled through the deliberate introduction of small quantities of material to an intrinsic semiconductor, so forming an extrinsic semiconductor.

When a semiconductor solid is brought into contact with a solution containing a redox couple then electron transfer may take place between the solution-phase species until the

electrochemical potential of the two phases becomes equal. When equilibrium is established the semiconductor will have gained a net positive or negative charge. This charge resides in a region near the surface of the solid and causes an electric field to be established within the semiconductor. This region is known as the space-charge layer and has a typical thickness of between 2 and 500 nm, depending on the conductivity of the solid.

In order to describe the distribution of charge within the semiconductor, the semiconductor bands are thought of as 'bent'. This implies an excess of negative charge at the surface if the bands are bent downwards, or an excess of positive hole at the surface if they bend upwards. Figure 1.3 shows the band bending effect induced by a redox couple (undergoing charge transfer) for an intrinsic semiconductor.

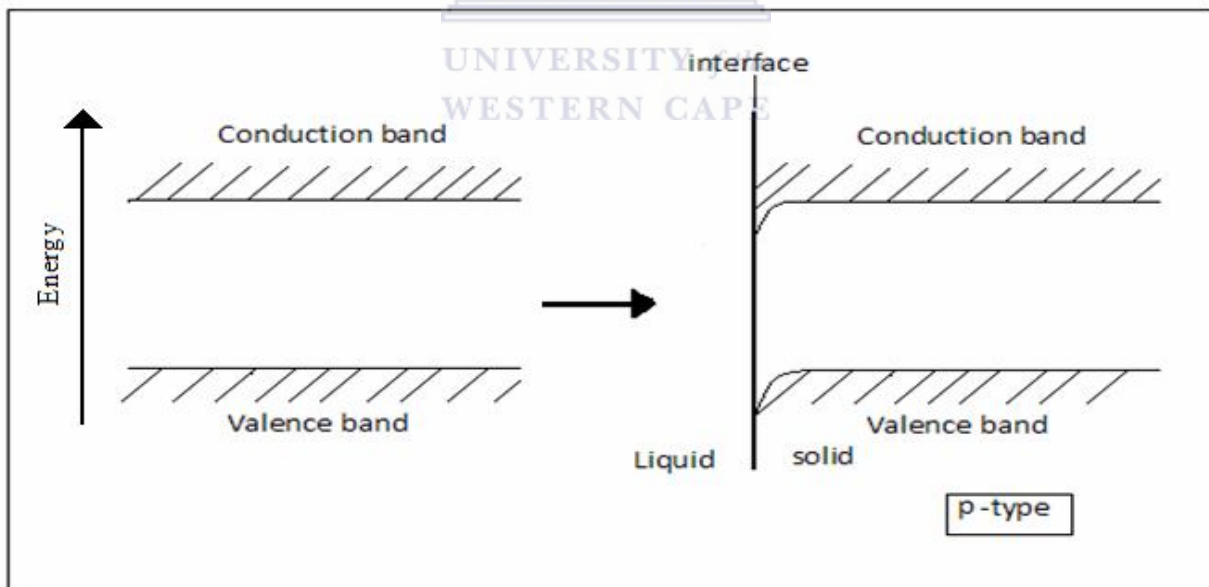
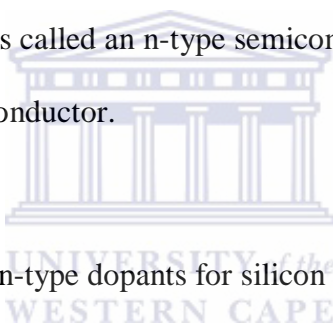


**Figure 1.3** Energy level diagrams illustrating the band bending effect in of p-type semiconductor.

If the semiconductor is controlled by a potentiostat then the applied potential from latter can change the energy of the conduction and valence bands in the bulk semiconductor. As a result the extend of the band bending within the solid can be changed and charge carries brought to, or removed from the space-charge layer so permitting electrolysis to occur at the solid/liquid interface.

An introduction of specific types of impurity atoms into a pure semiconductor can significantly increase its conductivity. These impurities, called dopants, add extra electrons or holes. A semiconductor with extra electron is called an n-type semiconductor, while a semiconductor with extra holes is called a p-type semiconductor.



For an example, the most common n-type dopants for silicon are phosphorus and arsenic. Notice that the two elements are in Group V of the periodic table, and silicon is in Group IV. When silicon is doped with arsenic or phosphorous atoms, these dopant atoms replace silicon atoms in the semiconductor crystal, but since they have one more outer-shell electron than silicon they tend to contribute this electron to the conduction band. By far the most common p-type dopants for silicon is the Group III element boron, which lacks an outer-shell electron compared with silicon and thus tends to contribute a hole to the valance band.

In n-type material, the application of a negative potential will encourage the build-up (accumulation) of charge carriers at the electrode surfaces and reduction of solution species may

occur. In contrast the application of positive potential will deplete charge carriers and oxidative processes are enhanced, relatively. For p-type material, negative potentials will deplete the space- charge layer of charge carries (holes) whereas positive potential will lead to their accumulation.

Electron excitation into the conduction band of a semiconductor can be achieved by photoexcitation with the results that a hole is left in the valence band. It follows that the electrochemical behavior of the semiconductor electrodes will be strongly modified if they are irradiated with light of an energy equal to, or greater than, that of the band gap. This is illustrated in Fig.1.4 for the case of TiO<sub>2</sub>.

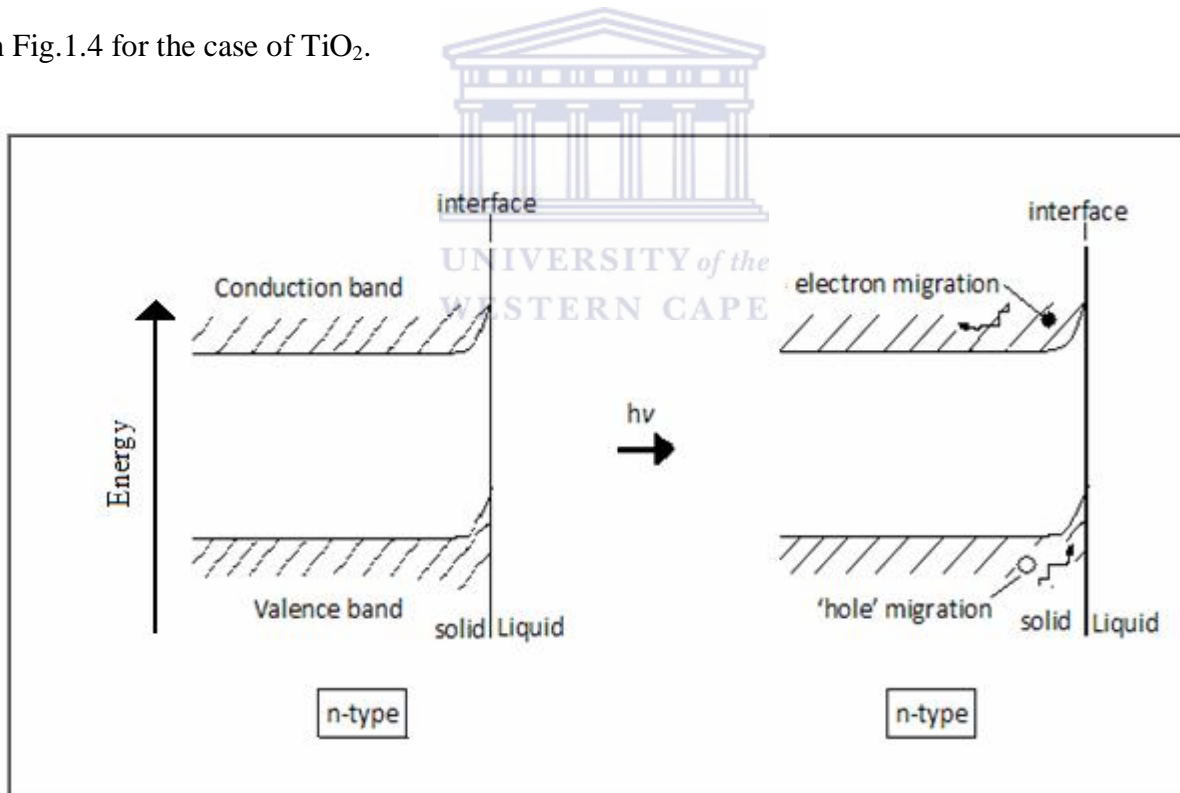
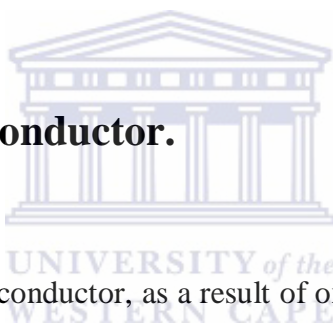


**Figure 1.4** Energy level diagrams illustrating the band bending effect in of n-type semiconductor.

For an extrinsic n-type semiconductor, such as  $\text{TiO}_2$ , the conduction and valence bands bend upwards at the surface unless a very negative potential is applied to the electrode, consequently, those electrons photochemically promoted to the conduction band will be swept into the bulk of the material by the electric field present in the space-charge layer. Equally, the holes left in the valence band will move under the influence of the same field but will migrate to the surface of the solid. As a result, under this condition of irradiation, photooxidations are encouraged to occur at the interface of the n-type semiconductor and solution [34-36]

## **(ii) $\text{TiO}_2$ an n-type Semiconductor.**



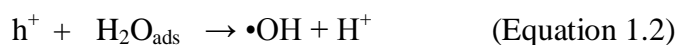
Titanium dioxide is an n-type semiconductor, as a result of oxygen deficient sites, which exist in the lattice. Due to these defect sites the bands are bent upwards at the surface relative to the bulk, which results in a spatial separation of the charge carriers. The holes in the valence band are drawn to the surface where they exhibit a strong oxidizing potential [37].

The Fermi level is a probability distribution curve that represents a 50% possibility of locating an electron at a given energy level [38]. For an n-type semiconductor such as  $\text{TiO}_2$  the Fermi level is close to the conduction band. Semiconductors material are called n-type because the majority of charge carriers which will contribute to an electrical current through the material are negatively charged free electrons produced by the doping process. There will be some contribution to the

current flow from positively charge holes due to electron hole pair generation but these holes are the minority charge carriers in this material [38-41].

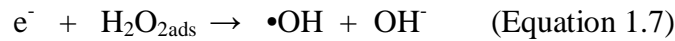
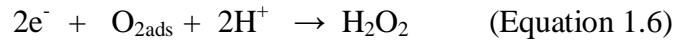
A hole can initiate reactions with adsorbates and can itself diffuse into the solvent bulk. Hole trapping is usually achieved by the use of degradable adsorbates or with the aid of sacrificial donors, these sacrificial donors are so called hole scavengers [21, 23, 42-46]. For TiO<sub>2</sub>, the reactive species is the hole and carries the major part of the light quantum energy. The energy is the driving force for the oxidation of organic and inorganic molecules that react at the TiO<sub>2</sub> surface [45].

When a hole migrates to the surface almost all of them react with the surface bound hydroxyl groups to form OH<sup>•</sup> radicals. Species such as water (equation 1.2), hydroxyl ions (equation 1.3), or organic compounds (equation 1.4).

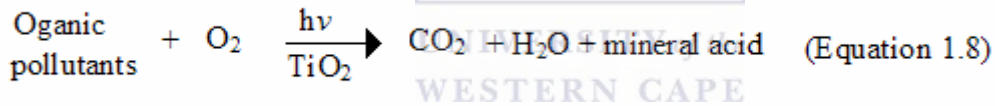


The electrons can also react with the compounds that are present in the solution such as oxygen and hydrogen peroxide. The electrons can be absorbed by the oxygen to form superoxide (equation 1.5) or it can react with oxygen together with hydrogen to create hydrogen peroxide

(equation 1.6). It can then react with hydrogen peroxide to create hydroxyl radicals and hydroxyl ions (equation 1.7).



All of these produced species are highly reactive, capable of attacking and breaking down organic compounds they come in contact with [43]. In aqueous suspensions the holes in the valences band have sufficient oxidizing power to convert most organic pollutants to CO<sub>2</sub>, H<sub>2</sub>O and mineral acids like HCl, as shown in the reaction below [21,47].



Titanium dioxide (TiO<sub>2</sub>) is an n-type semiconductor that absorbs primarily in the ultraviolet portion of the solar spectrum. TiO<sub>2</sub> can only make use of 3-4% of the solar energy reaching the surface of the earth since most of the solar radiation is of a wavelength that is greater 400 nm. When UV light strikes the surface of TiO<sub>2</sub> (which is slightly deficient in oxygen), electrons from filled valence band are promoted to the vacant conduction band and produce active oxygen species (hydroxyl radical and superoxide anion) which decomposes toxic organic substances by oxidation.

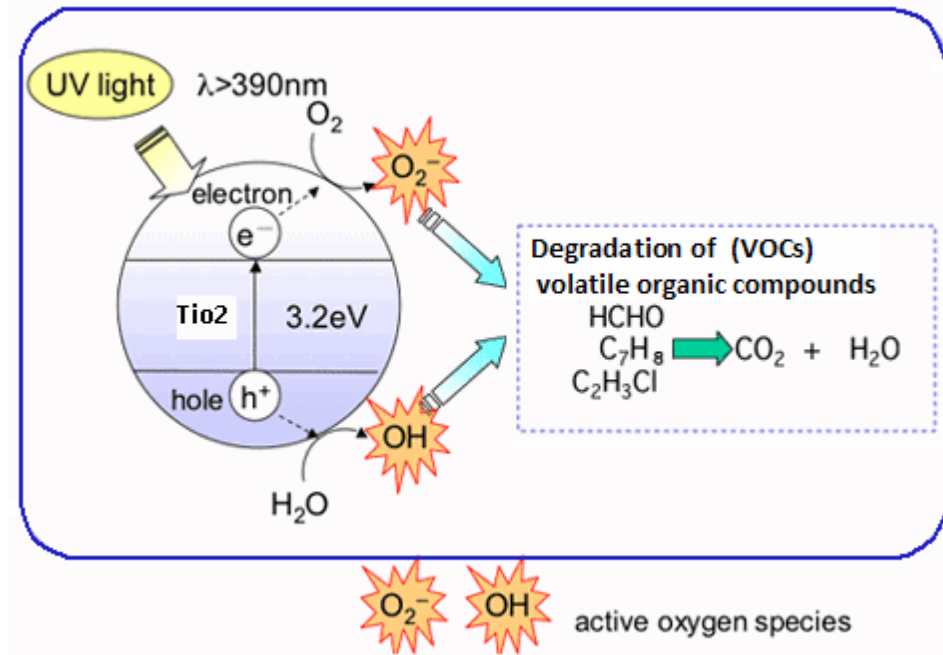


**Figure 1.5** Mechanism of photocatalysis using energy from the light [48].

This only occurs when the electrons absorb photons of sufficient energy to overcome the band gap energy of TiO<sub>2</sub> which is 3.0-3.2eV. The valence band consists mainly of oxygen 2p states, and conduction band prevalently from titanium 3d states.

Activation of the photocatalyst by photon absorption produces a charge separation that results in the formation of electrons in the conduction band and leaves holes (positive charges) in the valence band.



The mean-life of these electron-hole pairs before recombination is in the order of nanoseconds, a time in which they may be able to move to the catalyst surface and undergo reactions with some

of the adsorbed species. Hence, electrons and holes that do not recombine may participate in reduction and oxidation reactions, respectively [49].

TiO<sub>2</sub> can convert photon energy into chemical/electrical energy by generating electrons and holes pairs upon UV irradiation. The resulting charge carriers can migrate to the surface where they can react with adsorbed water and oxygen to produce radical species which are strong oxidizing agents.

In order to improve the efficiency of TiO<sub>2</sub> as a photocatalyst it must be able to absorb more of the solar spectrum so that it becomes active under visible light (sunlight) excitation utilizing even interior room lighting to degrade a large number of organic and inorganic contaminants. This can be achieved by reduction of the titanium dioxide band gap, which will allow the semiconductor material to absorb photons of wavelength than 400 nm in the visible light region.

### **(c) Photocatalytic properties of TiO<sub>2</sub>.**

Sectors such as the pharmaceutical, textile, agricultural, food, and chemical industries, all produce waste effluent contaminated with organic compounds such as aromatics, haloaromatics, aliphatics, dyes, dioxins and a wide range of other polluting materials. Many of these materials are extremely toxic and the waste streams must be treated prior to discharge. Incineration of organic waste is not always effective and can disperse large quantities of toxic emissions, such as products of incomplete combustion or heavy metals, into the atmosphere. An effective treatment

system is required which can degrade the polluting materials prior to discharge of the effluent. The photocatalytic process is a technique which could address both these requirements.

In recent years, applications related to environmental cleanup have been one of the most active areas in heterogeneous photocatalysis. This has been inspired by the potential application of TiO<sub>2</sub>-based photocatalysts for the total destruction of organic compounds in polluted air and wastewaters [18,50]. This process involves the utilisation of a non-toxic semiconductor catalyst such as titanium dioxide.

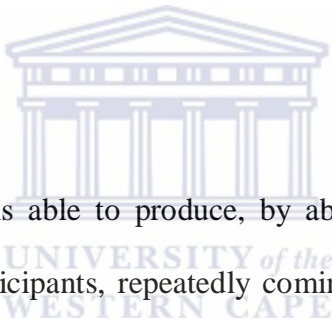
In 1972, Fujishima and Honda discovered the photocatalytic splitting of water on TiO<sub>2</sub> electrodes [51]. This event marked the beginning of a new era in heterogeneous photocatalysis. Since then, research efforts in the understanding the fundamental processes and in enhancing the photocatalytic efficiency of TiO<sub>2</sub> have come from extensive research performed by chemists, physicists, material scientists and chemical engineers. Such studies are often related to energy renewal and storage [52-56].

Among the metal oxides semiconductors suitable for photocatalytic process, titanium dioxide is the most widely used due to its relatively favorable band-gap energy and its photocorrosion stability in the reaction conditions [57-58]. Moreover, TiO<sub>2</sub> has proved to be the best photocatalyst due to its strong oxidizing power under UV illumination and its chemical stability. The photocatalytic properties of TiO<sub>2</sub> are affected by several factors, such as crystal structure,

morphology, surface area and porosity [59]. It is well known that  $\text{TiO}_2$  has three kinds of crystal phases and an anatase  $\text{TiO}_2$  has the highest photoactivity among the three phases.

Semiconducting oxides such as  $\text{TiO}_2$  are uncomplicated to obtain synthetically. Titanium dioxide remains the most promising photocatalyst due to a broad range of applications, low cost, availability, non-toxicity, non-selectivity, high stability, chemical inertness, and resistivity to corrosion, the strong oxidizing power of the photogenerated holes/electrons, photocorrosion, and photostability [26,50,60-62].

### **(i) Photocatalysis.**



Photocatalyst is a substance that is able to produce, by absorption of light quanta, chemical transformation of the reaction participants, repeatedly coming with them into the intermediate chemical interactions and generating its chemical composition after each cycle of such interaction. Photocatalysis is a change in the rate of chemical reactions under the action of light in the presence of substances-called photocatalyst.

The photocatalyst itself will not decompose and it can be re-used indefinitely. Photocatalysis processes involve the initial absorption of photons by a molecule or the substrate to produce highly reactive electronically excited states. A reactive center can be a molecule or a surface reactive site. The electron transfer process requires the overlap between the occupied donor

orbital and the acceptor orbital which may be empty or half-filled. An energy transfer process takes place by electron exchange or dipole-dipole resonant coupling [63].

The initial process for heterogeneous photocatalysis of organic and inorganic compounds by semiconductors is the generation of electron-hole pairs in the semiconductor material. In photocatalysis, irradiated semiconductor particles must be in close contact with a liquid or gaseous reaction medium. At the level of the material's surface, the requirements for efficient photocatalysis can be deduced from the electronic reactions.

There should be surface bound water to allow for efficient oxidation; and the water should be aerated to provide oxygen to the solution. Additionally, the degradation of the pollutant by the catalyst requires for the pollutant to be adsorbed or very close to the surface of the material, and hence the greater the surface area of the material, the more pollutant can adsorb. Semiconductor particles may be photoexcited to form electron donor sites (reducing sites) and electron acceptor sites (oxidizing sites), providing great scope as redox reagent [64-65].

The molecular orbitals of semiconductors have a band structure. The bands of interest in photocatalysis are the occupied valence band and the unoccupied conduction band. They are separated by an energy distance referred to as the band gap. When the semiconductor is illuminated with light of greater energy than that of the band gap, an electron is promoted from the valence band to the conduction band. This leaves a positive hole in the valence band.

The hole has the potential to oxidize water that may be on the surface of the material resulting in the formation of hydroxyl radicals. Hydroxyl radicals are themselves very powerful oxidizing agent, and can easily oxidize any organic species that happens to be nearby, ultimately to carbon dioxide and water. In the conduction band, the electron has no hole to recombine with, since it has oxidized surface bound water. It quickly looks for an alternative to reduce, and rapidly reduces oxygen to form the superoxide anion. This can subsequently react with water to form, again, the hydroxyl radical.

The electron and hole pair may recombine with the generation of heat. If they are separated they can become involved in electron transfer reactions with other species in the solution [26, 66].

## **(ii) $\text{TiO}_2$ as a photocatalyst.**



Titanium Dioxide acts as a photocatalyst which has a strong oxidizing effect when activated by ultraviolet light such as sunlight.  $\text{TiO}_2$  has stronger oxidation ability than ozone and anion, stronger absorbability than active carbon, and has the efficacy (decomposing bacteria), which the active carbon does not have. It has strong redox ability that makes it decompose various organic and inorganic matters. Furthermore, it has strong efficacy of decomposing formaldehyde, benzene, ammonia and other organics that are discharged by fitment materials .Also it can eliminate the contaminants such as CO,  $\text{SO}_2$ , NO and oxyhydrogen compound.  $\text{TiO}_2$  does not produce other contaminants and radiation matters.

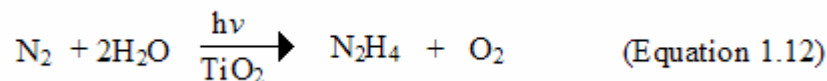
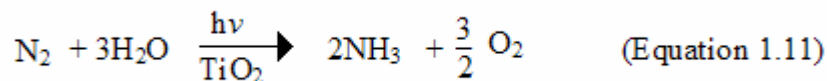
Efforts have been made to make use of  $\text{TiO}_2$  for both water and air purification. Although there have been several reports on photocatalytic water treatment [18,21,67-68], there are still practical and economical problems that must be addressed before commercialization can proceed. However, air purification through  $\text{TiO}_2$  photocatalysis has proven to be highly successful [69-71], and commercial products in various forms are available on the market today. Researchers have demonstrated that the low-intensity UV radiation from various types of indoor lighting fixtures such as fluorescent lamps is sufficient to photocatalytically decompose nearly all contaminants in indoor environments [69-71].

Furthermore, researchers have succeeded in developing transparent  $\text{TiO}_2$  coatings on various substrates such as glass and ceramic tiles that are capable of photodegrading various noxious or malodorous chemicals, smoke residues and cooking oil residues. Self-cleaning surfaces in various forms, including  $\text{TiO}_2$ -coated tiles, window glass, wallpaper, lampshades and lamp cover glasses are developed by various companies to help maintain clean indoor environments.  $\text{TiO}_2$ -containing cloth as a tent material and  $\text{TiO}_2$  coatings on various surfaces such as automobile bodies and aluminium siding for buildings have also been shown to be very effective in keeping these surfaces clean in the open air.

In addition to photocatalytic properties,  $\text{TiO}_2$  films have exhibited extreme photoinduced hydrophilicity as well as amphiphilic surface wettability, leading to applications in anti-beading and anti-fogging glass. Based on these properties, anti-beading automobile side-view mirrors are being produced even today.

The photoreduction of N<sub>2</sub> to ammonia on semiconductor powder represents an attractive way to convert solar energy into a useful chemical product. For example, N<sub>2</sub> photo fixation has been suggested as a possible method of producing fertilizer in place with appropriate semiconductor powder [49]. The metal oxides are preferably used in a form which has a high surface area for contact with nitrogen and water. However, TiO<sub>2</sub> doped has higher activity than undoped TiO<sub>2</sub> [72].

TiO<sub>2</sub> is irradiated in the presence of nitrogen and water with ultraviolet light. The nitrogen and water may be in the vapor phase, or they may be adsorbed on the metal oxide. In addition, liquid water may be present. The ammonia which is formed may be recovered in a number of ways, for example, by heating the metal oxide gently under vacuum, by water extraction, or by adsorption in an acid acceptor. The recovered ammonia may be used as an agricultural fertilizer either directly or in the form of ammonium nitrate, sulfate, or phosphate salts [72]. Schrauzer and Guth [73] demonstrated that iron-doped TiO<sub>2</sub> promotes the photoreduction of chemisorbed N<sub>2</sub> to NH<sub>3</sub> and N<sub>2</sub>H<sub>4</sub> according to the following equations.



The reduction of  $N_2$  to  $NH_3$  and  $N_2H_4$  appears to proceed in a stepwise fashion on 2-electron reducing sites at the  $TiO_2$  surface, via chemisorbed  $N_2H_2$  as the intermediate. This presents an improved method for fixing nitrogen, for example, nitrogen from air, by reduction to ammonia and also provides a method for preparing photocatalysts useful for reduction of nitrogen.

### **1.3 Reducing the band gap of $TiO_2$ .**

Efficient use of solar radiation requires extending the photo-response of  $TiO_2$  to visible wavelengths. This can be achieved by reduction of the titanium dioxide band gap, which will allow the semiconductor material to absorb photons of wavelength greater than 400 nm in the visible light region. Reducing the band gap of  $TiO_2$  is important for utilization of sunlight or even interior room light. Also, it will minimize energy that is required to photo-excite an electron from the valence band to the conduction band, as a result it will enhance the efficiency of  $TiO_2$  for various applications.

Several methods have been attempted to reduce the band gap of  $TiO_2$  [74]. External sensitizers such as organic dyes and polymers have been successfully employed to increase photoconversion efficiencies in photovoltaic cells [75-77]. However, the sensitizers may detach from the  $TiO_2$  surface in aqueous media and these organic sensitizers degrade in corrosive and highly oxidizing environments.

For applications such as photoelectrochemical water-splitting, and photocatalytic degradation of organic compounds, where the photoelectrode is subject to prolonged exposure to an aqueous medium, the external sensitizer approach is not feasible. The other approach involves manipulating the chemical composition of titania towards modifying its electronic structure. Cationic doping of TiO<sub>2</sub> with transition metals such as V and Cr has been extensively studied [78-80]. Other transition metal dopants such as Cr<sup>3+</sup> create sites which increase electron-hole recombination [81]. It is believed that these transition metals create acceptor and donor centers where direct recombination occurs.

While there is an improvement in the optical absorption for visible wavelengths, there is also an increase in thermal instability [82] and a decrease in carrier lifetimes [80], which limits overall conversion efficiencies. Calcination in different gaseous atmosphere has been used to introduce non metal doping to narrow the band gap and enhance electrical conductivity [83-88].

Transition metal ions and non-metals have been introduced into TiO<sub>2</sub> layers, and effects on the band gap of various magnitude have been reported for the different approaches [89- 91]. Asahi and co-workers [92] performed densities of states (DOSs) calculations on the effect of substitutional non metal doping of C, N, F, P or S for O in the anatase crystal. They identified nitrogen as the most effective dopant due to its comparable ionic radius and because its p states contributed to band gap narrowing by mixing with the p states of oxygen [93].

There has recently been a surge of interest in this area documenting different experimental approaches towards nitrogen doping of titania [94-96]. When vacuum techniques such as ion beam assisted deposition [95], pulsed laser deposition [96] and reactive sputtering[97] in a

nitrogen atmosphere are used to dope  $\text{TiO}_2$ , nitrogen atoms occur as  $\beta\text{-N}$  and are bonded to Ti atoms in substitutional lattice sites to form  $\text{TiO}_{2-x}\text{N}_x$ . On the other hand, when wet chemical methods are used, a substantial portion of the doped nitrogen is not directly bound to Ti [98]. Other method to incorporate anionic dopants, specifically nitrogen, is electrochemical anodization process that allows simultaneous nanostructuring and doping of the anodic film [99].

## 1.4 Reduction of $\text{TiO}_2$ .

$\text{TiO}_2$  samples in the form of single crystals, powders, or thin films become electrically conducting when they are reduced. Chemical reduction is associated with a change in the oxidation state of the transition-metal ion, formally  $\text{Ti}^{4+}$  in stoichiometric  $\text{TiO}_2$ , with the formation of  $\text{Ti}^{3+}$  species.  $\text{Ti}^{4+}$  cannot react with other non metals since is more stable than  $\text{Ti}^{3+}$ . Reduced titanium dioxide is believed to be more reactive to water, oxygen and non metals. These species ( $\text{Ti}^{3+}$ ) are believed to be responsible for the electronic conductivity [100-101].

The formation of  $\text{Ti}^{3+}$  species upon  $\text{TiO}_2$  reduction is supported by several pieces of experimental evidence as follows.

- (i) The sample blue color, whose intensity increases with the level of reduction, is assigned to d-d transitions [102].

(ii) The occurrence of a gap state at  $\sim 2$  eV above the valence band maximum and

$\sim 1$  eV below the conduction band minimum, which is observed by

photoelectron spectroscopy [103-105] and electron energy loss experiments [106].

(iii) The Electron Spin Resonance (ESR)-measured g-tensor typical of a Ti  $3d^1$  state [107-109].

(iv) The shift in the core level binding energies of the reduced Ti atoms [110].

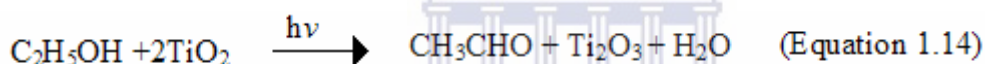
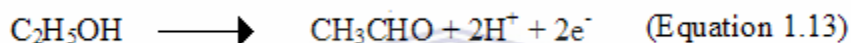
(v) The population of Ti-3d states as probed by resonant Auger electron spectroscopy [111] or resonant photoemission [112].

(vi) Resonant photoelectron diffraction patterns recorded for photoelectrons from Ti-3d defect states [113].

## **(a) Photochemical reduction.**

It has been well reported that alcohols are readily oxidized in the presence of light on a TiO<sub>2</sub> catalyst [114-119]. The photooxidation occurs by the irradiation process involving hydroxyl radicals produced from the oxidation of surface OH<sup>-</sup> groups by photoproducted holes. The oxidation can also start from the direct reaction with the photo produced holes in the valence band.

With alcohol oxidization, the TiO<sub>2</sub> catalyst is very efficiently reduced as demonstrated in the reaction below.



TiO<sub>2</sub> turns from white to blue, this blue colour is characteristic of Ti<sup>+3</sup> ions. The yield of acetaldehyde photo-produced initially increases until it reaches a maximum after which the yields remain constant. This is explained by the fact that the TiO<sub>2</sub> is reduced to Ti<sub>2</sub>O<sub>3</sub>, and Ti<sub>2</sub>O<sub>3</sub> does not react with ethanol. This seems to suggest that the surface Ti<sup>3+</sup> site reaches a saturation level after a few hours.

## (b) Electrochemical reduction.

TiO<sub>2</sub> can be reduced electrochemically in organic compounds with development of a blue colour. The colour is caused by electrons residing on surface titanium ions and it has been shown by an ESR study that the electrons in the reduced TiO<sub>2</sub> are predominantly located on the titanium ion

(i.e.  $Ti^{3+}$ ) on surface sites. The blue colour is not developed under all organic compounds such as hexane, since many compounds are very easily reduced by the electrons of the blue  $TiO_2$  [112]. These electrons are mobile in  $TiO_2$  surface under the influence of an electric field.

There are several methods to reduce  $TiO_2$  electrochemically. The blue colour can be obtained by chemical reduction with the Grignard reagent, such as phenylmagnesium bromide (in ethyl ether, under nitrogen). By wafer of compressed  $TiO_2$  under DMF which was contacted with a platinum wire as cathode and second platinum electrode serves as anode while applying potential difference.  $TiO_2$  can even be reduced with base metals, such as zinc in DMF by refluxing [113].

If oxygen or other easily reduced species are absent, the  $TiO_2$  assumes a blue colour which fades on exposure to oxygen or other oxidants such as iodine since  $Ti^{3+}$  is very reactive with oxygen and  $H_2O$  [120-122]. The reduced titanium dioxide is very important since it can react with non metals such as nitrogen and etc. Incorporation of nitrogen into the reduced titanium dioxide narrows the band gap of a semiconductor [95].

### **(c) Cyclic voltammetry studies in non-aqueous solution.**

Cyclic voltammetry is the most versatile electroanalytical technique for the study of electroactive species or redox systems. The cyclic voltammetric response of semiconductor electrodes has been used for accurate determinations of the semiconductor flat-band potential and for identification of surface state densities and energies [123-124].

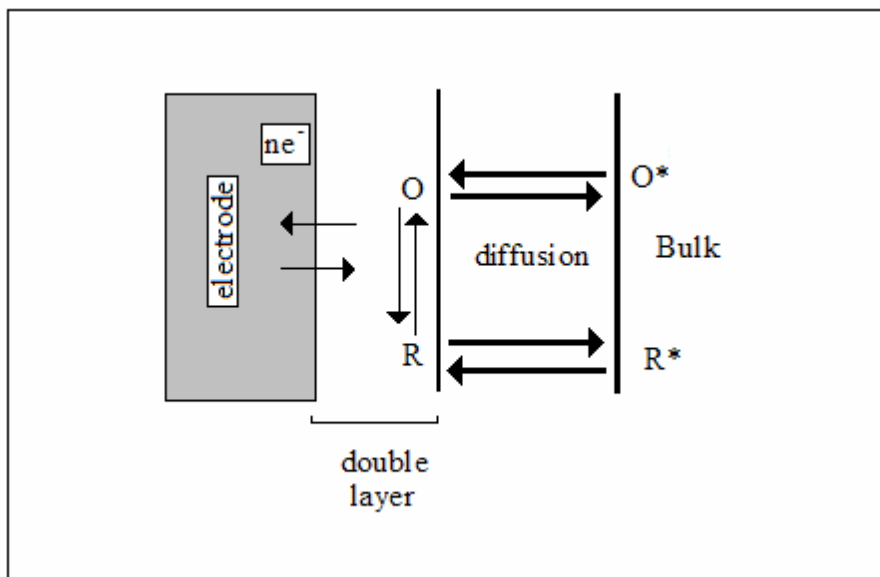


**Figure 1.6** Electrochemical system that includes electron transfer [125].

Figure 1.6 describes the process that occurs in simple electrode reactions. In the case of reduction, a species (O) capable of receiving an electron from the electrode diffuses to the surface, receives an electron and diffuses away from the surface. Current at the surface is generated by the transfer of electrons from the electrode to the redox species.

The charge transfer between a semiconductor and a species in solution is postulated to be equienergetic. This requires that there exists a significant overlap between the semiconductor bands at the surface and the donor and acceptor levels in solution. For a small band-gap semiconductor the possibility exists that a redox couple overlaps both the conduction and valence bands, so that there may be contributions to the exchange current from both bands [126].

The energy level of the particles differ, however, from the bulk, for extremely small particles, the Fermi level shifts to more negative values due to the quantum size effect. With slightly larger

particles, photogenerated electrons can have energy that is different from that of conduction band edge of the bulk semiconductor in contact with the same solution. Thus, measurements of the energy of dispersed particle are very important in deciding whether a given particle is in position to reduce or oxidize [125].

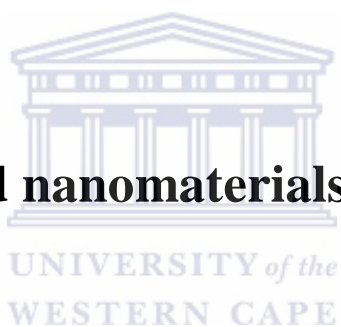
Studies on the number of semiconductor electrodes immersed in both aqueous and non aqueous solution have shown that account must also be taken of surfaces states and intermediate levels, as well as changes in the nature of surface during electrochemical studies that are specific to the semiconductor material and solvents [127].

The latter effects are particularly important with small band gap semiconductors which tends rather easily reduced or oxidized. Such surface effects are also of importance in photoelectrochemical cells for the conversion of light energy to chemical and/or electrical energy and results in quantum efficiency which vary with time, photocorrosion, passivation of the electrode surface, and development of surface layer which can affect the observed photopotential.

Acetonitrile has been shown to be well suited to the study of semiconductor electrochemistry [128-130] because of its large stability gap (5 V vs. 1.5 V for water) and hence its suitability for a large number of reversible one-electron redox systems spanning a wide potential range. Thus many stable redox couples exist in acetonitrile, which show reversible electrochemical behavior over a wide range of redox potential.

When semiconductor electrode is brought to negative potentials, reduction of surface electrode occurs [127]. It is also known that the reduction of nanocrystalline TiO<sub>2</sub> thin films is more facile in the presence of “potential determining” cations, such as Li<sup>+</sup>, Na<sup>+</sup> and Mg<sup>2+</sup> [131]. However, tetrabutylammonium perchlorate is used to prevent intercalation. In neat acetonitrile (or 0.1 M tetrabutylammonium perchlorate) electron injection is suppressed and long-lived metal ligand charge transfer (MLCT) excited states are observed. A model has been proposed wherein cation adsorption to the nanocrystalline semiconductor lowers the energy of TiO<sub>2</sub> acceptor states and increases the efficiency of interfacial charge injection from vibrationally hot molecular excited states [132-133].

## 1.5 Nanoscience and nanomaterials.



Nanoscience is the study which deals with structures of the size 100 nanometers or smaller in at least one dimension to manipulate and control the matter on atomic and molecular scales, where properties differ significantly from those at a larger scale. Nanoscale materials exhibit remarkable properties, functionality, and phenomena due the influence of small dimensions. The bulk properties of materials often change dramatically when nanosized particles are involved.

Nanotechnology is based on the manipulation, control, and integration of atoms and molecules to form materials, structures, components, devices, and systems at the nanoscale. Nanotechnology is the application of science in new nanomaterials and nano -concepts for new components, systems and products. Therefore, nanotechnology will provide us with the ability to design

custom-made materials with any property we require, especially to industrial and commercial objectives. Nanotechnology deals with materials and systems having the following key properties [134-135].

- They have at least one dimension of about 1 – 100 nm.
- They are designed through processes that exhibit fundamental control over the physical and chemical attributes of molecular scale structures.
- They can be combined to form large structures.

Nanotechnology has the potential to impact all products manufactured now and in the future. Nanotechnology is the natural progression of technology miniaturization from the bulk macroscopic world (e.g., the plow) to millimeter-sized objects (e.g., the first transistor) to micron dimensions (e.g., integrated circuits) and finally, into the nanoworld (e.g., the quantum dot). Nanotechnology has the potential to create many new materials and devices with a vast range of applications, such as in medicine, electronics and energy production.

There are two principal factors which cause the properties of nanomaterials to differ significantly from other materials, they are:

- (i) Increased relative surface area.
- (ii) Quantum effects.

These factors can change or enhance properties such as reactivity, strength and electrical characteristics. As a particle decreases in size, a greater proportion of atoms are found at the surface compared to those inside. For example, a particle of size 30 nm has 5% of its atoms on its surface, at 10 nm 20% of its atoms, and at 3 nm 50% of its atoms.

Thus nanoparticles have a much greater surface area per unit mass compared with larger particles. As growth and catalytic chemical reactions occur at surfaces, this means that a given mass of material in nanoparticulate form will be much more reactive than the same mass of material made up of larger particles.

Nanomaterials can be made (using various methods) of carbon, ceramics, chemical precursors, ferrites, metals, minerals, polymers, semi-conductors and silica or silicates. Nanotechnology products are devices that utilize nanostructures. There are many types of nanomaterials and nanotechnology products.

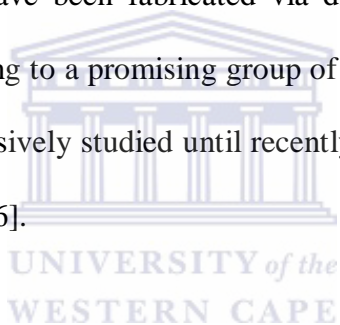
## **1.6 Nanostructured titanium dioxide**

The ability to control the architecture of titanium dioxide down to nanoscale dimensions can be expected to positively impact a variety of economically important technologies [136]. The properties of semiconductor particles are known to depend very sensitively on particle size [137]. In addition, electrical properties may show unusual characteristics and crucial behavior

when passing from the large-scale to the nanoscale, due to quantum effects provoked by the nanostructure of the particles.

Recently, there have been extensive studies on nanoparticle materials because of admirable physical properties and wide-range of applications [138-139]. Formations of metal-oxide layers on titanium metal have attracted more attention due to emerging technological developments. TiO<sub>2</sub> layers can possess various morphologies in thin film such as nanowires, nanofibers, nanorods, nanoporous and nanotubes structure [140-145].

These morphological structures have been fabricated via diverse techniques and reported by many researchers. Nanotubes belong to a promising group of nanostructured materials. Titanium dioxide nanotubes have been intensively studied until recently but their modification has not yet been explored to a great extent [146].



## 1.7 Titanium Dioxide Nanotubes.

There is a great interest in TiO<sub>2</sub> nanotubes because of their unique physical properties. TiO<sub>2</sub> nanotubes have high surface-to-volume ratio and size dependent properties. The increased exploitation of the specific functional properties of TiO<sub>2</sub> nanotubes in various applications is due to their large surface area, high surface activity and high sensitivity. TiO<sub>2</sub> nanotubes are suggested to be superior in chemical and photoelectrochemical performances [75,147-149], due to the one-dimensional channel for carrier transportation, in which the amount of recombination of e<sup>-</sup>/h<sup>+</sup> is expected to reduce.

G.K. Mor et al. [150] have noted the hydrogen sensitivity of the material, about seven orders of magnitude (1,000,000,000%) change in the electrical resistance at 23 °C in response to 1000 ppm hydrogen, appears to be the largest known sensitivity of any material at any temperature to any gas [9]. TiO<sub>2</sub> nanotubes with completely different lengths, diameters and thickness can be simply grown by controlling the electrochemical conditions and other parameters during the anodization process. The two basic criteria for growth of the nanotubes are sustained oxidation of metal and pore growth by chemical/field-assisted dissolution of the formed oxide with nanotube length determined by the dynamic equilibrium between growth and dissolution processes [151-152].

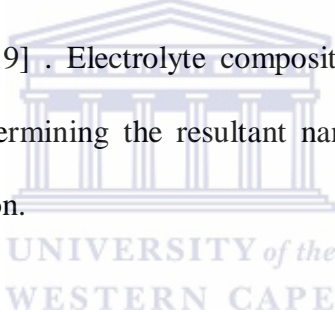
## **1.8 Fabrication of TiO<sub>2</sub> nanotubes.**

### **(a) Anodization of titanium.**

Anodic oxidation encompasses electrode reactions in combination with electric field driven metal and oxygen ion diffusion leading to the formation of an oxide film on the anode surface. Anodic oxidation is a well-established method of producing different types of protective oxide films on metals [147,153]. Anodic titanium oxides have high resistivity relative to the electrolyte and the metallic parts of the electrical circuit. The applied voltage drop mainly occurs across the oxide film of the anode. As long as the electric field is high enough to drive the ions through the oxide, a current will flow and the oxide will continue to grow [153].

Anodic oxidation can also be used to increase oxide layer thickness in order to increase corrosion protection and decrease ion release [154]. It is also used in coloration and porous coating formation [155]. The structural and chemical properties of the anodically formed oxides can be varied over quite a wide range by altering the process parameters, such as anode potential, electrolyte composition, temperature, and current[153].

In 2001, Grimes and co-workers first reported formation of uniform TiO<sub>2</sub> nanotubes arrays via anodic oxidation of titanium in an hydrofluoric (HF) electrolyte [152]. Further studies were focused on precise control and extension of the nanotube morphology [156], length and pore size [157] , and wall thickness [19] . Electrolyte composition plays a critical, and as of yet essentially unexplored role in determining the resultant nanotube array nanoarchitecture and, potentially, its chemical composition.



Electrolyte composition, and its pH, determines both the rate of nanotube array formation, as well as the rate at which the resultant oxide is dissolved. In all cases, a fluoride ion containing electrolyte is needed for nanotube array formation. In an effort to shift the band gap of the titania nanotube arrays so that they more fully respond to full spectrum light various doping strategies have been pursued [158-160] including the use of an organic anodization bath, and incorporation of anionic species during the anodization process.

HF solutions have a great tendency to attack glass apparatus and HF resistant materials require high-cost electrochemical systems. Inexpensive electrochemical systems can be employed by

carrying out anodization in electrolytes containing  $\text{NH}_4\text{F}$  in polyhydric alcohols such as glycerol or ethylene glycol.

Moreover, the use of ethylene glycol as a solvent in the electrochemical oxidation of titanium exhibits an extremely rapid titanium dioxide nanotube growth. Much longer and smoother tubes can be grown in such viscous electrolytes. A range of properties of the tubes depend on the tube geometry [146,161-165]. Fluoride containing organic electrolytes permit formation of tubular and nanoporous metal oxide layers. Nanotubes length increases until the rate of oxide formation is equal to the rate of chemical dissolution [156,166].

The oxide layer forms strong barriers which prevent movement of electron and ions, which tend to slow the oxidation process since the growth of the oxide layer is directly proportional to its resistance. These phenomena slow the whole process until the oxidation process ceases which finalizes the growth mechanism of the nanotubes [167].

## **(b) Other methods of synthesis of $\text{TiO}_2$ nanotubes.**

Several other preparation techniques of  $\text{TiO}_2$  nanotubes have been reported besides anodic oxidation [168]. Electrochemical lithography [169], photoelectrochemical etching[170], sol-gel processing [171], hydrothermal synthesis[172],seeded growth [173] and template synthesis[174-175]. There is growing interest in the synthesis of  $\text{TiO}_2$  nanotubes by electrochemical

anodization due to its preparative simplicity, repeatability, handling and more controllable synthesis than the earlier mentioned methods [176].

TiO<sub>2</sub> nanotubes synthesized by electrochemical anodization are highly ordered with well-defined dimensions, vertically oriented and perpendicular to the substrate. Furthermore, TiO<sub>2</sub> nanotubes prepared by electrochemical anodization are already directly connected to a conductive substrate, titanium which is an advantage for several applications.

## 1.9 Aim and objectives

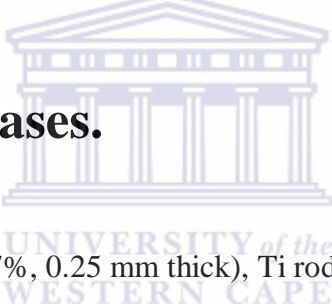
The aim of this research was to synthesize and characterize TiO<sub>2</sub> nanotubes .A further aim was to attempt to reduce the band gap of the TiO<sub>2</sub> nanotubes by non-metal doping. The research was carried out in terms of the following objectives:

1. To construct and test an electrolytic cell for the synthesis of TiO<sub>2</sub> nanotubes by anodic oxidation of titanium.
2. To characterize the TiO<sub>2</sub> nanotubes using SEM, TEM, XRD, RBS, CV and UV/Vis DRS.
3. To reduce the TiO<sub>2</sub> nanotubes both electrochemically and photochemically.
4. To study the electrochemical reduction process by CV.
5. To attempt to dope the reduced TiO<sub>2</sub> nanotubes with nitrogen by annealing in nitrogen gas.

# CHAPTER 2

## EXPERIMENTAL METHODS

### 2.1 Chemicals and gases.



High-purity titanium {Ti} foil (99.7%, 0.25 mm thick), Ti rod (3.8 mm diam., 99.7%), platinum {Pt} (wire, 0.5 mm diam. 99.9% metal basis and gauze, 52 mesh, 99.9%), ethylene glycol {EG} (anhydrous, 99.8%), methylene blue {MB}, N,N-dimethylformamide {DMF} (anhydrous, 99.8%), acetonitrile {ACN} (anhydrous, 99.8%), ammonium fluoride {NH<sub>4</sub>F} (99+%) were purchased from Sigma-Aldrich. Copper {Cu} grid (400 mesh) were purchased from Agar Scientific. Methanol {MeOH} (99.9%), Ethanol {EtOH} (99.9%) were purchased from Kimix and tetrabutylammonium perchlorate {TBAP} (98%), titanium dioxide {TiO<sub>2</sub>} (Degussa P25) from Fluka Analytical. Potassium chloride {KCl} was purchased from B&M Scientific cc. Potassium ferricyanide {K<sub>3</sub>[Fe(CN)<sub>6</sub>]}, Nitric acid {HNO<sub>3</sub>} (55%) and dichloromethane {DCM} (99%) were purchased from Saarchem.

Gases UHP: Nitrogen {N} (99.99%), air (instrumental grade) and argon {Ar} (99.99%) were purchased from Afrox.

## 2.2 Preparation of TiO<sub>2</sub> nanotubes.

TiO<sub>2</sub> nanotubes were prepared by employing an electrochemical anodization cell with titanium foil as the anode and platinum gauze as the cathode in an organic viscous electrolyte containing fluoride ions. The electrolyte solution comprised a small amount of ultra-pure water (2%v/v) and ammonium fluoride (0.3% w/w) in ethylene glycol.

The conditions to synthesize longer nanotubes were chosen based on previously published work, see table 2.1.

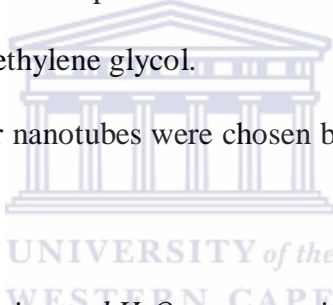


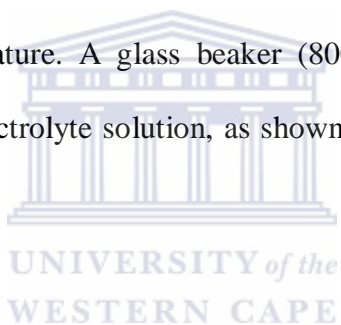
**Table 2.1** Effect of NH<sub>4</sub>F concentration and H<sub>2</sub>O concentration in ethylene glycol electrolyte on the nanotube length, 60 V anodization potential and 17 hours duration [177].

Volume % H <sub>2</sub> O	0.25 wt% NH <sub>4</sub> F	0.30 wt% NH <sub>4</sub> F	0.50 wt% NH <sub>4</sub> F
1	139 μm	156 μm	45 μm
2	177 μm	220 μm	107 μm
3	80 μm	160 μm	142 μm

The electrochemical anodization of titanium was performed using a DC power supply (BK PRECISION, CAT.II MODEL 1715 A, 0–60 V, 0–2 A, 210 W).

Specimens of Ti foil with a size of 4 cm × 2 cm and Pt gauze with size 1.5 cm × 1.5 cm were cut and copper wire was attached to the upper front side of specimens using conductive epoxy adhesive. The electrodes were vertically orientated face to face as shown in figure 2.1.

Prior to electrochemical anodization both electrodes were etched by immersing them in methanol, 6M HNO<sub>3</sub> and ultrapure H<sub>2</sub>O for 5, 10 and 5 minutes, respectively (followed by ultrasonification bath with ultrapure water). Subsequently, they were rinsed with ultrapure water and dried in air at room temperature. A glass beaker (800 cm<sup>3</sup>) was used as a cylindrical electrochemical reactor system electrolyte solution, as shown in figure 2.1. The electrodes were connected to a DC power supply.



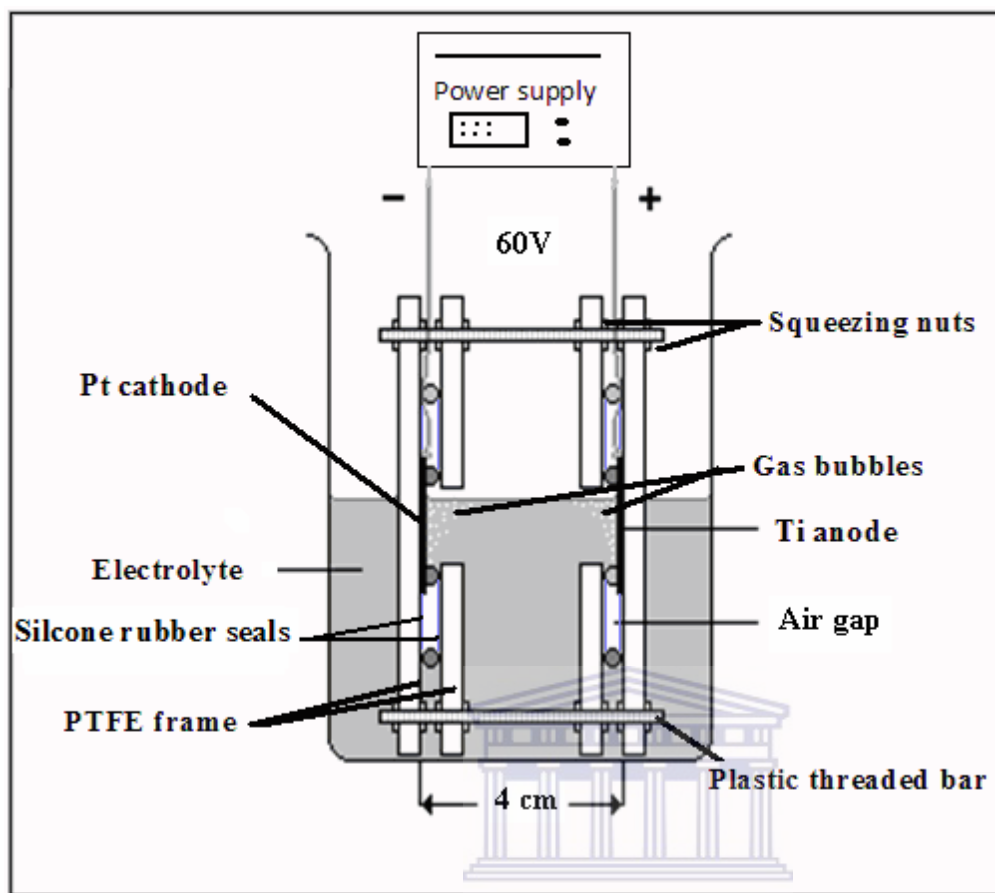


**Figure 2.1** Diagram illustrating the components of the horizontally orientated anodising unit. The system includes a two electrode cell and a power supply.

All anodization experiments were conducted at room temperature (c.a 25°C) at constant 60 V potential for 17 hours using electrodes which were positioned directly 4 cm apart horizontally. As-anodized TiO<sub>2</sub> film were immediately rinsed with ethanol and/or ultrapure water after electrochemical anodization treatment and then dried at room temperature.

Silicone rubber seals were used to make liquid tight seals and they were arranged in a manner that allows only faces of the electrodes to be exposed to the electrolyte. If electrodes were suspended in the electrolyte without the PTFE frame and silicone rubber seals the TiO<sub>2</sub>

nanotubes were not grown. The electrolyte level was below the top edges of the electrodes to allow the hydrogen (from the cathode) and oxygen (from the anode) to escape, see figure 2.1.

## **2.3 Electrochemical reduction of TiO<sub>2</sub>.**

### **2.3.1 Using electrochemical reduction.**

The electrochemical reduction experiments were performed by reversing the polarity of the electrodes (in figure 2.1) used in anodization with the as-anodized titanium dioxide (Ti/TiO<sub>2</sub> nanotubes) as the cathode with Pt gauze as the anode. All experiments were conducted at room temperature (c.a 25°C) inside a fume cupboard, with an applied constant 3V potential for 3 minutes. The electrodes were positioned 3cm apart. The electrolyte was either DMF or ACN containing 100 mM TBAP as the supporting electrolyte. Samples prepared in DMF were finally washed with DCM to remove absorbed DMF from the reduced Ti/TiO<sub>2</sub> nanotubes.

Cleaning the surface of TiO<sub>2</sub> nanotubes plays an important part in observing clear morphological structure from SEM and TEM. The first pre-treatment of titanium metal is also crucial to the growth of nanotubes without which the nanotubes do not grow. Unwashed Ti surfaces that have debris or finger-prints on the side to be activated will preclude the formation of the nanotubes. Immediately after electrochemical reduction the reduced specimens were washed ultrasonically in ethanol for 3 minutes.

### 2.3.2 Growth of TiO<sub>2</sub> nanotubes on a Ti electrode to be used in cyclic voltammetry studies.

In order to evaluate the electrochemical properties of the nanotubular TiO<sub>2</sub> surface by cyclic voltammetry (CV) a special electrode was required on which the nanotubes were grown.

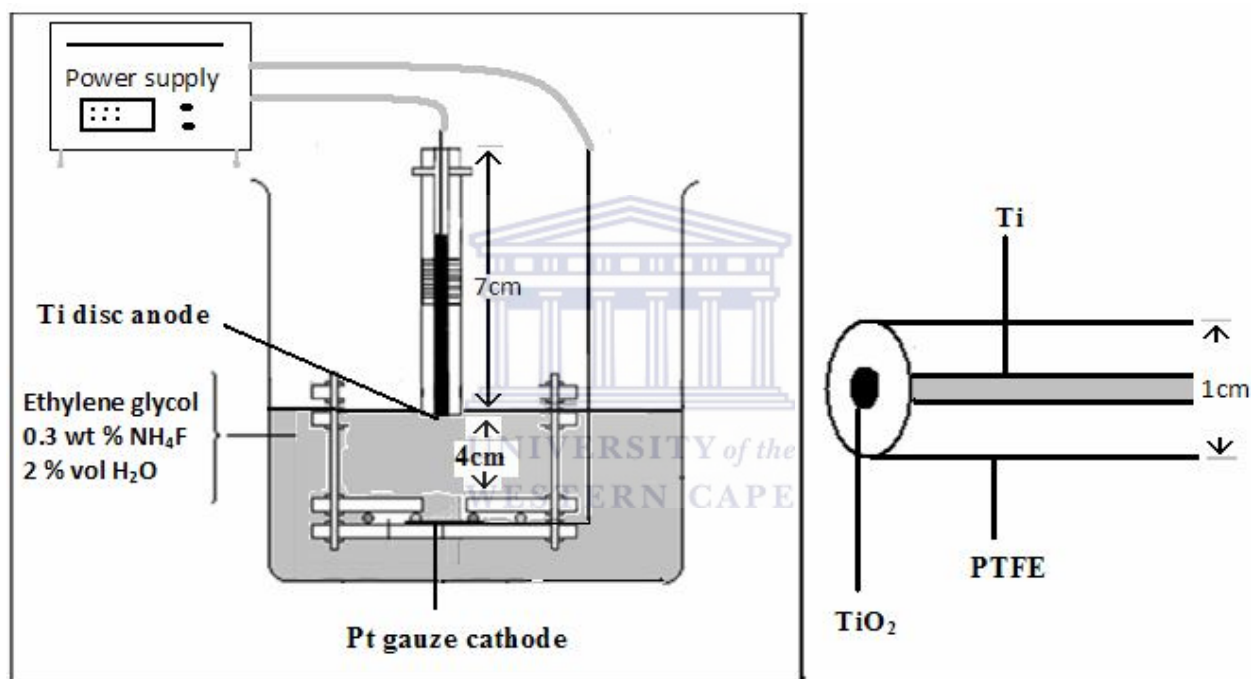


**Figure 2.2** Diagram illustrating the components of the horizontally orientated anodising unit. The system includes a two electrodes cell and a power supply.

A titanium rod anode was enclosed in a removable PTFE sheath with an exposed Ti disc area of 0.08 cm<sup>2</sup>. The cathode was Pt gauze held in the same manner as described in section 2.2 but, the electrodes were vertically spaced. The anode tip was held 4cm above the cathode as shown in figure 2.2.

The conditions of anodization were the same as those described in section 2.2. Immediately after anodization, the as-grown TiO<sub>2</sub> nanotubes on titanium electrode were removed from PTFE sheath while it was wet to avoid the cracking and falling-off of the TiO<sub>2</sub> nanotubes. Cracking and falling-off of the TiO<sub>2</sub> nanotubes produce undesired CV results. The TiO<sub>2</sub> nanotubes on titanium electrode (Ti/TiO<sub>2</sub>) were washed to remove debris and subjected to calcinations after the removal of the PTFE sheath. The electrochemical behavior and surface of an annealed Ti/TiO<sub>2</sub> was then studied and characterized.

### **2.3.3 Cyclic Voltammetry.**

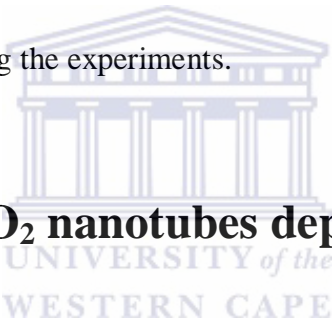
Cyclic voltammetry (CV) can be used in the study of electrode surface reactions, the behavior of electrochemically-active species, and to investigate the nature of substance deposited on the electrode surface. CV is a widely used technique for acquiring information about an electrochemical reaction due to the fact that it provides information on the thermodynamics of redox processes and the kinetics of heterogeneous electron-transfer reactions.

CV entails cycling a potential applied to an electrode immersed in an electrolyte solution, containing analytic species, through a defined potential range and measuring the resultant current [178]. The measured current is a result of electron flow through the electrochemical circuit and is due to diffusional mass transfer of electroactive species as migration and convection are minimized. The applied potential is swept back and forth between two designated potentials at a constant current, by a potentiostat.

Typically a three-electrode system consisting of a working electrode, a reference electrode and a counter electrode is used. The working electrode is the electrode of interest at which a potential is applied. An essential feature of a working electrode is that the electrode should not react chemically with the solvent or solution components.

The counter electrode completes the circuit and is usually Pt wire, graphite or glass carbon [179]. The purpose of the counter electrode is to supply the current required by the working electrode without limiting the measured response of the cell.

The reference electrode experiences zero current and has a known standard potential against which all other potentials are measured. The role of the reference electrode is to provide a fixed potential which does not vary during the experiments.



### **2.3.4 CV studies of TiO<sub>2</sub> nanotubes deposited on a Ti electrode.**

The Ti electrode was used to study electrochemical properties of pure titanium, as-anodized and annealed TiO<sub>2</sub> nanotubes in aqueous (such as 10 mM K<sub>3</sub>[Fe (CN)<sub>6</sub>] in 1M KCl) and /or non-aqueous organic solvents (such as DMF or ACN containing 100 mM TBAP).

CV studies were carried out using an Autolab electrochemical analyser in conjunction with a second potentiostat, (BAS instruments) three-electrode all system and personal computer for data storage and processing. An Ag/AgCl (saturated KCl) /3 M KCl was used as the reference electrode, Pt spiral wire as counter electrode and Ti as the working electrode. All electrolyte

solutions were purged with nitrogen for 10 minutes and the experiments were carried out under a nitrogen atmosphere in the cell, as shown in figure 2.3. Since nitrogen bubbling was essential for removing any oxygen present in the electrolyte that would influence the potential of the redox reaction by acting as an oxidizing agent.

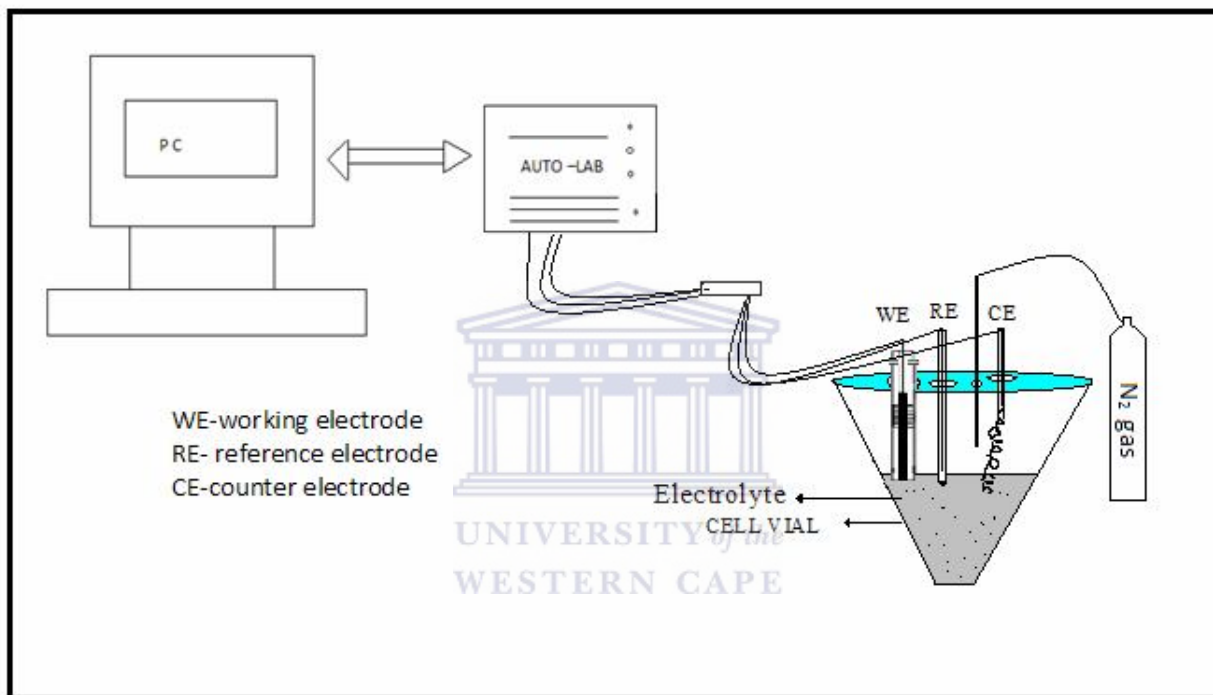


*Figure 2.3* Diagram illustrating the components of CV apparatus. The system includes Autolab electrochemical system in conjunction with a three-electrode(BAS instruments) system and personal computer for data storage and processing.

## 2.4 Photochemical reduction of TiO<sub>2</sub> Samples.

As-anodized TiO<sub>2</sub> nanotubes samples were transferred to a quartz round bottom flask which was connected to condenser while continually purging electrolyte with nitrogen under irradiation with UV light for an hour. The round bottom flask contained 50 ml methanol, boiling chips (glass beads) and a magnetic stirrer bar. The distance between the reaction flask and light source was horizontally fixed at 7cm apart .A UV lamp (HPA 400 W Philips, which emits radiation mainly between 300 and 400 nm) was the radiation source, See figure 2.4.

TiO<sub>2</sub> nanotubes samples were reduced while they were still attached to a Ti substrate in some cases whereas in other cases the TiO<sub>2</sub> nanotubes powders were used.

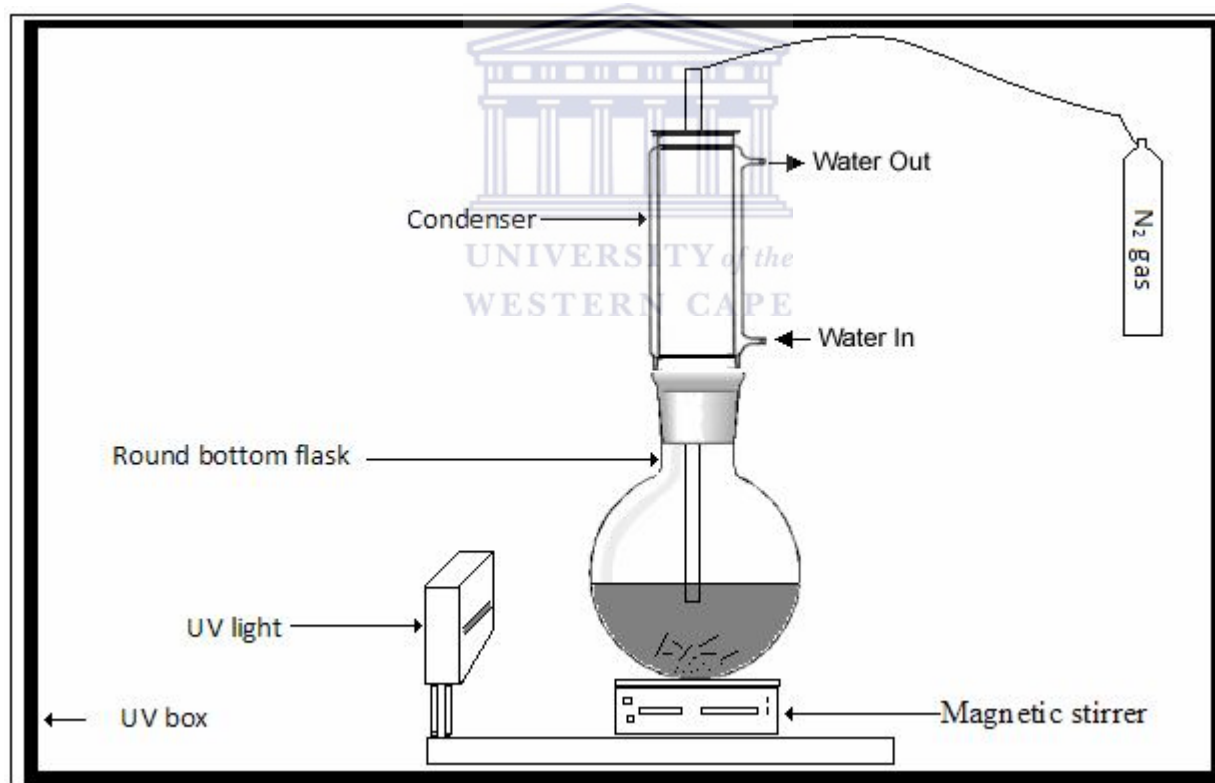


**Figure 2.4** Diagram illustrating the components of photoreduction apparatus.

## 2.5 Doping procedure of TiO<sub>2</sub> nanotubes.

The reduced and non reduced as-grown TiO<sub>2</sub> nanotubes samples were subsequently annealed in various gases (such as nitrogen, air and argon) at temperatures ranging from 280°C to 480°C for 3 hours in a tube furnace (Hecors, NC 2438) at a ramp rate of 4.67°C per minute. The temperature was set from room temperature to its final value (280°C, 380°C, 480°C) and then held constant for 2 hours (dwell time) at the desired treatment temperature using the furnace programme. Some TiO<sub>2</sub> nanotubes samples were calcined while they were still attached to the titanium substrate. The Ti/TiO<sub>2</sub> nanotubes electrode rod was removed from its PTFE sheath while it was wet and washed ultrasonically prior to annealing.

## 2.6 Scanning Electron Microscopy.



Scanning Electron Microscopy (SEM) has many advantages over traditional microscopes. The SEM has a large depth of field, which allows more of a specimen to be in focus at one time. The SEM also has much higher resolution, so closely spaced specimens can be magnified at much higher levels. Because the SEM uses electromagnets rather than lenses, the researcher has much more control in the degree of magnification.

All of these advantages, as well as the actual strikingly clear images, make the scanning electron microscope one of the most useful instruments in research today. The SEM is an instrument that produces a largely magnified image by using electrons instead of light to form an image.

A beam of electrons is produced at the top of the microscope by an electron gun. The electron beam follows a vertical path through the microscope, which is held within a vacuum. The beam travels through electromagnetic fields and lenses, which focus the beam down toward the sample. Once the beam hits the sample, electrons and X-rays are ejected from the sample. The electron induced signals which are produced in SEM can yield a great deal of morphological, physical and chemical information about the specimen.

SEM utilizes vacuum conditions and uses electrons to form an image, special preparations must be done to the sample. All water must be removed from the samples because the water would vaporize in the vacuum. All metals are conductive and require no preparation before being used. All non-metals need to be made conductive by covering the sample with a thin layer of conductive material. This is done by using a device called a "sputter coater".

The sputter coater uses an electric field and argon gas. The sample is placed in a small chamber that is at a vacuum. Argon gas and an electric field cause an electron to be removed from the argon, making the atoms positively charged. The argon ions then become attracted to a negatively charged gold foil. The argon ions knock gold atoms from the surface of the gold foil. These gold atoms fall and settle onto the surface of the sample producing a thin gold coating.

## 2.6.1 Construction of a typical SEM.

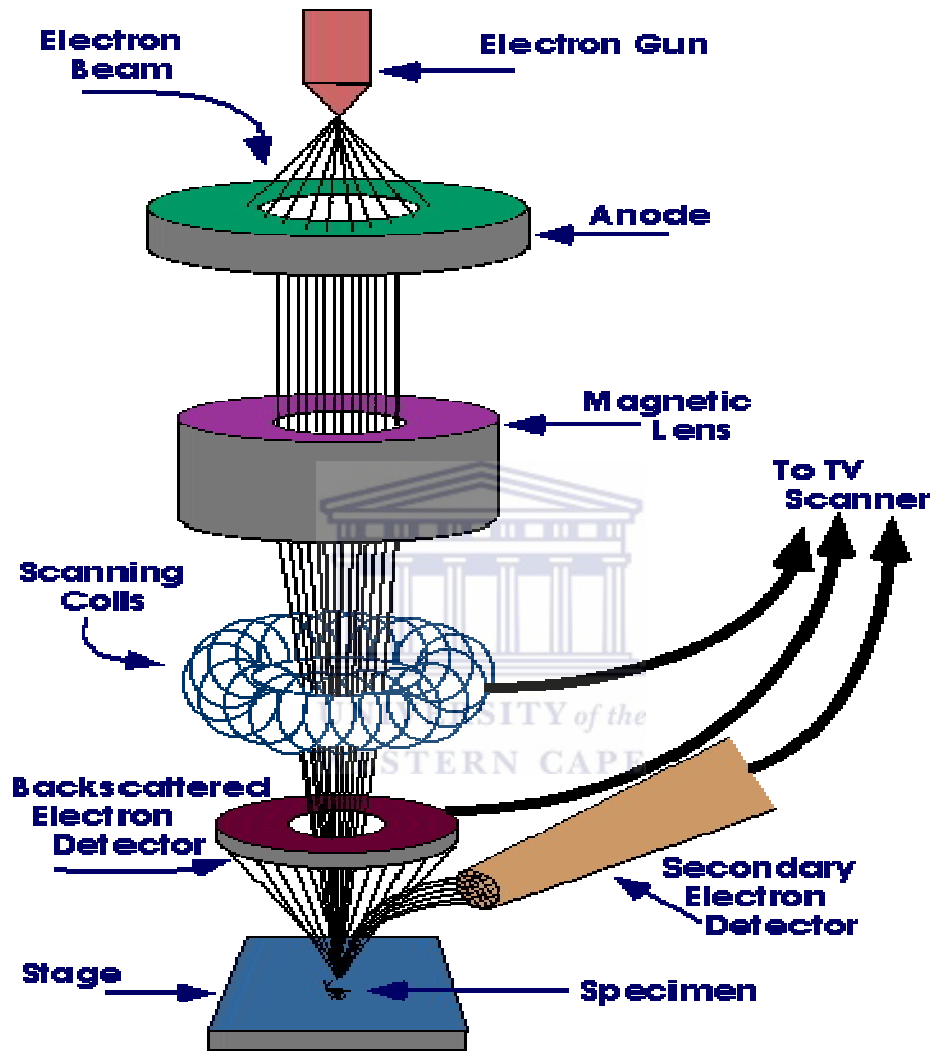
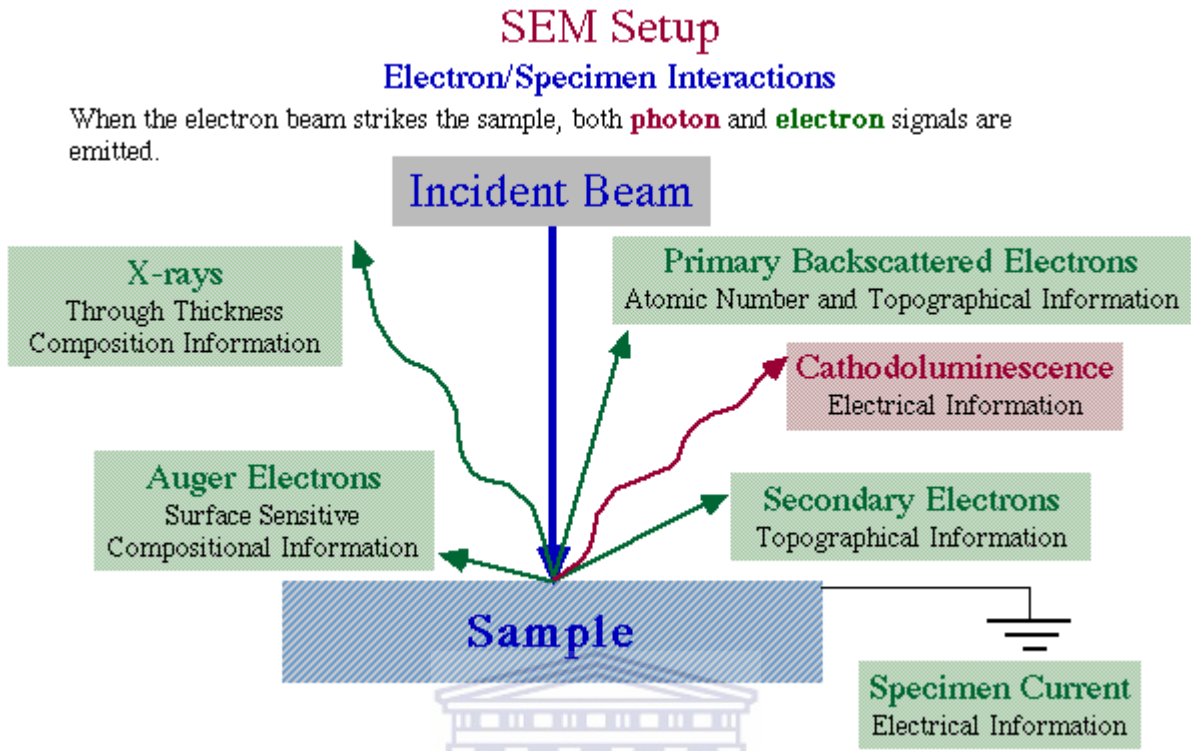
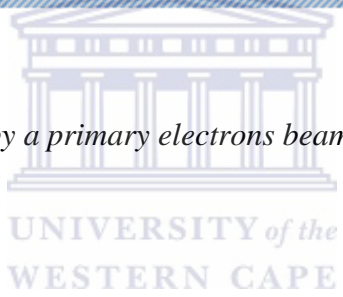


Figure 2.5 Schematic of a SEM [180].



**Figure 2.6** The signals generated by a primary electrons beam-specimen interaction in SEM [180].



A SEM produces surface images by scanning a specimen with a beam of high energy electrons while allows large area of a specimen to be in focus at one time. The electrons interact with the atoms that make up the specimen, producing signals that contain information about the specimen's surface, topography, elemental composition and other properties.

Depending on the instrument, resolution will vary between less than 1 nm and 20 nm. In addition to its high resolving capability, the SEM also has a great depth of field, giving the characteristic three-dimensional appearance that is useful for understanding the surface structure of a specimen.

## **2.6.2 Preparation of TiO<sub>2</sub> nanotubes specimens for SEM studies.**

The as-anodized specimens were examined using a SEM (Hitachi X650). Three different sides (bottom, top-and cross-sectional view) of TiO<sub>2</sub> nanotubes layer were mounted mechanically after being detached from Ti surface followed by coating. SEM was operating with an accelerating voltage 25kV and working distance was 15mm. Magnifications were different for each image taken

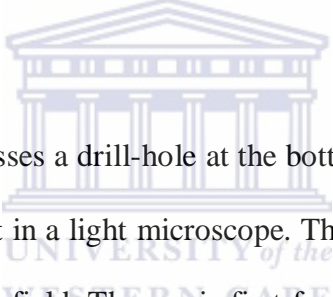
When a specimen is non-conductive a negative charge from the electron beam tends to accumulate on the surface of the specimen, drastically affecting the final image of the sample. For this reason, anodised TiO<sub>2</sub> nanotubes analyzed with the instruments mentioned above were coated with a thin layer (few nm) of gold to eliminate electrostatic charging of the samples, using an Ion Sputtering Device (Edwards Sputter Coater S150B) with the following settings: Coating time was 4 minutes, pressure was  $3 \times 10^{-1}$  Mbar., Current was 30mA and the system was operating at 1 kV.

## **2.7 Transmission Electron Microscopy.**

The transmission electron microscope (TEM) is a scientific instrument that uses electrons instead of light to scrutinize objects at very fine resolutions. The beam of electrons is produced by a pin-

shaped cathode heated up by current. The electrons are vacuumed up by a high voltage at the anode.

The higher it is, the shorter are the electron waves and the higher is the power of resolution. But this factor is hardly ever limiting. The power of resolution of electron microscopy is usually restrained by the quality of the lens-systems and especially by the technique with which the preparation has been achieved. Modern gadgets have powers of resolution that range from 0, 2 - 0, 3 nm. The acceleration voltage was and magnifications were different for each image taken from TEM. Moreover, HR-TEM was still operating at 200 kV and gunlens, spotsizes, C2 aperture and objective aperture used were 1, 3, 3 and 1, respectively.

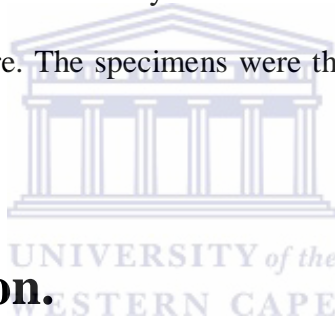


The accelerated ray of electrons passes a drill-hole at the bottom of the anode. Its following way is analogous to that of a ray of light in a light microscope. The lens-systems consist of electronic coils generating an electromagnetic field. The ray is first focused by a condenser. It then passes through the object, where it is partially deflected. The degree of deflection depends on the electron density of the object.

A beam of electrons are focused on a single, pinpoint spot or element on the sample being studied. The electrons interact with the sample and only those that go past unobstructed hit the phosphor screen on the other side. At this point, the electrons are converted to light and an image is formed.

## **2.7.1 Preparation of TiO<sub>2</sub> nanotubes specimen for TEM studies.**

The surface morphology of the TiO<sub>2</sub> nanotubes were further characterized using TEM (Hitachi H-800) and HR-TEM (Tecnai, G2 F20 X-Twin MAT). Specimens were prepared by first detaching oxide film (by washing with plentiful of ultrapure water (about 300ml) and dried in room temperature in order to permit cracking and falling off of TiO<sub>2</sub> nanotubes) from titanium substrate. Specimens were suspended in ethanol followed by sonification. Specimens were transferred into Holey carbon film double layer 400 mesh copper grids (sample holder) and allowed to dry at room temperature. The specimens were then characterized by both TEM and HR-TEM.



## **2.8 X-Ray Diffraction.**

X-ray diffraction (XRD) is a rapid analytical technique primarily used for phase identification of a crystalline material and can provide information on unit cell dimensions. The analyzed material is finely ground, homogenized, and average bulk composition is determined. XRD is a common technique for the study of crystal structures and atomic spacing.



**Figure 2.7** Bruker-Axs D8 advance XRD.

XRD consist of three basic elements: an X-ray tube, a sample holder, and an X-ray detector. X-rays are generated in a cathode ray tube by heating a filament to produce electrons, accelerating the electrons toward a target by applying a voltage, and bombarding the target material with electrons.

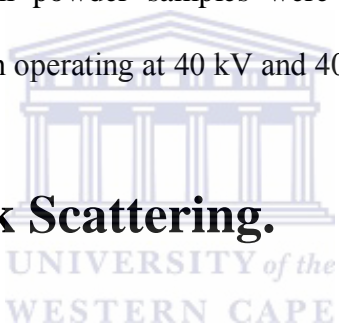
When electrons have sufficient energy to dislodge inner shell electrons of the target material, characteristic X-ray spectra are produced. These X-rays are collimated and directed onto the sample. As the sample and detector are rotated, the intensity of the reflected X-rays is recorded. When the geometry of the incident X-rays impinging the sample satisfies the Bragg's equation

( $n\lambda = 2d \sin\theta$ ), constructive interference occurs and a peak in intensity occurs. A detector records and processes this X-ray signal and converts the signal to a count rate which is then output.

### **2.8.1 Preparation of TiO<sub>2</sub> nanotubes specimen for XRD studies.**

Approximately 100 mg of TiO<sub>2</sub> nanotubes were detached from titanium substrate and ground to a fine powder. Prior to detachment all samples were subjected to various thermal, electrochemical and photochemical treatments. All powder samples were characterized by Bruker-Axs D8 advance XRD with Cu K $\alpha$  radiation operating at 40 kV and 40 mA.

## **2.9 Rutherford Back Scattering.**



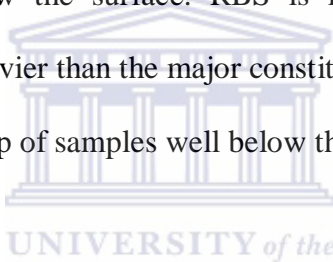
Rutherford Backscattering Spectrometry (RBS) is an accelerator based technique for qualitative composition analysis of thin layers or near surface regions of solids. It is based upon the elastic two-particle scattering of energetic ions with sample atoms via the repulsive Coulomb force of the positively charged atomic nuclei.

The energy distribution of backscattered ions comprehends information about the depth dependence of the elemental composition in a depth range of typical 1  $\mu\text{m}$  below the surface. A well collimated beam of monoenergetic ions is directed to the sample. Usually light ions of H, He or Li with energies in the low MeV region are used. The ions penetrate into the matter and

lose their kinetic energy, at the beginning mainly in collisions with electrons until they come to rest in a depth of several micrometers.

Only near the end of the range nuclear stopping dominates. Near the surface a very small fraction of the ions approach atomic nuclei near enough to be scattered at large angles. Backscattered ions can leave the sample and reach a particle spectrometer, where their energy is analyzed.

The specimen under study is bombarded with monoenergetic beam of  $^4\text{He}^+$  particles and the backscattered particles are detected by the detector-analysis system which measures the energies of the particles. With this information, it is possible to determine atomic mass and elemental concentrations versus depth below the surface. RBS is ideally suited for determining the concentration of trace elements heavier than the major constituents of the substrate. Its sensitivity for light masses, and for the makeup of samples well below the surface, is poor.



## **2.9.1 Preparation of $\text{TiO}_2$ nanotubes specimen for RBS studies.**

Samples for RBS studies consisted of a  $1 \text{ cm}^2$ . Ti metal substrate coated with  $\text{TiO}_2$  nanotubes (which had been subjected to various treatments). The final sample products were analyzed by Van De Graaf RBS with program RUMP software. Beam: 2.000 MeV  $^4\text{He}^+$  7.80 uCoul at 121.00 nA, Geometry: IBM Theta: -10.00 Phi: 15.00 Psi: 5.00 ,MCA: Econv: 3.720 142.400 First chan: 0.0 NPT: 478 , Detector: FWHM: 20.0 keV Tau: 5.0 Omega: 1.150, Correction: 1.3000, Irradiation time (sec): 165.

## 2.9.2 Calculation Method based on RBS.

How to calculate stoichiometry of doped TiO<sub>2</sub> based on RBS results. As-anodized TiO<sub>2</sub> nanotubes of sample E1 in section 3.7 (table 3.8) is used as an example.

Ti (wt %) = 58.65 (obtained from RBS results)

By assuming an un-doped TiO<sub>2</sub>

$$\text{Ti} + \text{O}_2 = \text{TiO}_2 = 100 \text{ wt\%}$$

$$\therefore \text{O}_2(\text{wt\%}) = 41.35$$

$$\text{mol of Ti : } n = m/M_r$$

$$= \frac{58.65\text{g}}{47.87\text{g/mol}}$$

$$= 1.23 \text{ mol}$$



$$\text{mol of O : } n = m/M_r$$

$$= \frac{41.35\text{g}}{15.99\text{g/mol}}$$

$$= 2.59 \text{ mol}$$

Divide each mole value by the smallest number of moles calculated

$$\text{Ti : } \frac{1.23\text{mol}}{1.23 \text{ mol}} = 1.0 \quad \text{and} \quad \text{O : } \frac{2.59\text{mol}}{1.23 \text{ mol}} = 2.1 \approx 2.0$$

Empirical formula is TiO<sub>2</sub>, but for doped TiO<sub>2</sub> is TiO<sub>2-x-y</sub>N<sub>x</sub>C<sub>y</sub>.

$$\therefore \text{O}_2(\text{wt\%}) = \text{O}_{2-x-y}(\text{wt\%}) + \text{N}(\text{wt\%}) + \text{C}(\text{wt\%}) \quad (\text{Equation 2.1})$$

Weight percentages of nitrogen and carbon are 0.18 wt% and 4.31 wt%, respectively. The results come from elemental analyzer.

$$\begin{aligned} \therefore \text{O}_{2-x-y} \text{ (wt\%)} &= 41.35 - 0.18 - 4.31 \\ &= 36.86 \end{aligned}$$

$$\therefore n = m/M_r$$

Ti	O	N	C
<u>58.65g</u>	<u>36.86g</u>	<u>0.18g</u>	<u>4.31g</u>
<u>47.87g/mol</u>	<u>15.99g/mol</u>	<u>14.00g/mol</u>	<u>12.01g/mol</u>
1.23 mol	2.31 mol	0.01 mol	0.36 mol

Divide each mole value by 1.23 moles calculated from TiO<sub>2</sub>.

Ti	O	N	C
<u>1.23</u>	<u>2.31</u>	<u>0.01</u>	<u>0.36</u>
<u>1.23</u>	<u>1.23</u>	<u>1.23</u>	<u>1.23</u>
1	1.88	0.01	0.29

By using the ratios:

$$\therefore \text{O}_{2-x-y} = 2 - 0.01 - 0.29 \quad (\text{from Equation 2.1})$$

$$= 1.7$$

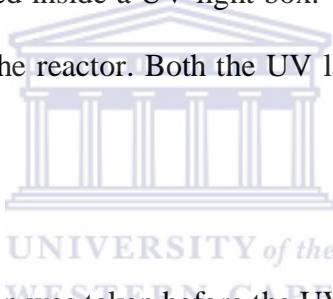
$$\therefore \text{TiO}_{1.7}\text{N}_{0.01}\text{C}_{0.29}$$

## 2.10 Measurement of photocatalytic activity.

Methylene blue (MB), is a dark green powder ( $\epsilon_{660} = 10^5 \text{ dm}^3 \text{ mol}^{-1} \text{ cm}^{-1}$ ) that yields a blue solution when dissolved in water, but will turn colourless if exposed to an oxidizing agent.

(a) In UV light.

300 ml of 10 ppm methylene blue (MB) solution was placed into the photochemical reactor and 50 mg of  $\text{TiO}_2$  (Degussa P25 versus  $\text{TiO}_2$  nanotubes) sample was added as the test catalyst. The reactor was placed in ultrasonic bath for 10 minutes to evenly disperse the catalyst throughout the solution. The reactor was placed inside a UV light box. The reactor system was cooled with water through the outer jacket of the reactor. Both the UV lamp prong and the magnetic stirrer bar were inserted into the solutions.



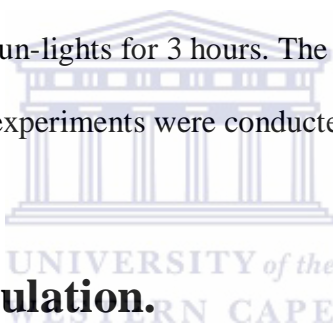
An initial sample of the MB solution was taken before the UV light was turned on. The magnetic stirrer and the lamp were simultaneously switched at the start of the irradiation. Samples were taken (10 ml) from solution at constant time intervals to determine the percentage degradation of MB over time at fixed wavelength (660 nm) and the gradient of MB used was 0.1944. Spectronic 20 was used to measure the absorbance of samples. Samples were centrifuged before the absorbance measurements.

The other experiments were performed in sunlight instead of using UV light and the photocatalytic activity of  $\text{TiO}_2$  nanotubes was compared to that of Degussa P25 ( $\text{TiO}_2$ ).

(b) In sunlight.

300 ml of 10 ppm and 50 ppm MB solutions were placed into 500 ml glass beakers and 50 mg of  $\text{TiO}_2$  (Degussa P25 versus  $\text{TiO}_2$  nanotubes) samples were added as the test catalyst. The glass beaker (sealed with parafilm) was placed in ultrasonic bath for 10 minutes to evenly disperse the catalyst throughout the solution. The glass beakers that were used in experiment were identical and the position of glass beakers was about 500 cm apart.

Samples were initially taken from the solution before they exposed to sunlight. For second time, samples were taken from the solution few minutes (~12 minutes) immediately after ultrasonic bath. Glass beakers were exposed sun-lights for 3 hours. The solutions received the same amount of intensity from the sun since the experiments were conducted simultaneously.



### **2.10.1 Methods of calculation.**

The Spectronic 20 was used to measure the absorbance (Abs). Abs of MB (50 ppm) was measured at fixed wavelength (660 nm) and calibration curve was found to be (0.1944). The concentrations were calculated as follows.

Beer's Law

$$A = \epsilon lc$$

Where  $A$  is absorption,  $\epsilon$  is the molar absorptivity,  $l$  is cell path length (1cm) and  $c$  is a concentration

$$\begin{aligned}
\text{Concentration (c)} &= (\text{Abs}) / (\text{calibration curve}) \\
&= (\text{Abs}) / (0.1944) \\
&= c \text{ (ppm.)} \qquad \qquad \text{(Equation 2.2)}
\end{aligned}$$

Concentration was calculated from each sample and expressed in ppm.

The removal was calculated as  $[1-(c/c_0)] \times 100\%$ , where  $c_0$  is the initial concentration of methylene blue,  $c$  is the concentration of methylene blue after reaction. If standard MB used is 10ppm then  $c_0 = 10\text{ppm}$



$$\begin{aligned}
\% \text{ Degradation of MB} &= \{(c \text{ initial} - c) / c \text{ initial}\} \times 100\% \\
&= [1-(c/c_0)] \times 100\% \qquad \text{(Equation 2.3)}
\end{aligned}$$

## 2.11 UV/Vis Diffuse reflectance spectrophotometry.

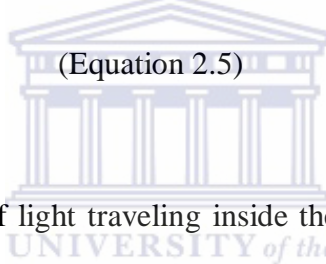
Ultraviolet-visible diffuse reflectance spectrophotometer (UV/ Vis DRS) is a standard technique in the determination of absorption properties of material such as semiconductors. UV/ Vis DRS consist of a broad adsorption bands over a wide range of wavelengths. The reason for this broad adsorption band is that the energy levels of both the ground state and the excited state of a molecule are subdivided into rotational and vibrational sublevels. Electronic transitions may occur

from any one of the sublevels of the ground state to any of the sublevels in the excited states. The inflection in the spectrum is due to the band gap of the semiconductor and can be determined by using UV/ Vis DRS.

The theory on which the derivation of band gap energies from DRS is based was proposed by Kubelka and Munk [181]. Originally they proposed a model to describe the behavior of light traveling inside a light-scattering specimen, which is based on the following differential equations:

$$-di = -(S + K)jdx + Sjdx \quad \text{(Equation 2.4)}$$

$$-dj = -(S + K)jdx + Sidx \quad \text{(Equation 2.5)}$$



Where  $i$  and  $j$  are the intensities of light traveling inside the sample towards its un-illuminated and illuminated surfaces, respectively;  $dx$  is the differential segment along the light path.

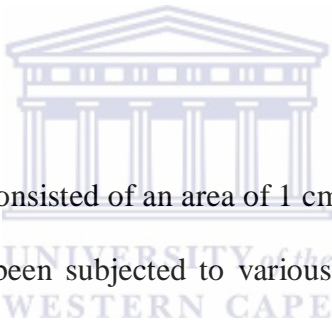
$S$  and  $K$  are the so called K-M scattering and absorption coefficients, respectively. These last two quantities have no direct physical meaning on their own, even though they appear to represent portions of light scattered and absorbed, respectively, per unit vertical length [182]. This model holds when the particle size is comparable to, or smaller than the wavelength of the incident light, and the diffuse reflection no longer allows to separate the contributions of the reflection, refraction, and diffraction (*i.e.* scattering occurs).

In the limiting case of an infinitely thick sample, thickness and sample holder have no influence on the value of reflectance. All these standard methods allow the determination of the absorption

coefficient as a function of wavelength, or at least a variable proportional to the absorption coefficient; it is then possible to use standard techniques to find the band gap. The absorption coefficient also allows the depth distribution of light absorption in the semiconductor to be determined.

The Kubelka–Munk model allows calculation of reflectance from a layer that both scatters and absorbs light [175].

### **2.11.1 Preparation of TiO<sub>2</sub> nanotubes specimens for UV/Vis DRS.**



Samples for UV/Vis DRS studies consisted of an area of 1 cm x 2.5 cm Ti metal substrate coated with TiO<sub>2</sub> nanotubes (which had been subjected to various treatments). TiO<sub>2</sub> nanotubes were directed to the beam of light. The final sample products were analyzed by GBC Centra 404 spectrophotometer with integrating sphere was used to characterize the samples.

### **2.12 X-ray photoelectron spectroscopy.**

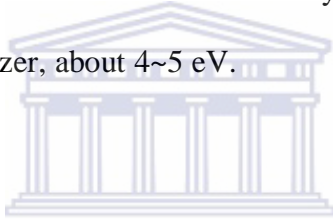
X-ray photoelectron spectroscopy (XPS) is a surface analytical technique, which is based upon the photoelectric effect. Each atom in the surface has core electron with the characteristic binding energy that is conceptually, not strictly, equal to the ionization energy of that electron.

When an X-ray beam directs to the sample surface, the energy of the X-ray photon is adsorbed completely by the core electron of an atom.

If the photon energy,  $h\nu$ , is large enough, the core electron will then escape from the atom and emit out of the surface. The emitted electron with the kinetic energy of  $E_k$  is referred to as the photoelectron. The binding energy of the core electron is give by the Einstein relationship:

$$E_b = h\nu - E_k - \phi$$

Where  $h\nu$  is the X-ray photon energy (for monochromatic Al Ka,  $h\nu = 1486.6$  eV);  $E_k$  is the kinetic energy of photoelectron, which can be measured by the energy analyzer; and  $\phi$  is the work function induced by the analyzer, about 4~5 eV.



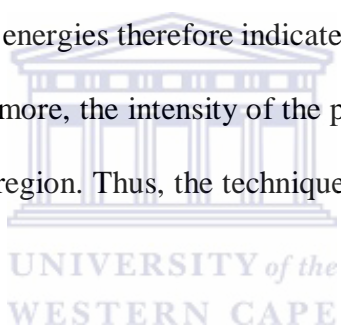
The core electron of an element has a unique binding energy, which seems like a "fingerprint". Thus almost all elements except for hydrogen and helium can be identified *via* measuring the binding energy of its core electron. For each and every element, there will be a characteristic binding energy associated with each core atomic orbital i.e. each element will give rise to a characteristic set of peaks in the photoelectron spectrum at kinetic energies determined by the photon energy and the respective binding energies [183].

The peak areas can be used (with appropriate sensitivity factors) to determine the composition of the materials surface. The shape of each peak and the binding energy can be slightly altered by

the chemical state of the emitting atom. Hence XPS can provide chemical bonding information as well.

The exact binding energy of an electron depends not only upon the level from which photoemission is occurring, but also upon the formal oxidation state of the atom, the local chemical and physical environment. Any changes give rise to small shifts in the peak positions in the spectrum - so-called chemical shifts. The emitted photoelectrons have kinetic energies in the range of *ca.* 0 - 1250 eV.

The presence of peaks at particular energies therefore indicates the presence of a specific element in the sample under study - furthermore, the intensity of the peaks is related to the concentration of the element within the sampled region. Thus, the technique provides a quantitative analysis of the surface composition [184].



### **2.12.1 Preparation of TiO<sub>2</sub> nanotubes specimen for XPS studies.**

The samples were prepared in a similar manner to those in section 2.8.1. Surface analysis and the elemental composition of TiO<sub>2</sub> nanotubes was determined by X-ray photoelectron spectroscopy (XPS, Versaprobe, PHI- 5000 Scanning ESCA Microprobe system) ,the X-ray (Al anode)beam was run at 25 W with 100 μm and the high voltage was kept at 15.0 kV. Scanning X-ray Image

(SXI) images were done with 10  $\mu\text{m}$  1.25 W 15 kV x-ray beam. XPS studies were carried out at University of the Free State, department of Physics.

## **2.13 Elemental analysis.**

Elemental analyzer offers simultaneous multi-elemental determination of light element such as carbon, hydrogen, nitrogen, and sulfur in homogenous micro-samples. The analysis method is based on the complete and instantaneous oxidation of the sample by "flash combustion" which converts all organic and inorganic substances into combustion products. The resulting combustion gases pass through a reduction furnace and are swept into the chromatographic column by the carrier gas which is helium. The gases are separated in the column and detected by the thermal conductivity detector which gives an output signal proportional to the concentration of the individual components of the mixture.

### **2.13.1 Preparation of $\text{TiO}_2$ nanotubes specimen for elemental analysis.**

The samples were prepared in a similar manner to those in section 2.8.1. The sample products were analyzed by Euro-EA elemental Analyser (at Stellenbosch University, department of Soil Science).

## 2.14 Anodization of a titanium alloy.

In an attempt to prepare a layer of nickel titanate  $\text{NiTiO}_3$  an alloy disc of Ti and Ni was prepared. A TiNi (atomic ratio 1:1) alloy was anodized similar way using identical parameters as for the preparation of  $\text{TiO}_2$  nanotubes (section 2.2). The TiNi alloy face had exposed area of  $1 \text{ cm}^2$ .

(a) The following conditions were employed while anodizing TiNi using variable electrolyte compositions while holding other parameters constant.

- (i)  $0.3\text{w/w}\% \text{ NH}_4\text{F} + 2 \text{ v/v}\% \text{ H}_2\text{O}$  in ethylene glycol.
- (ii)  $(50\% \text{ of } 0.3\text{w/w}\% \text{ NH}_4\text{F}) + 2 \text{ v/v}\% \text{ H}_2\text{O}$  in ethylene glycol.
- (iii)  $(25\% \text{ of } 0.3\text{w/w}\% \text{ NH}_4\text{F}) + 2 \text{ v/v}\% \text{ H}_2\text{O}$  in ethylene glycol.
- (iv)  $0.3\text{w/w}\% \text{ NH}_4\text{F}$  in ethylene glycol.

(b) Variation of applied potential was employed while other parameters were constant at an electrolyte composition consisting of  $0.3\text{w/w}\% \text{ NH}_4\text{F} + 2\text{v/v}\% \text{ H}_2\text{O}$  in ethylene glycol.

- (i) 10, 20,30,40,50 and 60 V.

The TiNi alloy dissolved rather than forming a  $\text{NiTiO}_3$  layer on the alloy surface, hence the TiNi alloy was not further investigated.

# CHAPTER 3

## Results and Discussion

### 3.1 SEM and TEM characterization of TiO<sub>2</sub> samples.

#### 3.1.1 Non-reduced samples.

*Table 3.1 Different treatments of non reduced TiO<sub>2</sub> samples for SEM and TEM characterization.*

Samples	Treatments of TiO <sub>2</sub> nanotubes
S1	As anodized.
S2	As anodized → annealed under N <sub>2</sub> at 280°c.

The samples were prepared as films on titanium by anodization at 60V for 17 hours in ethylene glycol containing 2% v/v water and 0.3wt % ammonium fluoride. Immediately, after electrochemical anodization, the TiO<sub>2</sub> nanotubes were washed thoroughly with ethanol in ultrasonic bath in order to remove debris and unblock the pores of the nanotubes. SEM images show detached TiO<sub>2</sub> nanotubes at magnification of 17K, 2.5K and 15K for top view, cross sectional view and bottom view, respectively. The average length of the TiO<sub>2</sub> nanotubes was between 35-50 μm.

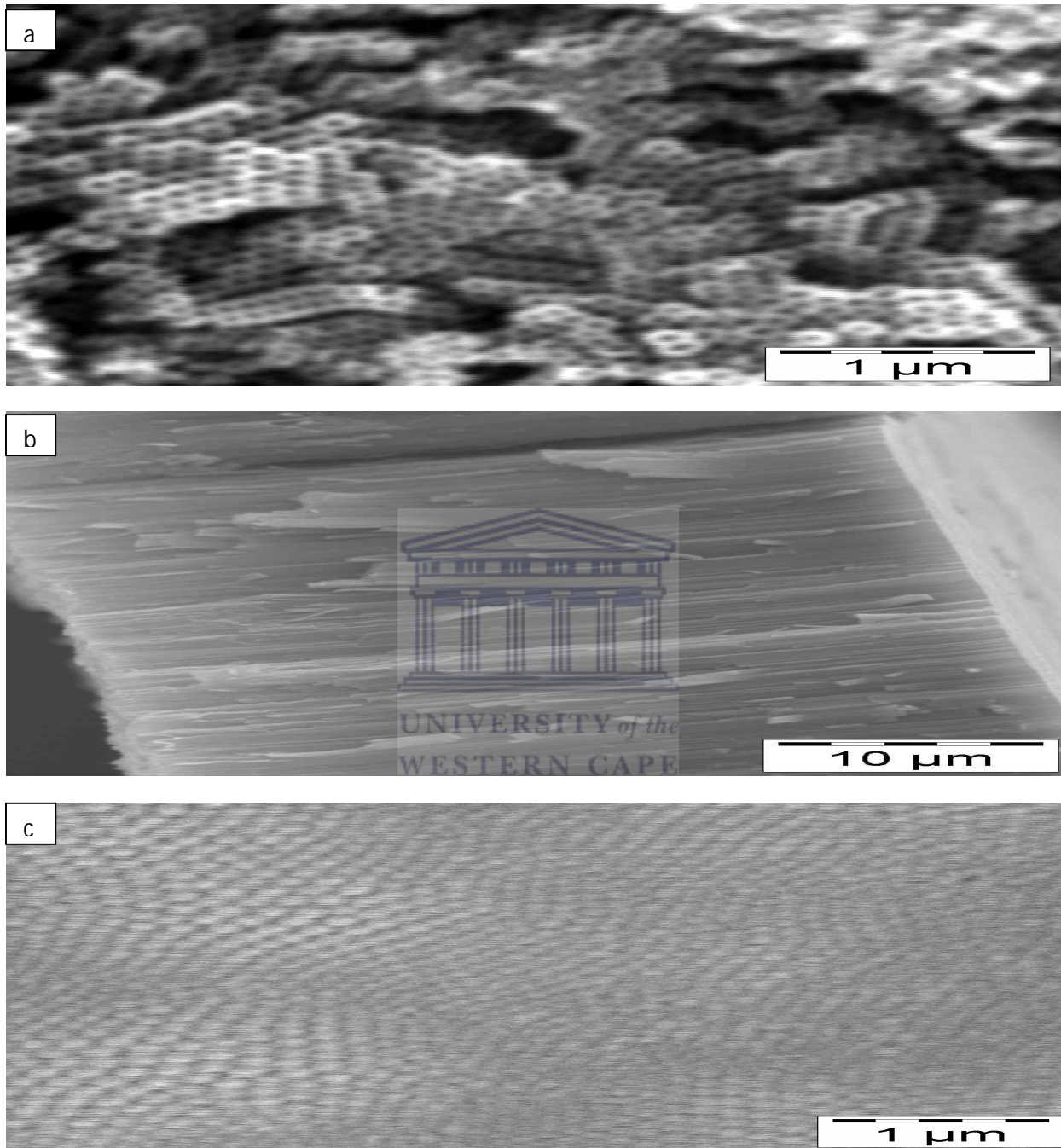


**Figure 3.1** (Sample S1) of  $\text{TiO}_2$  nanotubes, (a) View of face which was not in contact with Ti substrate (top view), (b) Cross sectional view, right side edge in image was that attached to Ti substrate. (c) View of face that was attached to Ti substrate (bottom view).

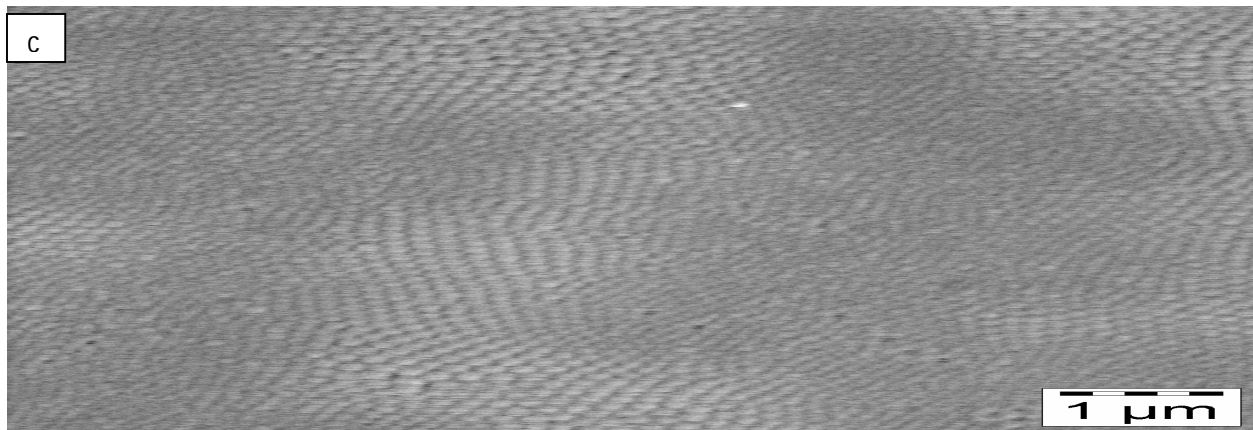
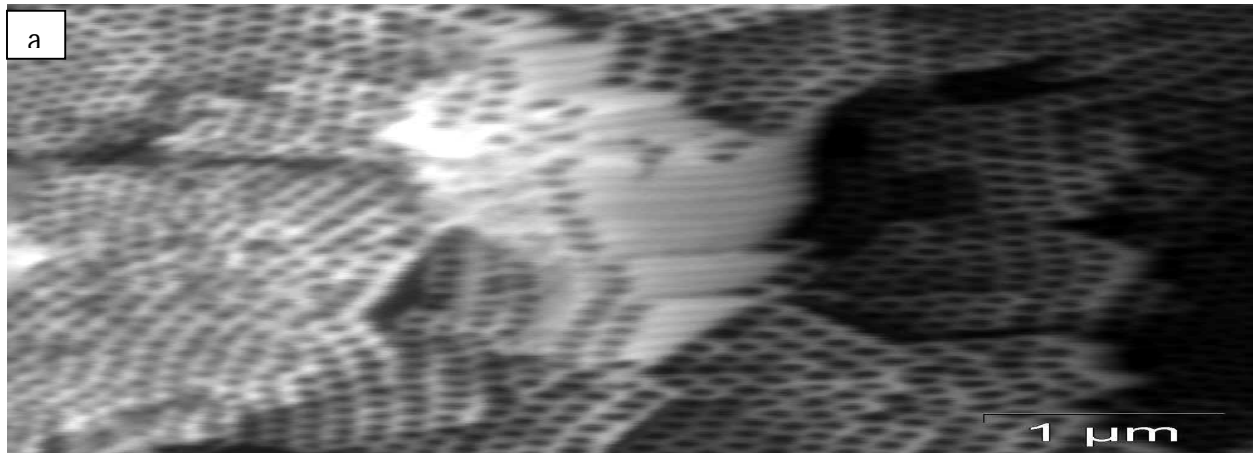


**Figure 3.2** (Sample S2) of  $\text{TiO}_2$  nanotubes, (a) View of face which was not in contact with Ti substrate (top view), (b) Cross sectional view, (c) View of face that was attached to Ti substrate (bottom view).

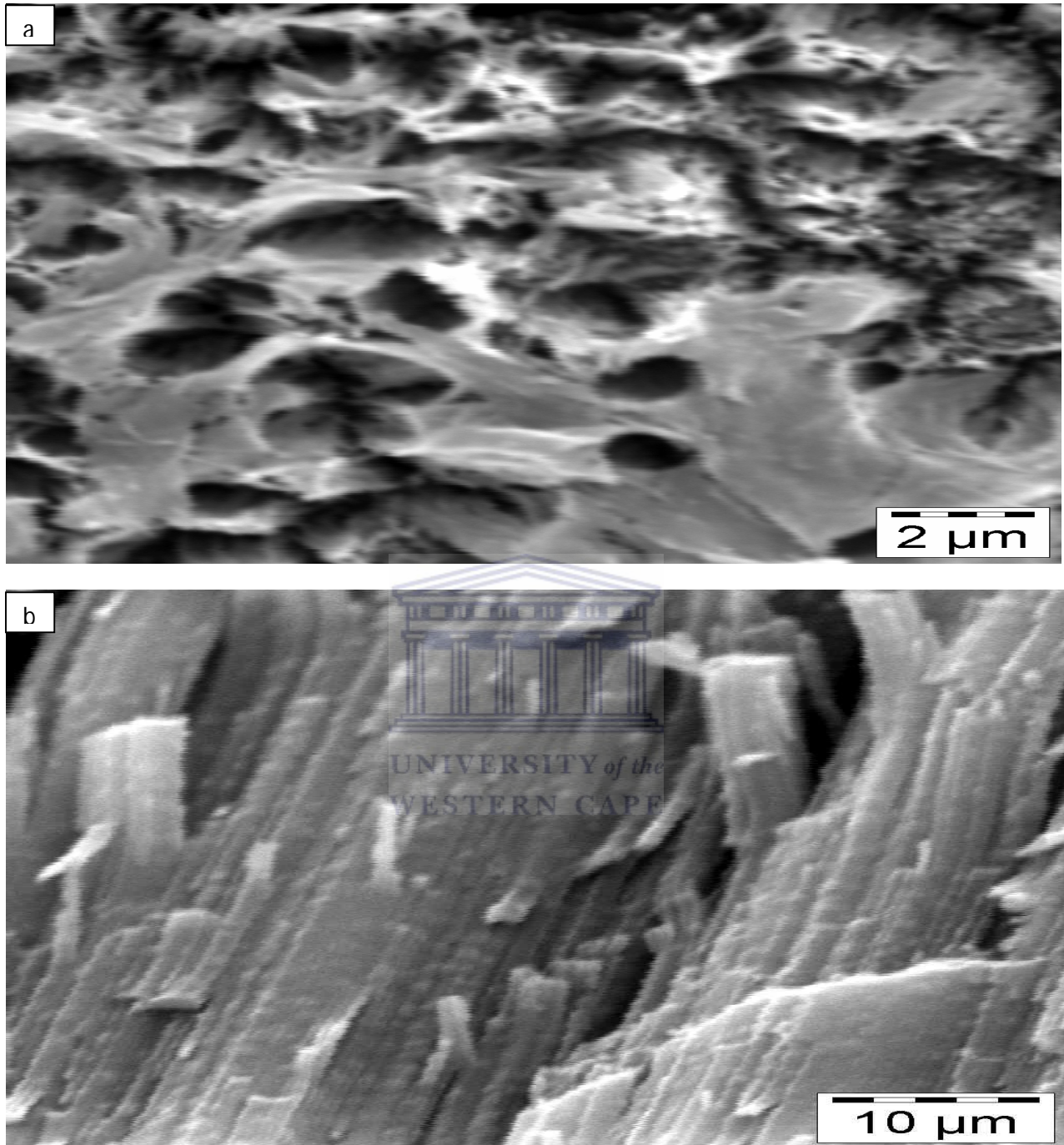


**Figure 3.3** Show SEM images of of TiO<sub>2</sub> nanotubes (a) top view at 15 K magnification and (b) cross sectional view at 7K magnification of sample S1 (that was not washed in ethanol after anodization).

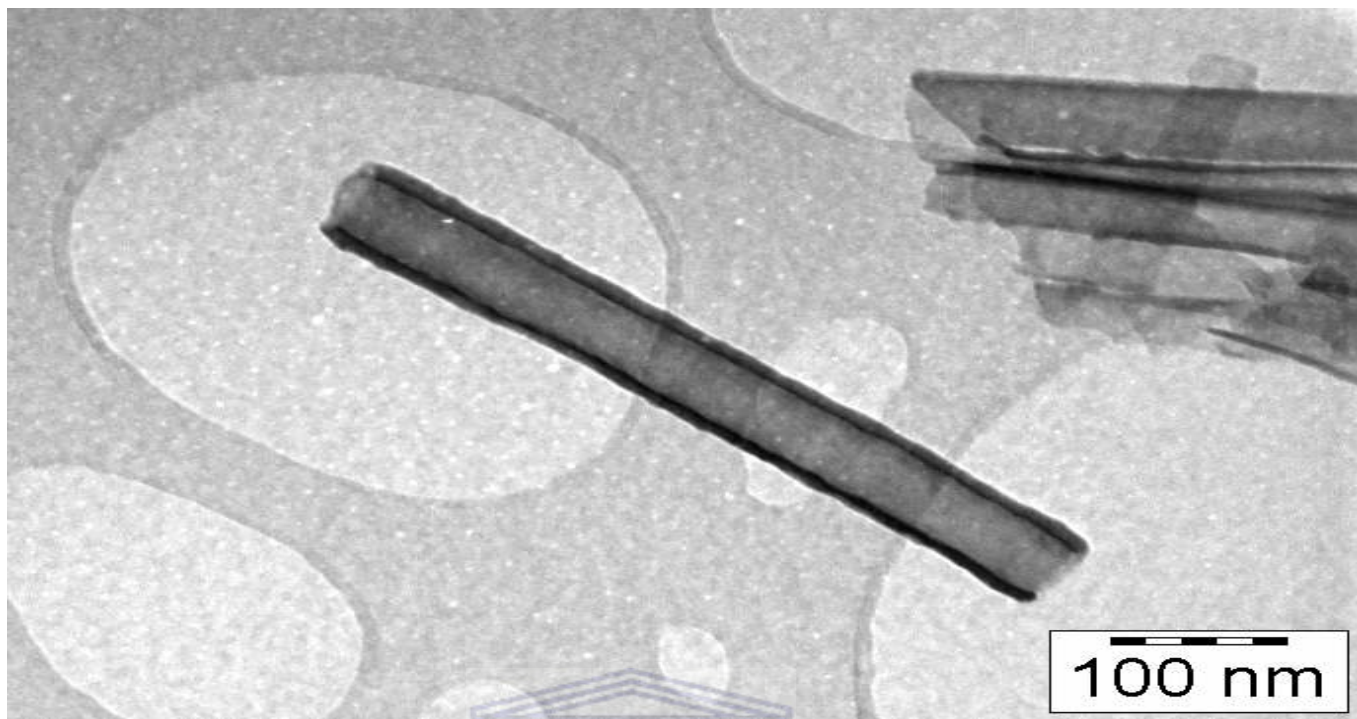


*Figure 3.4 TEM image of (sample S1) TiO<sub>2</sub> nanotubes at 100K magnification.*

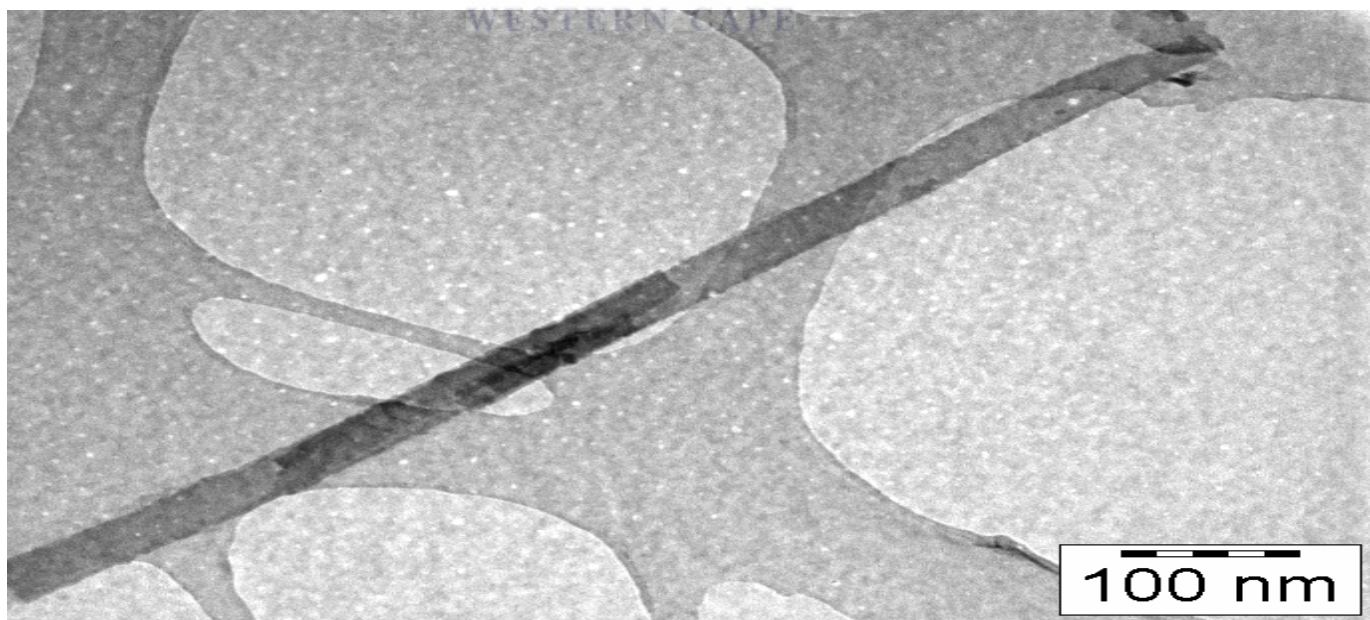


*Figure 3.5 TEM image of (sample S2) TiO<sub>2</sub> nanotubes at 100K magnification.*

Figure 3.1 (a) shows ordered tubular structure with open ends of the tubes which are clearly visible. These tubes are highly ordered but their surface is not uniform. However, it can be seen that all tube diameters and wall thickness are very similar. Figure 3.1(b) shows the closely packed and aligned nanotubes with smooth walls. The average length of the TiO<sub>2</sub> nanotubes is between 35-50 μm, as observed from the cross sectional view.

Figure 3.1(c) shows the uniformly aligned closed ends of the TiO<sub>2</sub> nanotubes. It is apparent that the top ends of the tubes are open and the bottom ends of the tubes are closed, as shown in figure 3.1. These results are similar to those published by K Shankar et al [177].

Figure 3.2 shows a washed TiO<sub>2</sub> nanotube sample that was annealed at 280°C in nitrogen atmosphere. The annealing process did not alter the morphology of TiO<sub>2</sub> nanotubes from top, cross sectional and bottom view, as shown in figure 3.2. Thus the results are similar to those in figure 3.1.

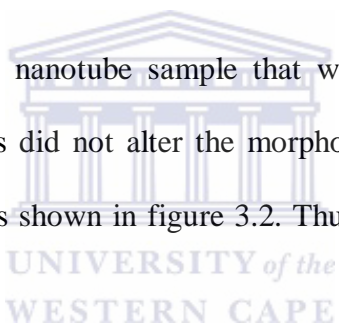
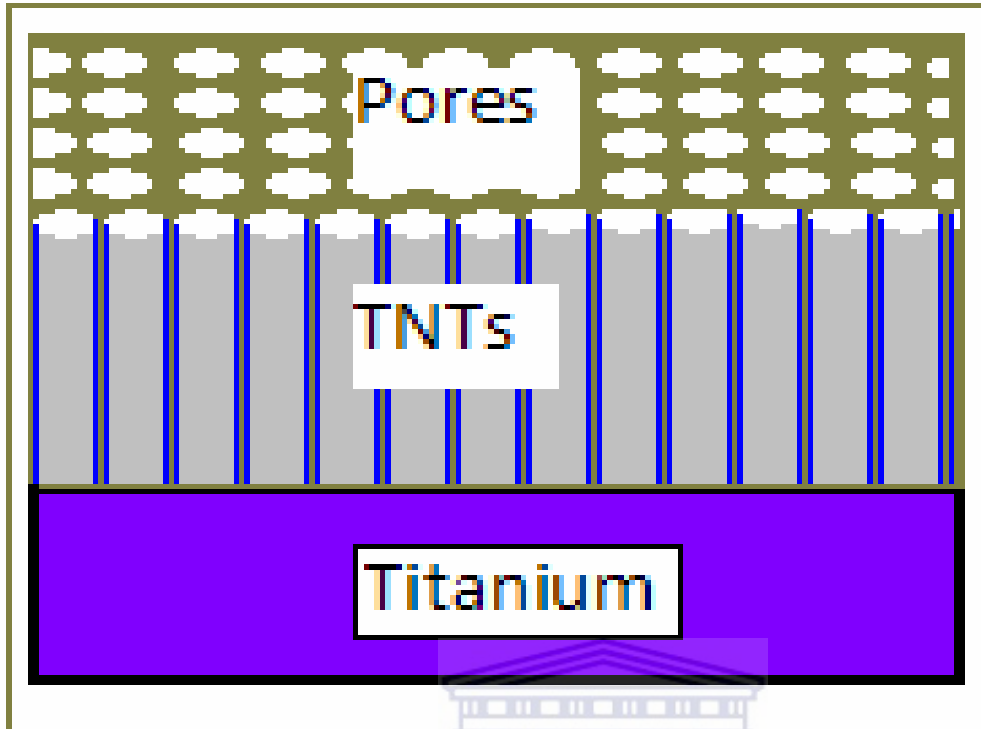


Figure 3.3 shows unwashed sample of TiO<sub>2</sub> nanotube. Most of the tubes are blocked and some form of non-nanotubular material is deposited as a layer on surface of the nanotubes, as shown in figure 3.3(a). However, there are few holes near the ruptured surfaces. Figure 3.3(b) shows TiO<sub>2</sub> nanotube walls which are much rougher as compared to those in figure 3.2(b). However, nanotubes are closely packed and vertically aligned. Thus, the washing treatment plays a major role to unblock the tubes and remove debris from the TiO<sub>2</sub> nanotubes as described in section 2.3.1.

TEM was used in order to determine the diameter and wall thickness of washed TiO<sub>2</sub> nanotubes. TiO<sub>2</sub> nanotubes have an average inner pore diameter of 98 nm and wall thickness of 21 nm. Figure 3.4 shows an amorphous TiO<sub>2</sub> nanotube (sample S1) and figure 3.5 shows an annealed TiO<sub>2</sub> (sample S2). It can be seen that amorphous nanotube sample is thicker than the annealed sample, as shown in figure 3.4 - 3.5. These results are similar to those published by R. Asmatulu et al [185].

### **3.1.1.1 Mechanistic model of TiO<sub>2</sub> nanotubes formation.**

The mechanism of the formation of the TiO<sub>2</sub> nanotubes oxide layer during anodization is still a complex issue, yet a general and simplified model of the chemistry involved is required to understand the growth process, the titanium dioxide nanotubes develop perpendicularly to the metal substrate surface and under controlled conditions, self-organization occurs, as shown in figure 3.6. It has been reported that the outer layer (partly exposed to the electrolyte) has an excess of hydroxyl ions as compared to the inner layer [163], and is considered to be Ti(OH)<sub>4</sub> whereas the inner layer, where de-hydroxylation of the film (water release) has occurred, is represented as TiO<sub>2</sub>.



**Figure 3.6** Shows developing  $\text{TiO}_2$  nanotubes from Ti metal substrate forming a nanotubular like array.

The possible reactions occurring at the anode were as follows.



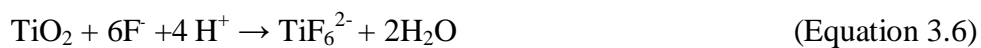
Equation 3.2 and equation 3.3 result in the formation of hydrated oxide and oxide, respectively. The titanium and oxygen ions formed in these redox reactions are driven through the oxide by the externally applied electric field resulting in the formation of the oxide film (equation 3.3). Further oxide is subsequently produced when the hydrated anodic layer releases water by a condensation reaction (equation 3.4). The primary processes responsible for anodic formation of nanoporous alumina [151,186-192] and titanium dioxide [193-196] are similar to each other. Moreover, the following simplified key processes are necessary for the formation of well aligned TiO<sub>2</sub> nanotubes.

- (1) Oxide growth at the surface of the metal occurs due to interaction of the metal with O<sup>2-</sup> or OH<sup>-</sup> ions [151]. After the formation of an initial oxide layer, these anions migrate through the oxide layer reaching the metal/oxide interface where they react with the metal.
- (2) Metal ion (Ti<sup>4+</sup>) migration from the metal at the metal/oxide interface; Ti<sup>4+</sup> cations will be ejected from the metal/oxide interface under application of an electric field that move towards the oxide/electrolyte interface.
- (3) Field assisted dissolution of the oxide at the oxide/electrolyte interface [151, 187]. Due to the applied electric field the Ti–O bond undergoes polarization and is weakened promoting dissolution of the metal cations. Ti<sup>4+</sup> cations dissolve into the electrolyte, and the free O<sup>2-</sup> anions migrate towards the metal/oxide interface, see process (1), to interact with the metal [197-198].

(4) Chemical dissolution of the metal, or oxide, by the acidic electrolyte also takes place during anodization.

In the initial stages of the anodization process field-assisted dissolution dominates chemical dissolution, due to the relatively large electric field across the thin oxide layer [199] formed due to interaction of the surface  $Ti^{4+}$  ions with oxygen ions ( $O_2^-$ ) in the electrolyte, and is seen uniformly across the surface.

The presence of fluoride ions in the electrolyte can chemically react with  $Ti^{4+}$  (equation 3.5) or dissolve the hydrated layer and the oxide (equation 3.6-3.7), the ions being mobile in the anodic layer (field-assisted dissolution), under the applied electric field. Cations move outward from the metal, and anions move inward to the metal, and the oxide grows both at the metal/oxide and oxide/electrolyte interfaces [200]. Small pits formed due to the localized dissolution of the oxide act as pore forming centers, represented by reaction of (equation 3.6).



The reactions strongly suggest that depletion of  $H^+$  and  $F^-$  species in the used solution renders it unable to produce sufficient local acidification at the pore bottom to limit the barrier layer thickness. Ions react with both the metal and the oxide to form a titanium hexafluoride complex

[TiF<sub>6</sub><sup>2-</sup>], which is stable in water and the structure of a nanotubular oxide, has a thin barrier inner layer at the M/MO and a porous outer layer at the MO/Electrolyte interface [152]. The competition between formation of the oxide (equation 3.2-3.4) and its dissolution (equation 3.5-3.7), is a primary step determining the nature of the anodic titanium dioxide structure formed.

The fact that gas evolution occurs at the anode (equation 3.8) implies that this may play a role in determining the morphology of the final structure and cannot be excluded. At the cathode, there was hydrogen evolution, (equation 3.9)



The current is depending on surface area of electrodes that are being used during electrochemical anodization. In case of titanium foil electrode that has area of 4 cm × 2 cm, the initial current was 46 mA at t<sub>0</sub> (initial time = 0 min) and drop to a final current of 8 mA at t<sub>f</sub> (final time = 17 hours). However, when titanium rod electrode (that has area of 0.08 cm<sup>2</sup>) is used in the same conditions, then initial current was 2 mA at t<sub>0</sub> (initial time = 0 min) and drop to a final current of 1 mA at t<sub>f</sub> (final time = 17 hours).

Although the anodizing process has been generally explained, there is still a general lack of understanding how the anodic structure forms and evolves from the early stages to its final tubular morphology. For example, most of the growth model mechanisms assume the structure changes from porous to tubular at a certain point of the anodisation process, although there is no clear evidence of such a transition.

### 3.1.2 Reduced samples.

*Table 3.2 Different treatments of reduced TiO<sub>2</sub> samples for SEM and TEM characterization.*

Samples	Treatments of TiO <sub>2</sub> nanotubes
S1	As anodized → photoreduced in MeOH → annealed under N <sub>2</sub> at 280°c.
S2	As anodized → Electrochemical reduced in DMF -(0.1M)TBAP → annealed under N <sub>2</sub> at 280°c.
S3	As anodized → Electrochemical reduced in ACN -(0.1M)TBAP → annealed under N <sub>2</sub> at 280°c.



The as-anodized samples were prepared as described in section 3.1.1. Subsequently, the as-anodized samples were reduced and annealed as shown in table 3.2. The reduced samples were characterized by using SEM and TEM.

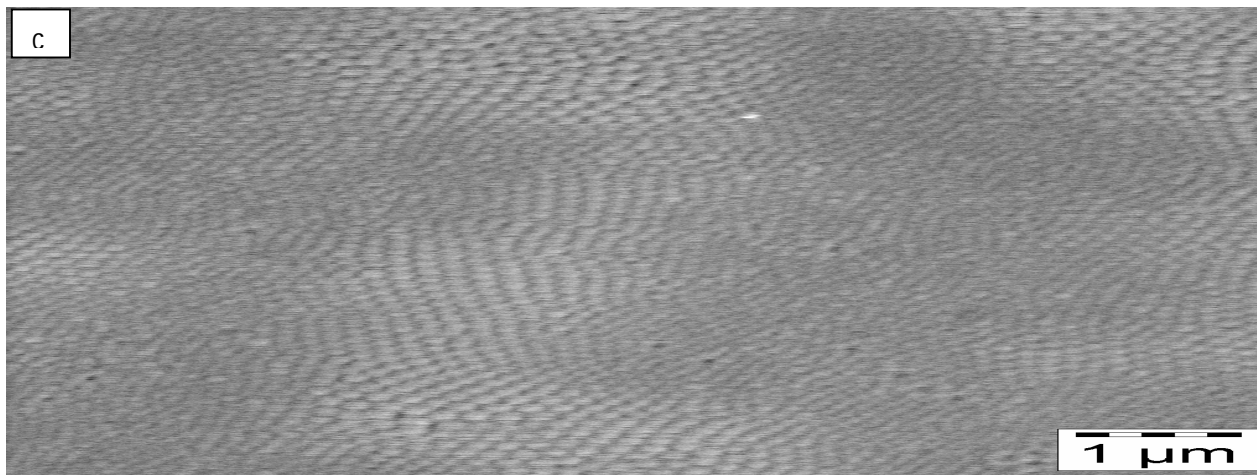
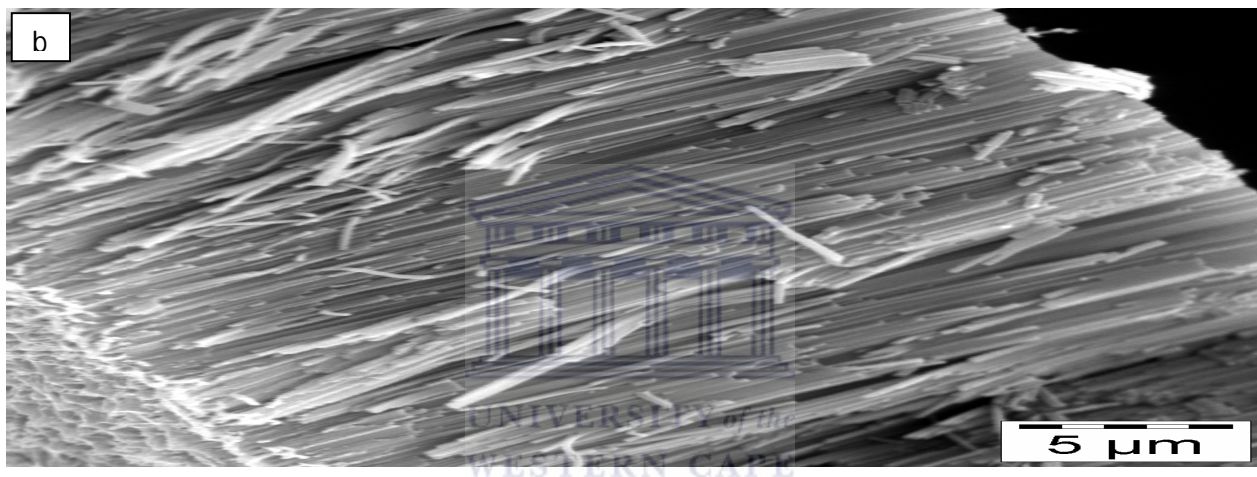
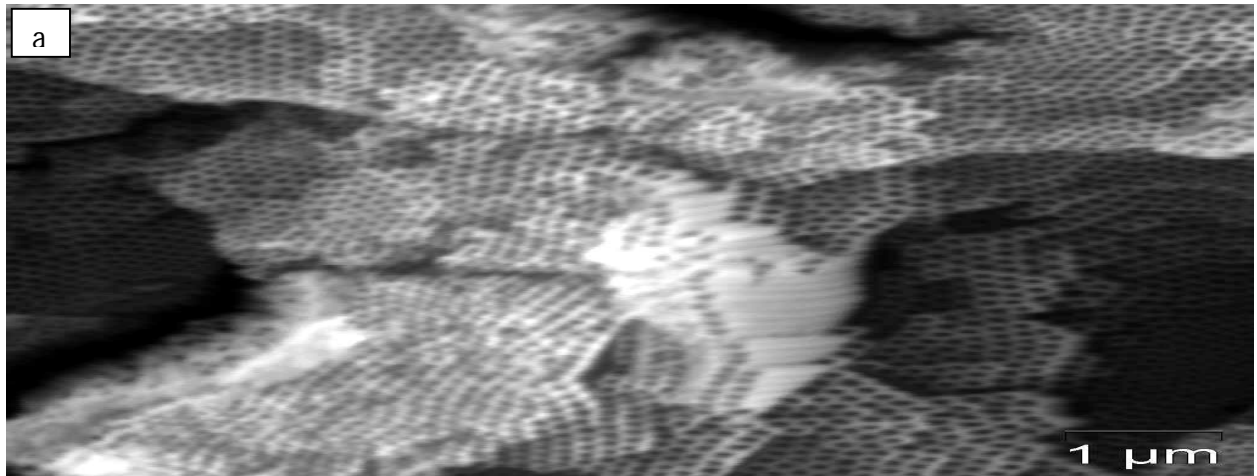


**Figure 3.7** (Sample 1) of  $\text{TiO}_2$  nanotubes, (a) View of face which was not in contact with Ti substrate (top view), (b) cross sectional view, left side edge in image was that not attached to Ti substrate (c)View of face that was attached to Ti substrate (bottom view).

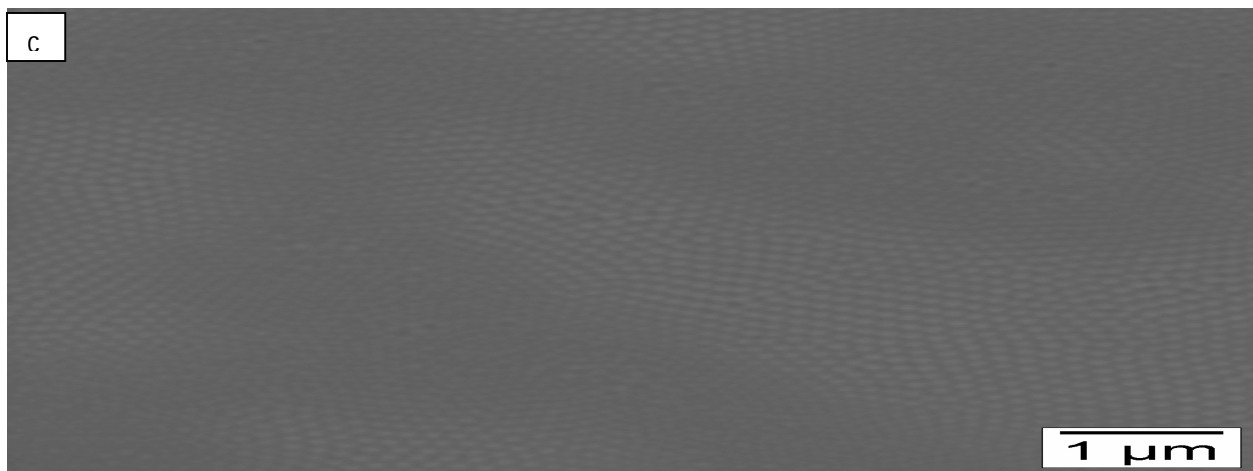
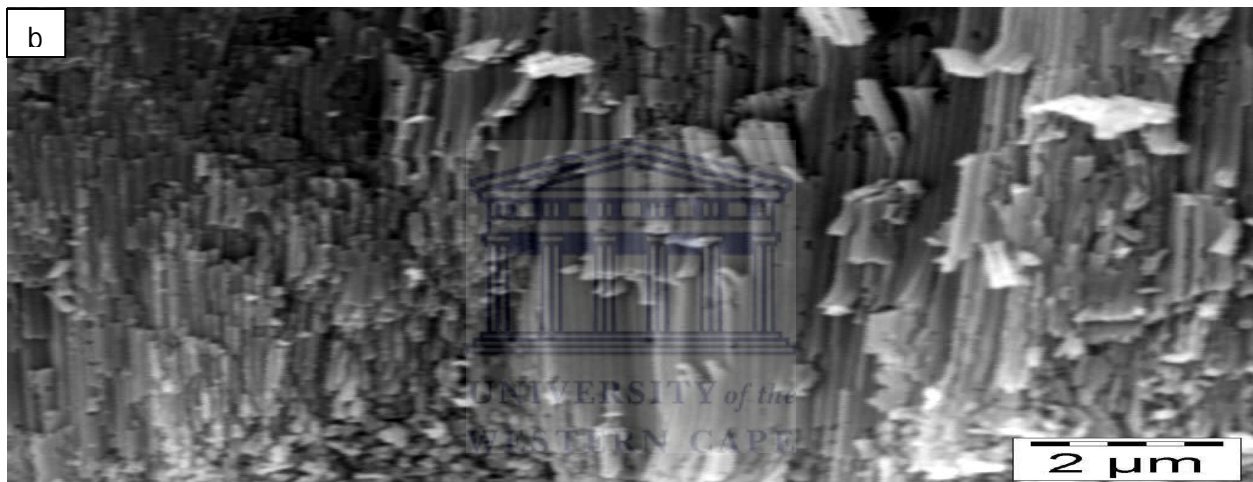
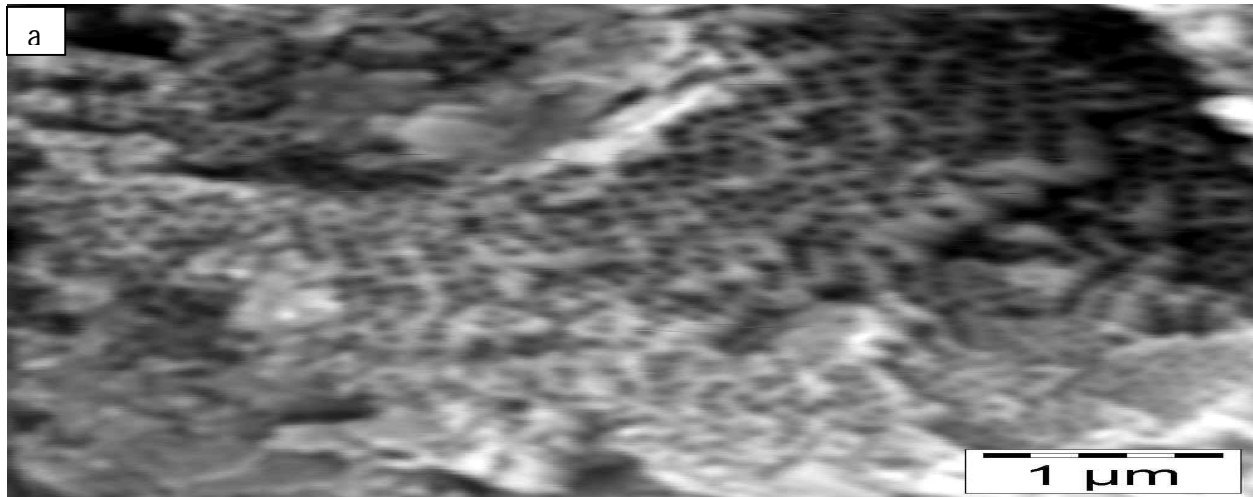


**Figure 3.8** (Sample 2) of  $\text{TiO}_2$  nanotubes , (a) View of face which was not in contact with Ti substrate (top view), (b) cross sectional view, (c)View of face that was attached to Ti substrate (bottom view).

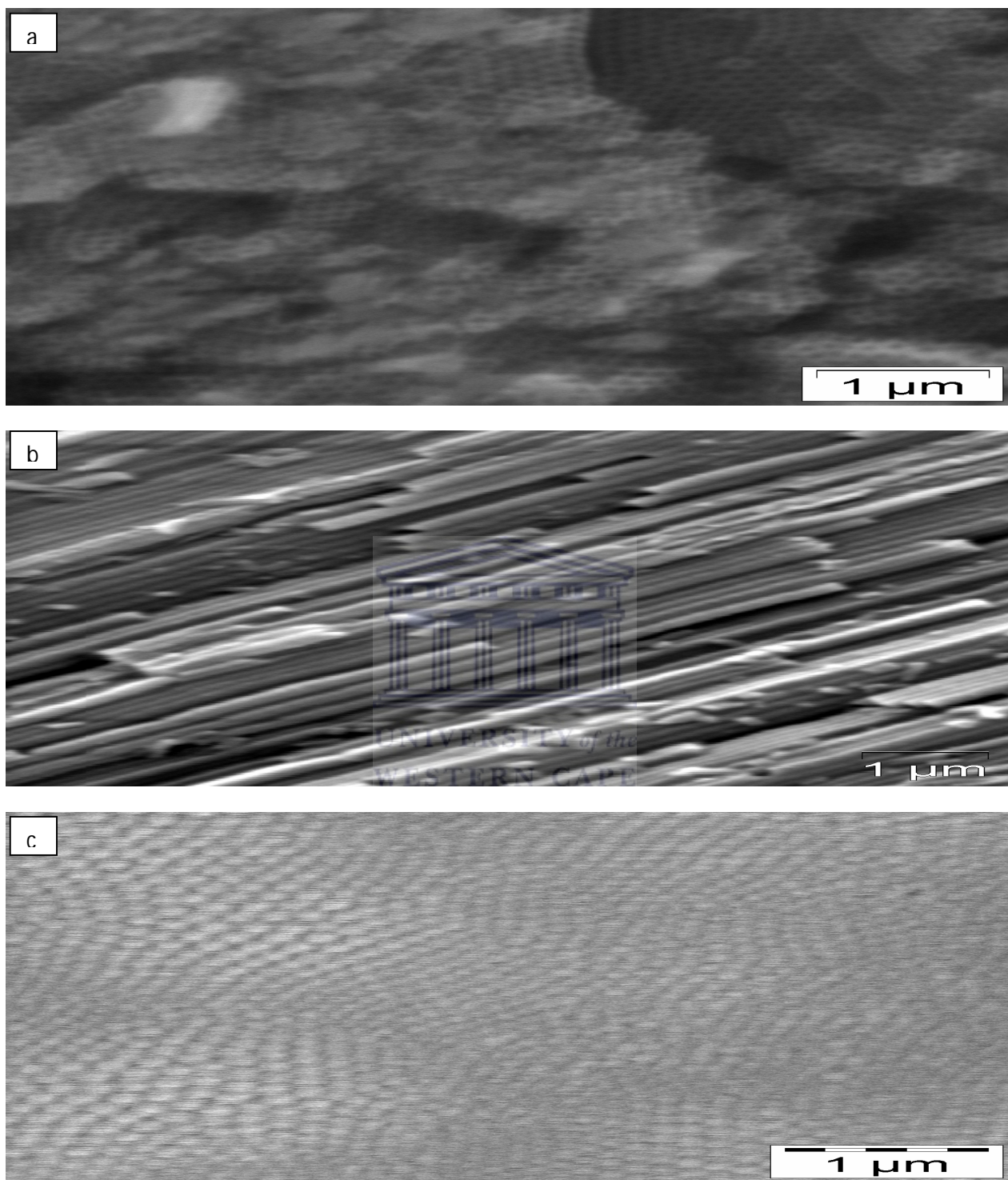


**Figure 3.9** (Sample 3) of TiO<sub>2</sub> nanotubes, (a) View of face which was not in contact with Ti substrate (top view), (b) cross sectional view, (c) View of face that was attached to Ti substrate (bottom view).

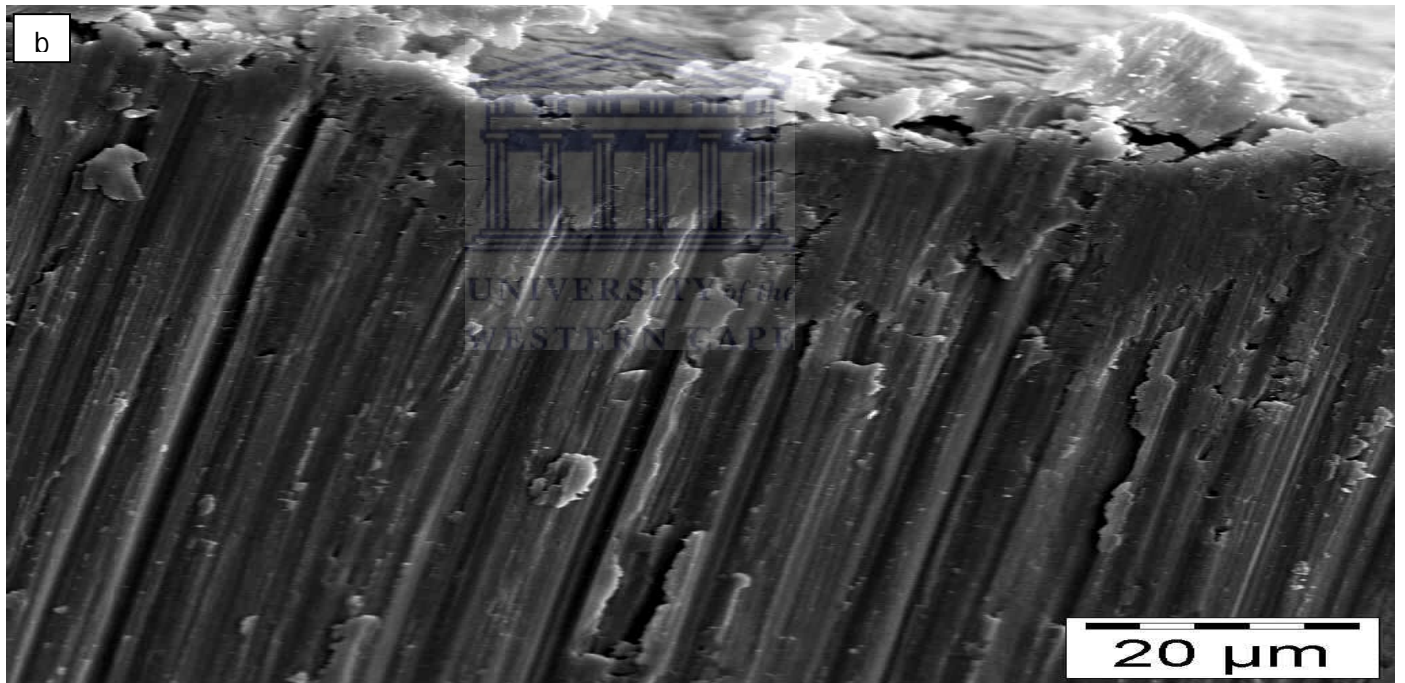
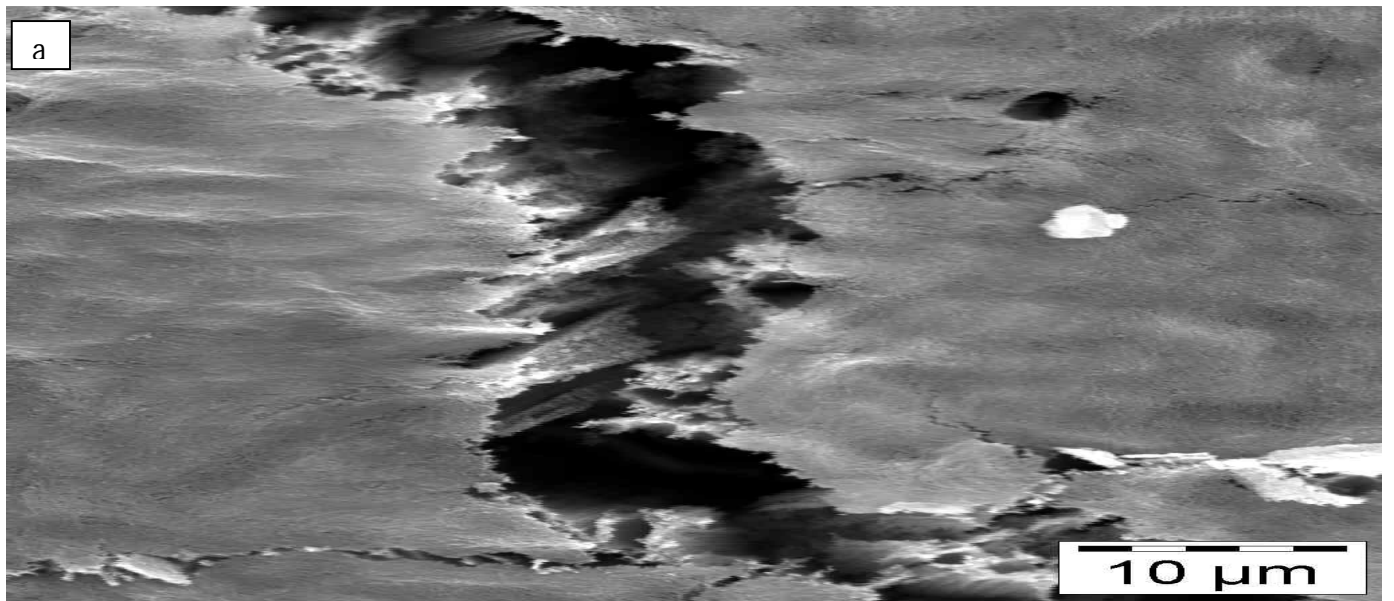


**Figure 3.10** Show SEM images of (a) top view at 13 K magnification and (b) cross sectional and top view at 3.5K magnification of  $\text{TiO}_2$  nanotubes that were reduced in DMF-TBAP electrolyte solution followed by rinsing with DCM (not washed in ethanol after anodization).

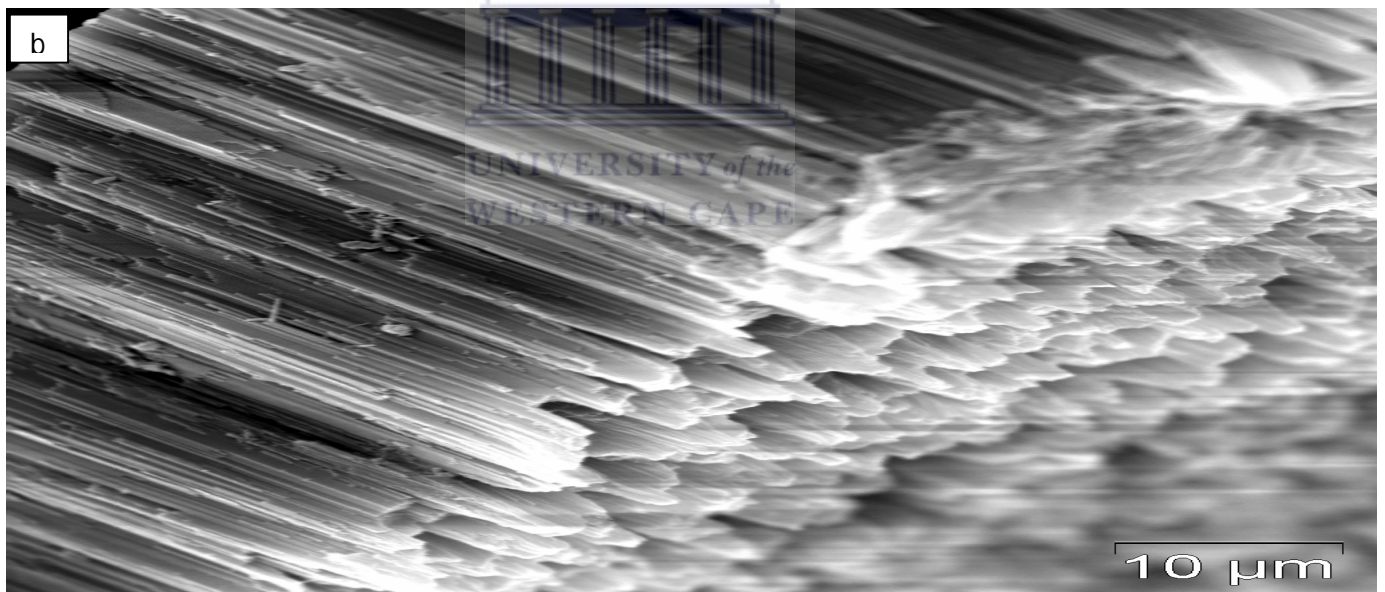
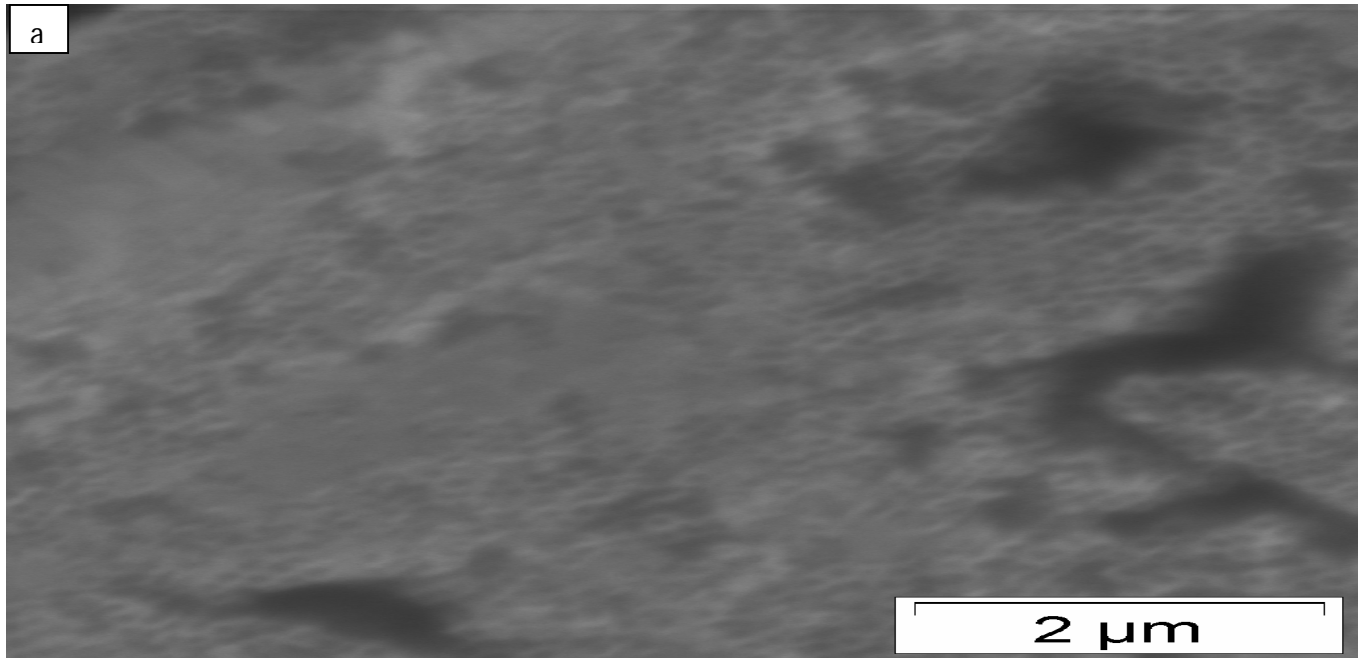


**Figure 3.11** Show SEM images of (a) top view at 15 K magnification and (b) cross sectional view, right side edge in image was that not attached to Ti substrate, at 2K magnification of  $\text{TiO}_2$  nanotubes that were reduced in ACN-TBAP electrolyte solution (not washed in ethanol after anodization).

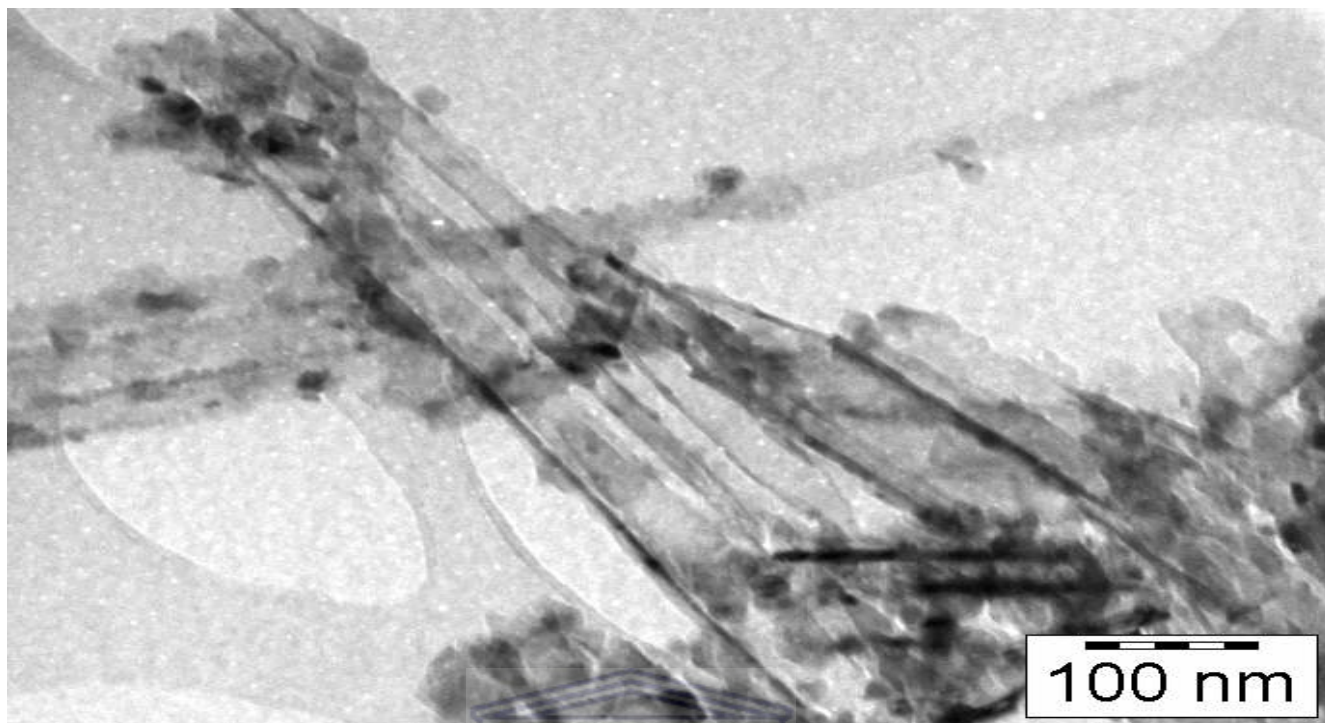


**Figure 3.12** (Sample S3) TEM image of electrochemically reduced  $\text{TiO}_2$  nanotubes in ACN at 100K magnification.

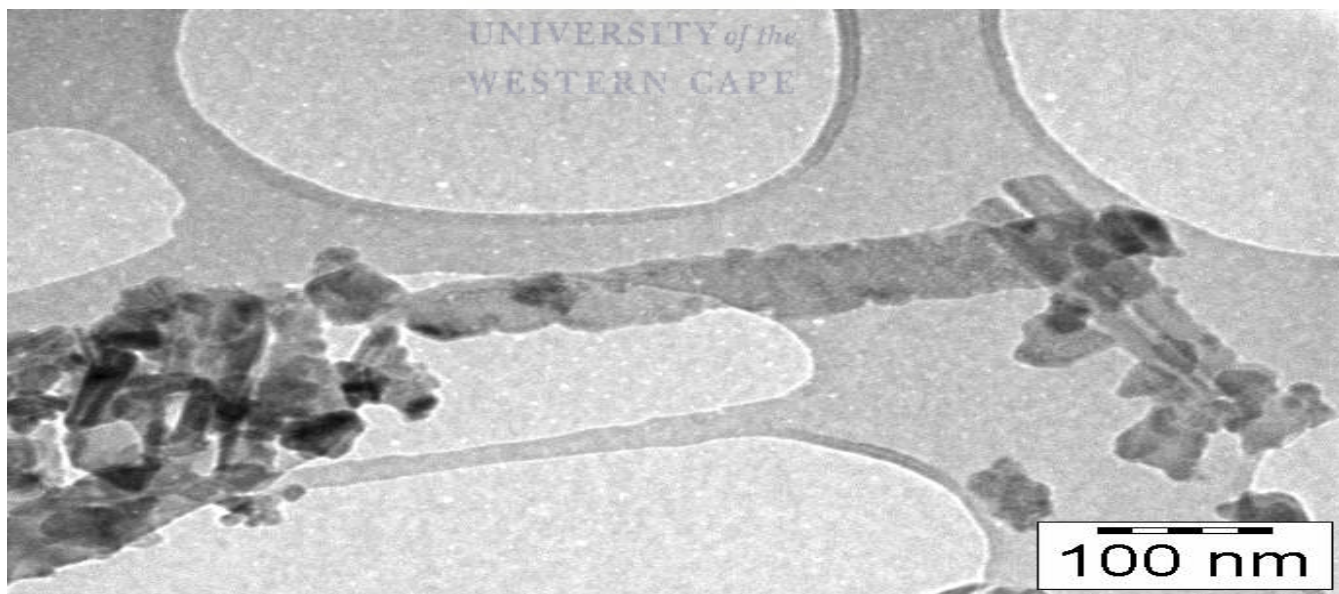


**Figure 3.13** (Sample S3) TEM images of electrochemically reduced (in ACN) and annealed  $\text{TiO}_2$  nanotubes at 100K magnification.

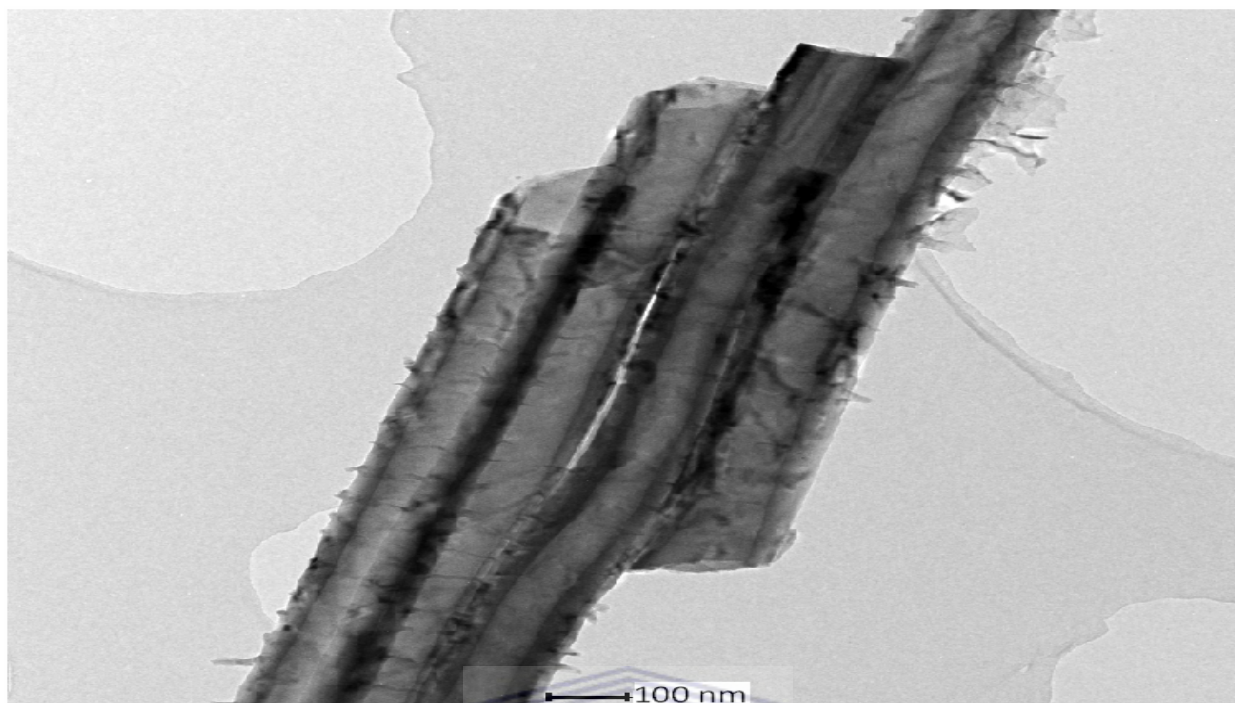


**Figure 3.14** (Sample S3) HR-TEM images of electrochemically reduced in ACN and annealed  $\text{TiO}_2$  nanotubes at 13.5K magnification.

Figure 3.7 (a) clearly shows ordered tubular structure and tube openings of a washed sample. The tubes are highly ordered but their surface is not uniform. However, it can be seen that all tubes and wall thickness are very similar. Figure 3.7(b) shows the closely packed and aligned nanotubes with smooth walls. The left side edge (which was not uniform) was that of a top view which was not attached to Ti substrate.

Figure 3.7(c) shows the closed ends (with a rounded shape) of the  $\text{TiO}_2$  nanotubes without any rupture and they are uniform. It is apparent that the top ends of the tubes are open and the bottom ends of the tubes are closed, as shown in figure 3.7. These results are similar to those in figure 3.1- 3.2.

Figures 3.8-3.9 show the similar results as shown in figure 3.7. However some holes can be seen from broken edge of nanotubes as shown in figure 3.8(b). Thus, both electrochemical and photochemical reductions do not alter the morphology of the TiO<sub>2</sub> nanotubes. SEM results of reduced TiO<sub>2</sub> nanotubes in ACN-TBAP or DMF-TBAP have not been published before.

Photochemical reduction (of sample S1) did not alter the morphology of unwashed TiO<sub>2</sub> nanotubes and no clogged pores were observed, as similar to those in figure 3.7.

The SEM images show that some form of non-nanotubular material is deposited as a layer on surface of the as-anodized TiO<sub>2</sub> nanotubes and the open tubes ends were completely blocked, as shown in figure 3.10(a). Figure 3.10 shows unwashed sample of TiO<sub>2</sub> after electrochemical reduction. Figure 3.10(b) shows smooth nanotubes which are closely packed and aligned upon which minor non-nanotubular layers are deposited. These non-nanotubular layers developed during electrochemical reduction in DMF-TBAP solution.

Figure 3.11 shows unwashed samples of TiO<sub>2</sub> nanotubes after electrochemical reduction. Figure 3.11(a) shows ordered tubular structure with tubes openings which are similar to those in figures 3.8(a) and 3.9(a). The closely packed and aligned nanotubes were maintained (see figure 3.11(b)) after electrochemical reduction (in the cross sectional view). The right side edge (which was not uniform) was that of a top view which was not attached to Ti substrate. Thus, the morphology of TiO<sub>2</sub> nanotubes was not altered by electrochemical reduction in ACN-TBAP solution.

All reduced samples were washed prior to TEM characterization. The reduced TiO<sub>2</sub> nanotubes samples also have an average inner diameter of 98 nm and wall thickness of 21 nm. The reduced TiO<sub>2</sub> nanotubes (in figure 3.12) have the dark appearance similar to amorphous TiO<sub>2</sub> nanotubes in figure 3.4.

Figure 3.14 shows higher resolution TEM of reduced and annealed TiO<sub>2</sub> nanotubes (sample 3) in figure 3.13. It is clear from HR-TEM image that only slight coloration still remains. Moreover, “hair like layers” on the surface of the nanotubes can be seen. It is not clear at this point what might be their due and more investigation needs to be done to clarify this matter. TEM results of reduced TiO<sub>2</sub> nanotubes in ACN-TBAP or DMF-TBAP have not been published before.

### **3.1.2.1 Effect of electrolyte composition in reduction process.**

TBAP was used as supporting electrolyte for all electrochemical reduction processes, and it was used to prevent intercalation process which could have been the case if lithium perchlorate was used as described in section 3.3.1. The colour of TiO<sub>2</sub> nanotubes changes from yellowish white to dark-blue when TiO<sub>2</sub> nanotubes were electrochemically reduced (see figure 3.15). The blue TiO<sub>2</sub> nanotubes colour was not obtained when using DMF or ACN alone during electrochemical reduction process.

Only when a certain amount of supporting electrolyte (100 mM) was added to organic solvents under certain electrochemical conditions (electrode separation was 4 cm, applied voltage 3 V for 4 minutes) then a permanent dark-blue colour of TiO<sub>2</sub> nanotubes was formed, as shown in figure 3.15(b). However, the blue colour was not observed instantly but developed during the electrochemical reduction process. It was very difficult to observe diminutive colour changes over a short period of time (several seconds). It was also noticed that an increase of colour intensity occurred over a longer period (4 minutes) of reduction process.

The blue colour was attributed to the reduction of titanium dioxide [201] since  $\text{TiO}_2$  has been long known to exhibit a deep blue coloration upon reduction.

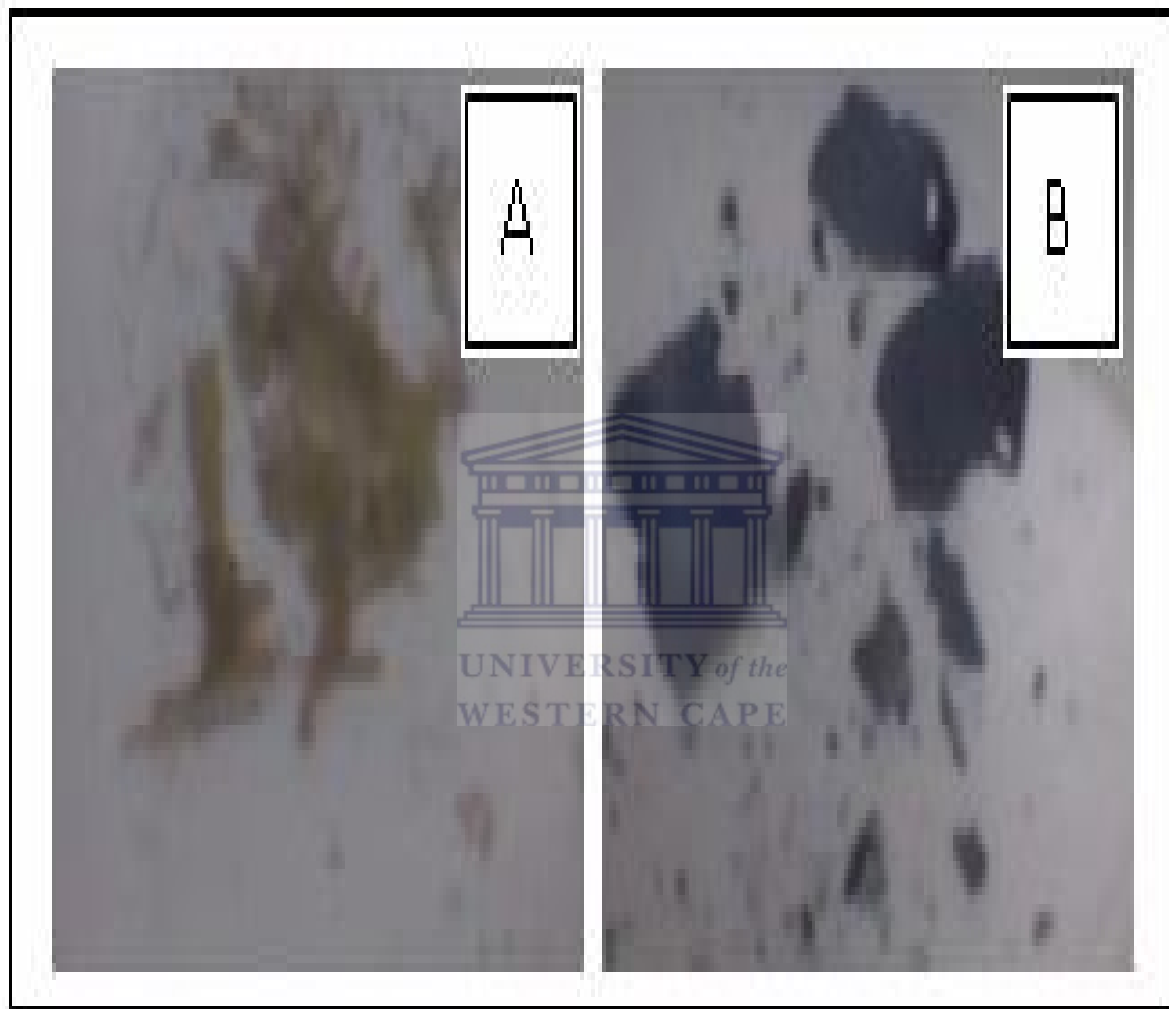


**Figure 3.15** Illustrative (A) yellowish white and (B) dark blue colour of as-grown  $\text{TiO}_2$  nanotubes before and after electrochemical reduction in 0.2M ACN-TBAP, respectively.

## 3.2 XRD measurements.

*Table 3.3 Different treatments of TiO<sub>2</sub> nanotube and Degussa P25 (sample j) for XRD.*

Samples	Treatments of TiO <sub>2</sub> nanotubes
a	As anodized.
b	As anodized → annealed under N <sub>2</sub> at 280°C.
c	As anodized → annealed under N <sub>2</sub> at 380°C.
d	As anodized → annealed under N <sub>2</sub> at 480°C.
e	As anodized → photoreduced in MeOH.
f	As anodized → photoreduced in MeOH → annealed under N <sub>2</sub> at 280°C.
g	As anodized → annealed under N <sub>2</sub> at 280°C → photoreduced in MeOH.
h	As anodized → Electrochemical reduced in DMF -(0.1M)TBAP → annealed under N <sub>2</sub> at 280°C.
i	As anodized → Electrochemical reduced in ACN -(0.1M)TBAP → annealed under N <sub>2</sub> at 280°C.
j	Degussa P25

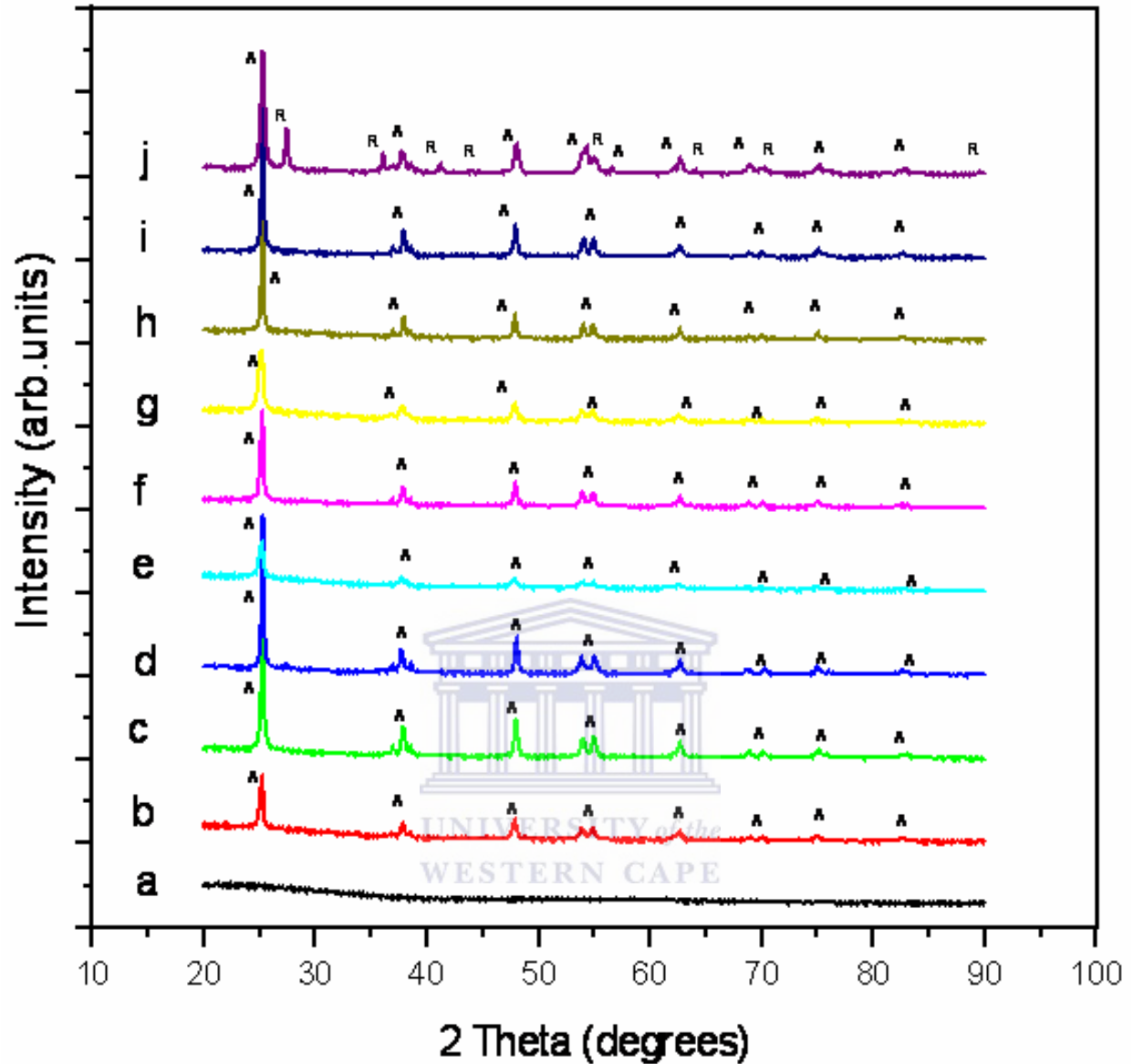


*Figure 3.16 X-ray diffraction peaks of the TiO<sub>2</sub> nanotubes arrays samples treated by various electrochemical and photochemical conditions. Sample j is a commercial Degussa P25 (80% anatase and 20% rutile) form. A and R represents anatase and rutile, respectively.*

XRD confirms that the as-grown  $\text{TiO}_2$  nanotubes made by anodization is amorphous, as shown in figure 3.13(a) whereas the commercial Degussa P25 contains a mixture of rutile and anatase, as shown in figure 3.13 (j)

Figure 3.13 (b, c and d) shows the XRD of  $\text{TiO}_2$  nanotubes after annealing in dry nitrogen for 3 hours at 280°C, 380°C and 480°C, respectively. The increase of temperature from 280°C to 480°C results in an increase in crystallinity, and diffraction peaks indicate that the samples are in the anatase form. However there is a slight indication that at 480°C rutile has been formed.

Figure 3.13 (e) shows XRD patterns of  $\text{TiO}_2$  nanotubes that were reduced photochemically for 1 hour. This treatment has converted some of the amorphous material to the anatase crystalline form, possibly due to the refluxing temperature and/or irradiation with UV light. Figure 3.13 (f) shows an increase of crystallinity due to annealing. Photochemical treatment after calcination does not alter the diffraction peaks intensity significantly, as shown in figure 3.13 (g).

It can be seen that after various electrochemical and photochemical treatments, followed by thermal treatments, the  $\text{TiO}_2$  nanotubes were crystallized and all of the diffraction peaks exhibit a phase transition from amorphous to anatase at temperatures above 280°C. There are no diffraction peaks corresponding to other crystals such as brookite, rutile and TiN in  $\text{TiO}_2$  nanotubes. This indicated that N doping did not change the crystal structure of  $\text{TiO}_2$ .

## 3.3 Cyclic voltammetry (CV) studies.

### 3.3.1 CV in non aqueous solution.

Acetonitrile and DMF have a high dielectric constant and a very wide useful potential window. The accessible potential window in ACN containing TBAP is 6 V between -3.5 V and 2.5 V [202]. Thus, the cyclic voltammetry results were not affected by the breakdown potential of electrolyte solution since acetonitrile does not oxidize or reduce within the potential window used.

No intercalation occurs because the tetrabutylammonium cation is very large in comparison with simple inorganic cations, such as  $\text{Li}^+$  [203] and cannot enter the solid body lattice. The amorphous  $\text{TiO}_2$  nanotube samples were used in the cyclic voltammetry studies. There was no dissolution of  $\text{TiO}_2$  nanotubes in the electrolyte even after prolonged cycling since it was not soluble in either aqueous or non-aqueous solvents which were used.

In all cyclic voltammetry experiments the applied potential was swept reductively and repetitive scanning did not change the voltammogram. Colour changes were also observed on the titanium rod electrode ( $\text{Ti}/\text{TiO}_2$ ) when  $\text{TiO}_2$  nanotubes were reduced electrochemically in DMF or ACN containing TBAP. The colour of  $\text{TiO}_2$  nanotubes changes from yellowish white to dark-blue (after several scans) during experiment when using the electrochemical system shown in figure 2.3.

The evaporation of the TBAP-ACN solution was a great problem over prolonged duration of experimentation. The rate of evaporation was increased by purging the solution with nitrogen and complicated the attempts to obtain consistent voltammograms. Many attempts were employed to minimize the issue of evaporation and finally steady voltammograms were obtained by cooling the surroundings of the electrolytic cell. When the electrolytic cell was used at room temperature, it should be noted that Ti/TiO<sub>2</sub> electrode possessed a large cathodic currents (at around -1.77 V) with a small anodic currents, but no redox peaks were observed, which can be ascribed to minimal electrical conductivity or suppressed of electron flow, as shown in figure 3.17 (a). This behaviour was caused by evaporation. However, when electrolytic cell was operated in an ice bath environment, two anodic and cathodic peaks at -2.116 V, -0.028 V and -0.351 V, -1.722 V, respectively were observed as shown in figure 3.17(b).

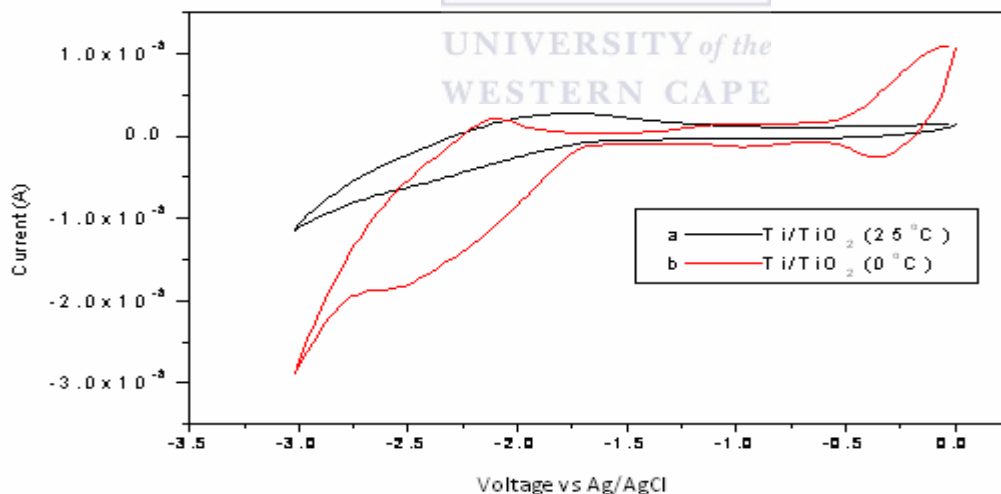


**Figure 3.17** Cyclic Voltammograms of *Ti/TiO<sub>2</sub> nanotubes* electrode surface in 0.2 M TBAP-ACN and sweep rate was 100 mV/s under nitrogen atmosphere through potential window of [0 ~ (-)3 V], (a) Electrolyte cell/system at room temperature, (b) Electrolyte cell/system was placed in an ice bath.

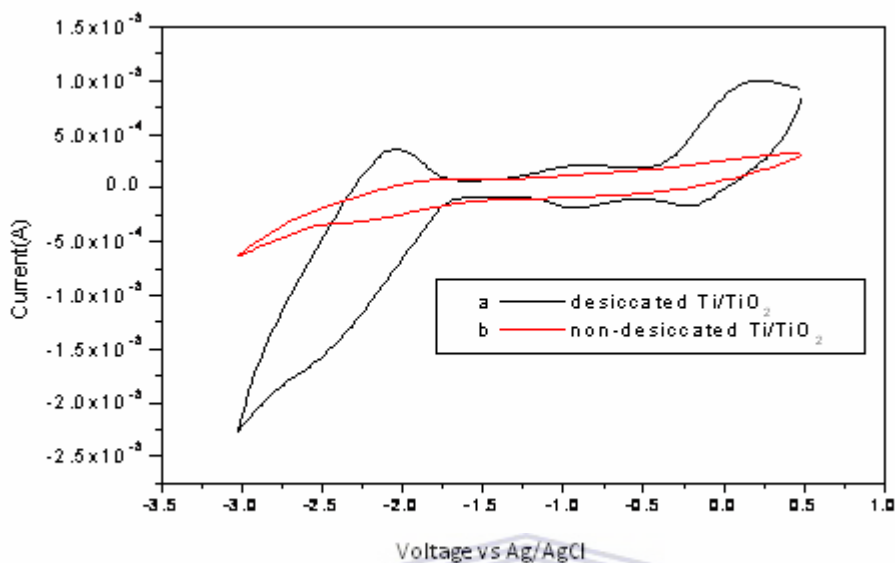


**Figure 3.18** Cyclic Voltammograms of  $Ti/TiO_2$  nanotube electrode surface in 0.2 M TBAP-ACN and sweep rate was 100 mV/s under nitrogen atmosphere through potential window of [0.5 ~(-3) V], Electrolyte cell/system was placed in an ice bath, desiccated sample (a) and non-desiccated sample (b).

In figure 3.18 illustrates the effect of desiccation on the  $Ti/TiO_2$  nanotubes samples. After anodization the samples were washed and dried in air for several minutes in room temperature. Subsequently, sample (a) was put in desiccator connected to vacuum for several hours while sample (b) was put in non-desiccated container to prevent dust and other contamination.

It is proposed that the contamination or defects on surfaces sites of the  $TiO_2$  nanotubes (non-desiccated sample) can be attributed to possible adsorbed moisture, and/or residual organic compounds formed during anodization and cleaning treatments. These caused electrons in the

nanotubes to encounter many grain boundaries, defects, and trap sites, becoming a factor that retards the electron transport time which suppresses electron flow to the electrolyte [204]. The result leads to a perturbed voltammogram showing no redox peaks.

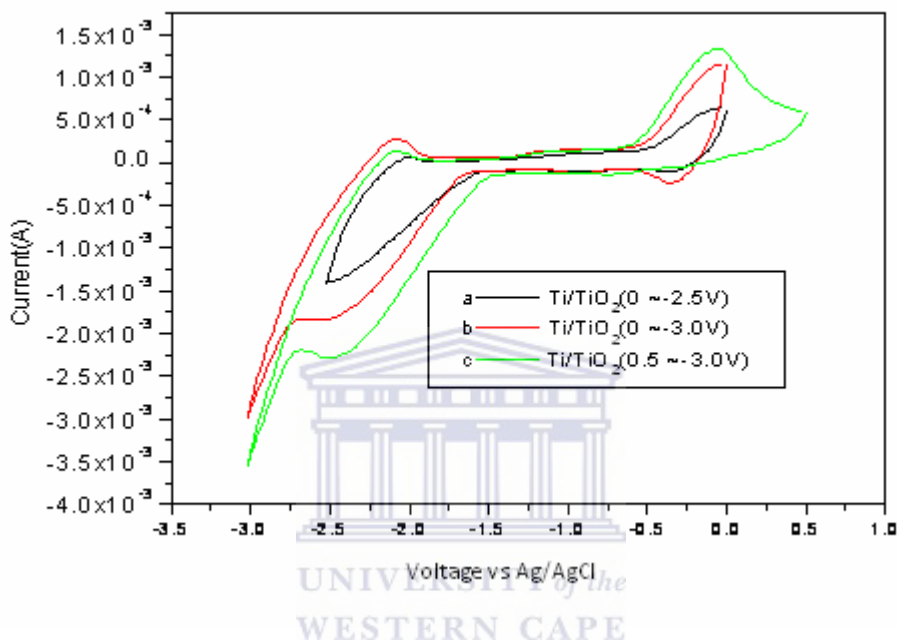


**Figure 3.19** Cyclic voltammograms of Ti/TiO<sub>2</sub> nanotubes electrode surface in 0.2 M TBAP-ACN and sweep rate was 100 mV/s under nitrogen atmosphere, Electrolyte cell/system was placed in an ice bath and all samples were desiccated, through various potential window (a)[0 ~ (-)2.5 V], (b)[0 ~ (-)3.0 V] and (c)[0.5 ~ (-)3.0 V].

In figure 3.19, the complete voltammogram is shown within a potential window of (0.5 ~ -3 V) and shows the occurrence of redox waves which comprised two anodic peaks and two cathodic peak at about (-2.1 V, 0.2 V) and (-2.5 V, -0.2 V), respectively.

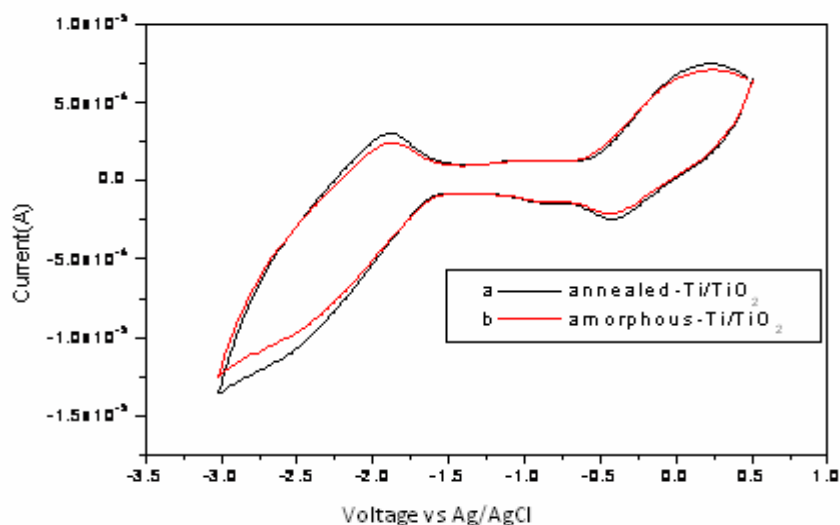


**Figure 3.20** Cyclic Voltammograms of  $\text{Ti/TiO}_2$  nanotube electrode surface in 0.2 M TBAP-ACN and sweep rate was 100 mV/s under nitrogen atmosphere through potential window of [0.5 ~(-3) V], Electrolyte cell/system was placed in an ice bath and samples were dessicated, (a) annealed sample at 280°C in nitrogen atmosphere and (b) amorphous sample .

There is no much difference between the cyclic voltammograms of annealed  $\text{Ti/TiO}_2$  and those of the amorphous as anodized sample in the case of non-aqueous solution, as shown in figure 3.20.

There were no observable peaks for bare Ti in the regions of significant peaks for  $\text{Ti/TiO}_2$  as shown in figure 3.21. This implies that the Ti metal does not undergo redox changes which can interfere with those of  $\text{Ti/TiO}_2$ .

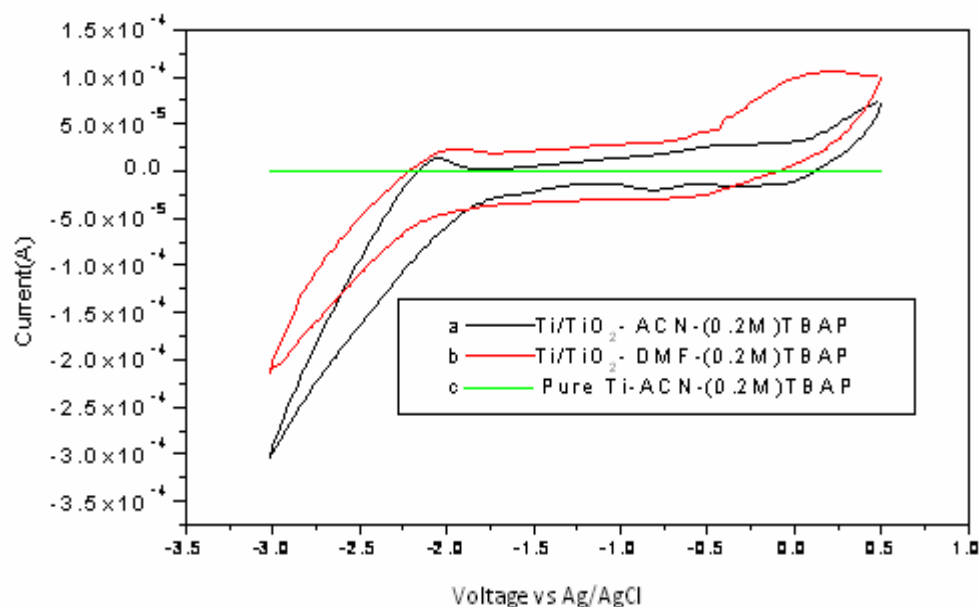


**Figure 3.21** Cyclic Voltammograms of (a ,b) titanium dioxide nanotubes ( $Ti/TiO_2$ ) and (c) titanium (Ti) in 0.2 M TBAP-DMF or ACN and sweep rate 100 mV/s under nitrogen atmosphere through potential window of [ 0.5~ (-)3 V]. Electrolyte cell/system was placed in an ice bath and samples were desiccated.

In figure 3.21(b), TBAP-DMF solution induces a shift to a more negative potentials (-1.7 V vs Ag/AgCl) as compared to TBAP-ACN solution (see figure 3.21(a)) at the starting point of the cathodic current. This shows that the TBAP-DMF solution plays a role in forming a barrier layer which inhibits movement of electron transfer, suppresses electron flow to the electrolyte and slow charge transfer [201]. Changing the electrolyte from MeCN to DMF does not significantly alter cyclic voltammogram behavior, as shown in figure 3.21.

The cathodic current follows similar increasing behavior in all cases of Ti/TiO<sub>2</sub> as shown in figure 3.22. A clear anodic peak is observed (at around -2.2 V) during anodic sweep and the corresponding cathodic peak is seen (figure 3.22) at the more negative potential of approximately -2.5 V. The peak currents for the redox change are different in the oxidation state of titanium at the surface and it may be due to difference in diffusion coefficients.

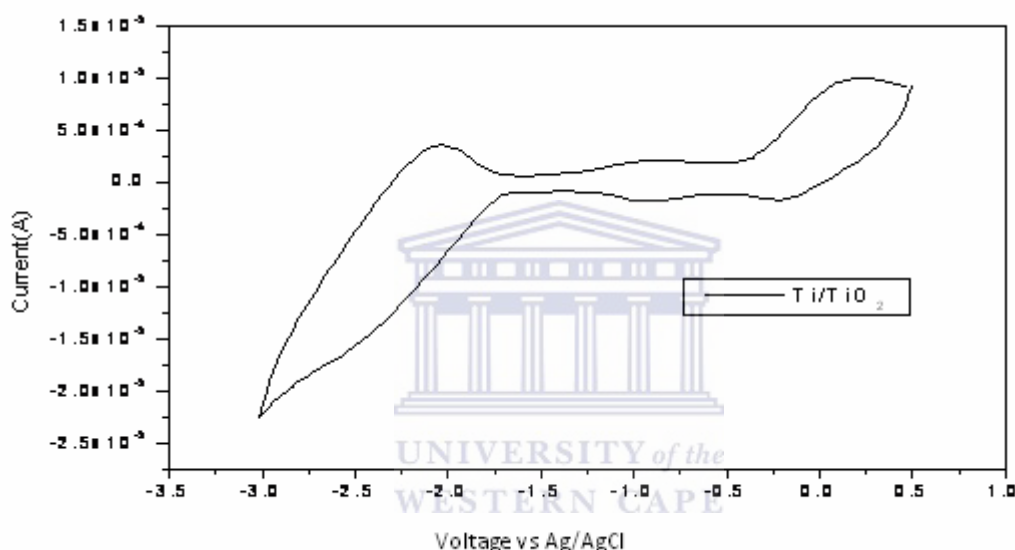


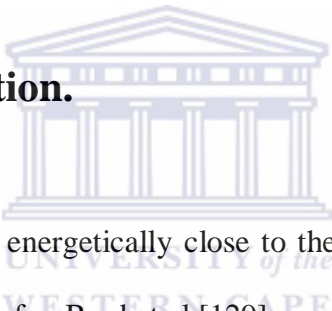
**Figure 3.22** Cyclic Voltammograms of Ti/TiO<sub>2</sub> nanotubes electrode surface in 0.2 M TBAP-ACN and sweep rate 100 mV/s under nitrogen atmosphere through potential window of [0.5 ~ (-)3 V], Electrolyte cell/system was placed in an ice bath.

TiO<sub>2</sub> nanotubes on a titanium electrode begin to reduce (at around -1.7 V) via electron accumulation as shown in figure 3.21 (a, b). This phenomenon results in blue colour which has been ascribed to electron accumulation within TiO<sub>2</sub> accompanied by ionic charge compensation and the presence of Ti<sup>3+</sup> balanced by an increase in the concentration of oxygen vacancies [205].

This suggests that the reduction peak is accompanied by an increase of oxygen vacancies. The blue colour that forms on the surface of the TiO<sub>2</sub> nanotubes was permanent even after the reduced TiO<sub>2</sub> nanotubes were exposed to air for a several days. The other minor redox peaks obtained (in the region between -0.5 V and -1.5 V, see figure 3.22) are believed to result from redox changes of organic contaminants in the solution.

Figure 3.22 shows two anodic peaks and two cathodic peaks at about (- 2.1 V, 0.2 V) and (- 2.5 V, - 0.2 V), respectively. This may due to oxidation and reduction of TiO<sub>2</sub> nanotubes. It may be possible that the reduction process occurred with two steps, from Ti<sup>4+</sup> to Ti<sup>2+</sup> via Ti<sup>3+</sup>.

### 3.3.2 CV in aqueous solution.



Only the redox couples, which are energetically close to the valence band or conduction band, are expected to undergo charge transfer. Bard et al [129] recorded CVs with a single-crystal TiO<sub>2</sub> electrode with redox couples chosen such that their redox potentials accommodate the entire potential window from the valence band to the conduction band. The idea was to determine the position of energy bands based on the reversibility of the CV for redox couples of known potentials, see figure 3.23.

Based on these results, three potential regions were identified: (i) a region positive to approximately -0.8 V, platinum is reversible but in the same potential range TiO<sub>2</sub> becomes totally irreversible. In some cases, the reduction wave for TiO<sub>2</sub> was shifted 1 V more negative compared

with that recorded on platinum. (ii) In the second potential region, negative to approximately -0.8 V, all redox couples of TiO<sub>2</sub> were reversible similar to that recorded on the platinum electrode.

(iii) In the third potential region, redox couples that reduce at potentials more positive than 0.4 V on platinum are reduced between +0.3 V and +0.4 V at TiO<sub>2</sub> irrespectively of their reduction potentials on platinum [125].

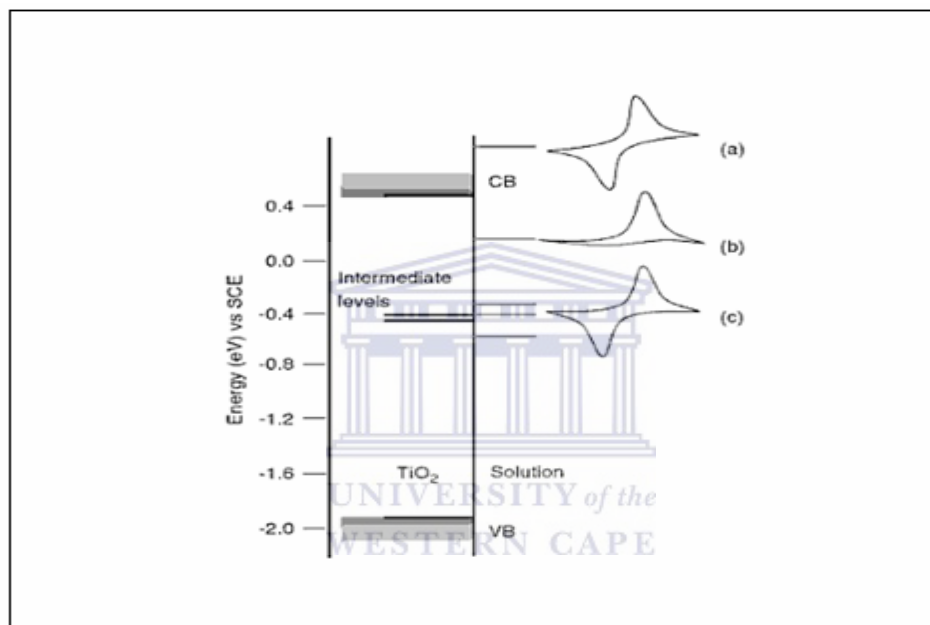


**Figure 3.23** Shows the band diagram for n-type single-crystal TiO<sub>2</sub> electrode based on CV measurements.(a) CV recorded for redox having redox potential above conduction band, reversibility of CV indicates metallic behavior of the electrode.(b) CV recorded for a redox having redox potential below conduction band, irreversibility of CV indicates rectifying nature of the junction.(c) Same CV for redox couples having redox potentials negative to ca. -0.3V indicating electron transfer through the surface states in this potential region [125].

The redox reaction observed in the first potential region between approximately -0.8 V and +0.3 V is attributed to electron transfer through a rectifying junction; this explains the irreversibility

of the CV curve. This behavior indicates that the redox potentials of the chosen redox couples are within the band gap region. The behaviour of the CV that is more negative than -0.8V can be attributed to the formation of an accumulation layer and metallic behaviour of the semiconductor. This behaviour indicates that the redox potential is above the conduction band. The CV behavior in the third potential region positive of +0.4 V is attributed to the mediation of electron transfer through surface states. Based on these results, the suggested band diagram for TiO<sub>2</sub> electrode was depicted as in figure 3.23.

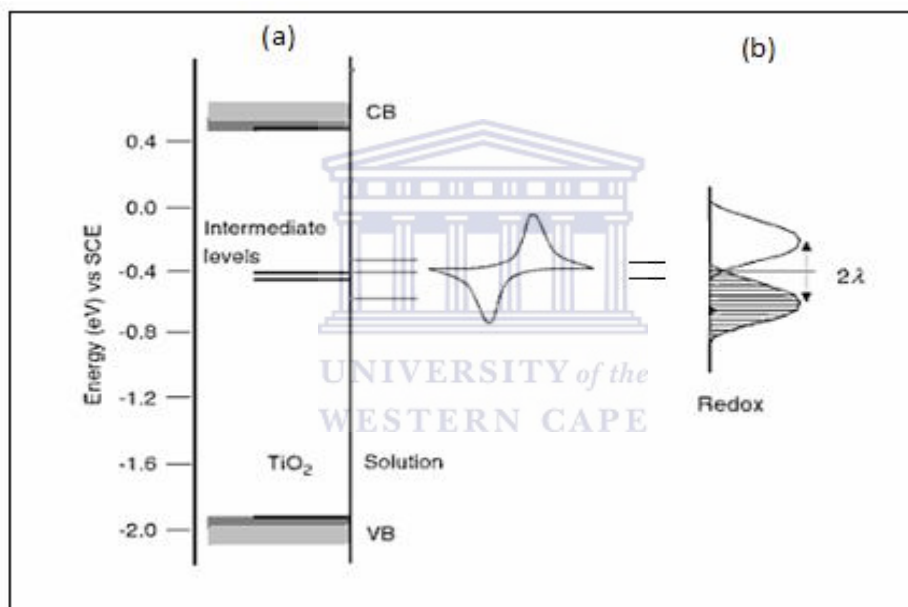


**Figure 3.24** Shows (a) the band diagram for n-type single-crystal TiO<sub>2</sub> electrode based on CV for redox couples having redox potentials, and (b) its equivalent energy diagram vs density of states for semiconductor –electrolyte interface (SEI) [125].

Figure 3.24 (b) shows energy diagram that results in an intermediate level within the band gap region. This region is where surface states at the semiconductor electrolyte interface facilitate reversible redox couples which are similar to that of metallic behaviour of electrode such as

platinum. Possible ways to induce intermediate levels in the semiconductor are doping, as discussed in section 1.2 b (i) and increased crystallinity [185, 206] or a combination of both [84-88, 207].

Crystallinity and resistivity in TiO<sub>2</sub> are inversely related. Annealing under a reductive environment, such as in nitrogen, can result in reduction of some of the Ti<sup>4+</sup> cations to lower valence state. At the same time, defects, such as the oxygen vacancies, can be generated in the TiO<sub>2</sub> structure due to a partial oxygen loss [206]. P. Xiao et al reported that the TiO<sub>2</sub> nanotubes annealed in nitrogen possesses lower resistivity than that calcined in air and argon [207].

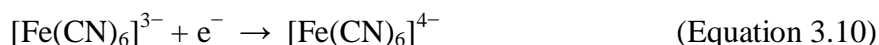
Annealing TiO<sub>2</sub> nanotubes at higher temperatures such as 650°C, resulted in the formation of rutile phase [207]. This phenomenon results in decreased conductivity which in turn was reflected by an increased separation of the anodic and cathodic peaks of the CV of the added redox couple. Moreover, the larger peak separations of redox couples are due to the lower electrical conductivity of the TiO<sub>2</sub> nanotube electrodes [207]. Calcination in different gases leading to possible doping is considered to be one viable approach to narrow the band gap and enhance the electrical conductivity [84-88].

The [Fe(CN)<sub>6</sub>]<sup>4-/3-</sup> redox system (with an exhibition of heterogeneous one-electron transfer ( $n = 1$ )) is one of the most extensively studied redox couples in electrochemistry [208]. The cyclic voltammetry experiments of the Fe<sup>2+/3+</sup> redox couple were performed by placing Ti/TiO<sub>2</sub> in an electrolyte solution of 10 mM K<sub>3</sub>[Fe(CN)<sub>6</sub>] and 1 M KCl. The electrochemical properties of TiO<sub>2</sub>

nanotubes electrodes annealed under different conditions were investigated by means of cyclic voltammetry in a potential range of  $-0.5$  V to  $1.2$  V versus Ag/AgCl at a sweep rate of  $0.1$  V/s.

In potassium ferricyanide  $K_3[Fe(CN)_6]$ , the possible redox changes are as follows:

Reduction of  $Fe^{3+}$



Oxidation of  $Fe^{2+}$

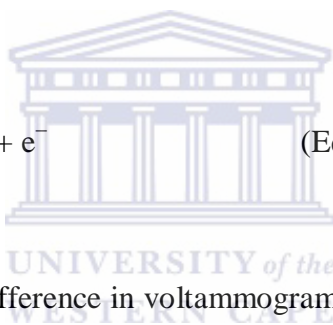
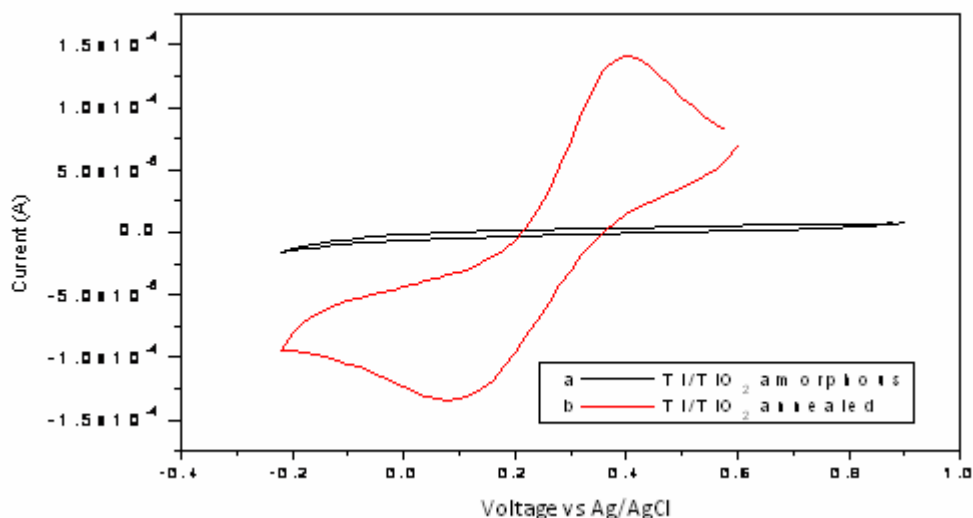
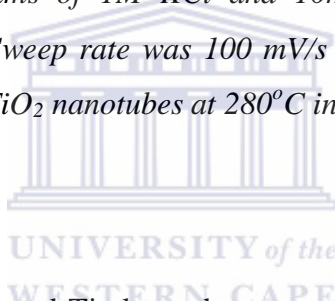


Figure 3.25 shows the enormous difference in voltammograms between amorphous and annealed  $TiO_2$  nanotubes in potassium ferricyanide solution. The iron (II/III) redox couple did not exhibit any observable peaks for as anodized  $Ti/TiO_2$  electrodes which contains amorphous  $TiO_2$ .  $Ti/TiO_2$  which was annealed at  $280^\circ C$  possesses a pair of well-defined oxidation/reduction peaks centered at  $0.402$  V and  $0.096$  V, with redox peak separation of approximately  $0.306$  V. The  $[Fe(CN)_6]^{4-}/[Fe(CN)_6]^{3-}$  redox couple occurs within the band gap of the  $TiO_2$  [125].

The amorphous  $TiO_2$  is so non conductive that the CV of  $[Fe(CN)_6]^{4-}/[Fe(CN)_6]^{3-}$  is not observed but when annealed surface states result in intermediate levels within  $TiO_2$  band gap which facilitate conductivity which results in a reversible CV.



**Figure 3.25** Cyclic Voltammograms of 1M KCl and 10mM  $K_3[Fe(CN)_6]$  using Ti/TiO<sub>2</sub> nanotubes as working electrode. Sweep rate was 100 mV/s of (a) amorphous TiO<sub>2</sub> nanotubes [0.9 ~ (-)0.2 V] and (b) annealed TiO<sub>2</sub> nanotubes at 280°C in nitrogen atmosphere [0.6 ~ (-) 0.2 V].



The titanium dioxide nanotubes coated Ti electrodes were annealed at 280°C in a tube furnace for 3 hours in different gaseous environment and then studied by cyclic voltammetry. The results in nitrogen show oxidation and reduction peaks at 0.393 V and 0.099 V, respectively, with redox peak separation of approximately 0.302 V. While electrodes annealed in argon and air have oxidation peaks at 0.676 V and 0.520 V, and reduction peaks at -0.257 V and - 0.098 V, respectively. Their redox peak separation was approximately 0.933 V and 0.618 V.

The redox peak separation in air is smaller than that compared to that in argon. Air contains nitrogen which in turn results in increased conductivity of the TiO<sub>2</sub> nanotubes semiconductor when used in the annealing environment. This verifies that TiO<sub>2</sub> nanotubes annealed at 280°C in

nitrogen streams has higher electrical conductivity than other gases mentioned above, as shown in figure 3.26.

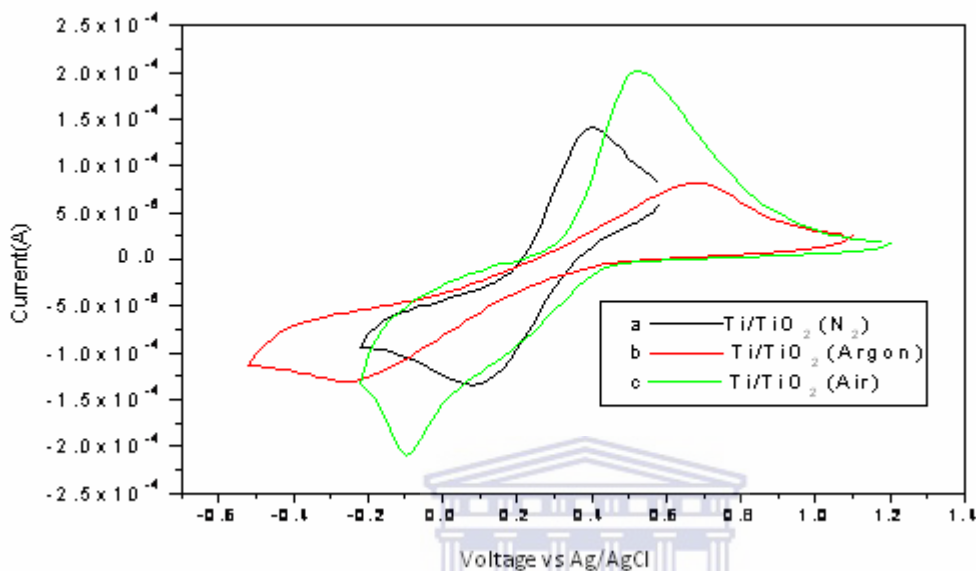


**Figure 3.26** Cyclic Voltammograms of 1 M KCl and 10 mM  $\text{K}_3[\text{Fe}(\text{CN})_6]$  using  $\text{Ti/TiO}_2$  nanotubes electrode as working electrode.  $\text{Ti/TiO}_2$  nanotubes electrode were annealed in various gases. Sweep rate 100 mV/s through various potential window of (a) [0.6 ~ -0.2 V], nitrogen, (b) [1.1 ~ -0.5 V], argon and (c) [0.8 ~ -0.2 V], air.

The effect of temperature was investigated by varying the annealing temperature in the tube furnace under a stream of nitrogen gas. The electrochemical properties of the  $\text{TiO}_2$  nanotubes electrodes were monitored using CV, as shown in figure 2.3.

Electrode which was annealed at 280°C has oxidation and reduction peaks at 0.398 V and 0.094 V, respectively, with redox peak separation of approximately 0.304 V. While electrodes annealed at 380°C and 480°C have oxidation peaks at 0.939 V and 0.523 V, and reduction peaks at

-0.198 V and -0.099 V, respectively. Their redox peak separation was approximately 1.137 V and 0.622 V.

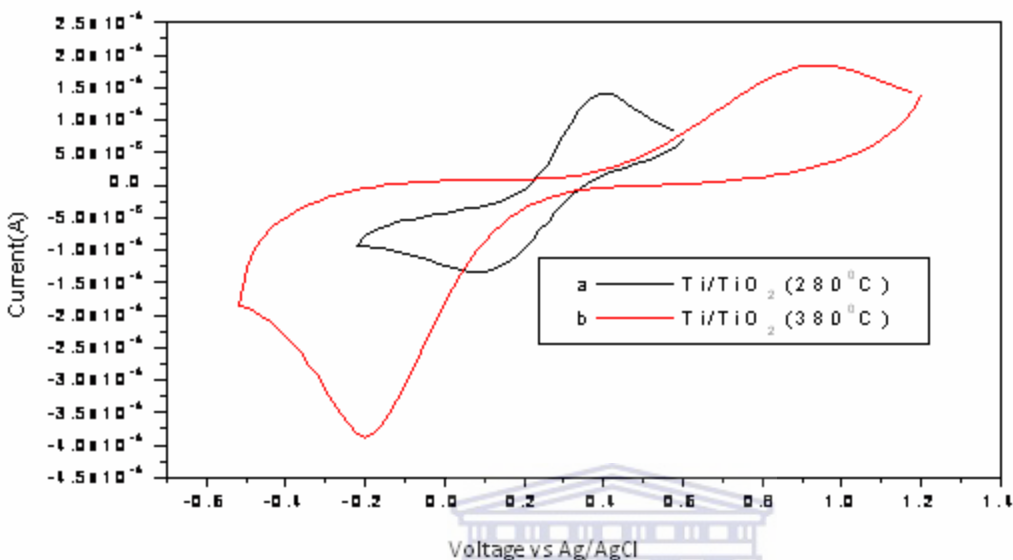


**Figure 3.27** Cyclic Voltammograms of 1 M KCl and 10 mM  $\text{K}_3[\text{Fe}(\text{CN})_6]$  using  $\text{Ti/TiO}_2$  nanotubes as working electrode annealed at various temperatures. Sweep rate was 100 mV/s under nitrogen atmosphere through various potential window of (a) [0.6 ~ -0.2 V] at 280°C and (b) [1.2 ~ -0.2 V] at 380°C.

This shows that titanium dioxide nanotubes annealed at 280°C has a higher electrical conductivity than the sample annealed at 380°C, see figure 3.27. The larger the peak separation the lower the electrical conductivity of the  $\text{TiO}_2$  nanotube electrodes [207]. This phenomenon is possibly due to occurred grain boundary effects reducing the conductivity. Moreover, similar results were observed by R. Asmatulu et al [185] when annealing  $\text{TiO}_2$  nanotube in air atmosphere above 350°C. For less conductive electrode, it is difficult for electroactive probe molecules to lose or gain electrons on the electrode surface than when conductive electrodes are used.

### 3.4 RBS Characterization.

Table 3.4 Different treatments of Ti/TiO<sub>2</sub> samples for RBS.

Samples	Treatments of TiO <sub>2</sub> nanotubes
R1	As anodized.
R2	As anodized → annealed under N <sub>2</sub> at 280°C.
R3	As anodized → annealed under O <sub>2</sub> at 280°C.
R4	As anodized → annealed under O <sub>2</sub> at 480°C.
R5	As anodized → photoreduced in MeOH.
R6	As anodized → photoreduced in MeOH → annealed under N <sub>2</sub> at 280°C.
R7	As anodized → annealed under N <sub>2</sub> at 280°C → photoreduced in MeOH.
R8	As anodized → Electrochemical reduced in DMF -(0.1M)TBAP → annealed under N <sub>2</sub> at 280°C.
R9	As anodized → Electrochemical reduced in ACN -(0.1M)TBAP → annealed under N <sub>2</sub> at 280°C.

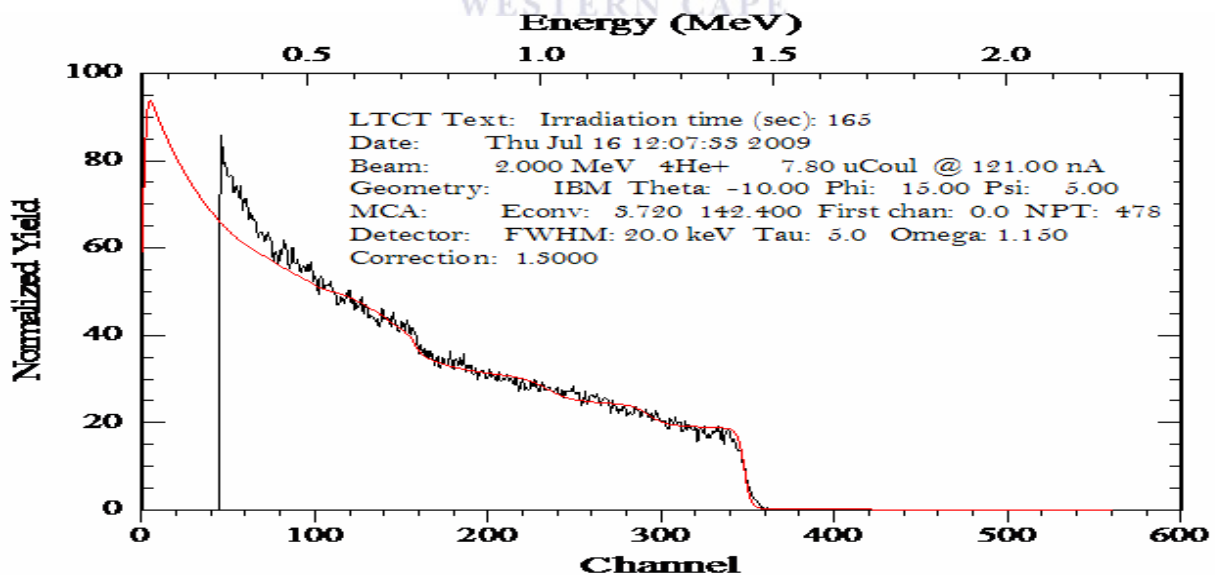


Figure 3.28 As-anodized TiO<sub>2</sub> nanotubes of sample (R1) shows experimental and the simulated spectra in black and red, respectively.

Spectra from the anodized R1, the anodized and N<sub>2</sub> annealed R2, R3 and R4, and the anodized, N<sub>2</sub> annealed and methanol photoreduced R7 were all practically identical, see figure 3.28 as an example for sample R1. The stoichiometry of the deposited layer is estimated by iterative simulation of the experimental spectrum using the RBS analysis program RUMP. From for these measurements, it is not possible to determine without any ambiguities the relative concentrations of oxygen, nitrogen and carbon in any of the samples. That is because of excessive overlapping of signals from these elements. In some instances excluding C or N from the simulation makes no difference. Similarly interchanging the simulated elemental concentrations of O and N has no visible effect on the simulated spectrum.

Spectra from the reduced and N<sub>2</sub> annealed samples R5, R6, R8 and R9 are identical with those of sample R1 to R4. Attempts at determining the concentrations of O, N, and C all bear inconclusive results. The RBS technique works best for analysis of heavy elements in a light element matrix, when there is little or no overlap of signals coming from different target elements. The only quantification that may be possible for some of these samples is that of the thickness of the deposited layer and Ti content in that layer. Analysis results of all samples are summarized in the table 3.8 of section 3.7.

The graphs in figure 3.28 show an example of both the experimental and the simulated spectra. The compositions of the layers of TiO<sub>2</sub> nanotubes are reliable for Ti metal (obtained by using RBS analysis program RUMP) and these were used in conjunction with elemental analysis data for C and N (obtained using an elemental analyzer not from RBS data).

### 3.5 UV/Vis Diffuse Reflectance spectroscopy (DRS)

#### Measurements.

Measurement of diffuse reflectance with a UV-visible spectrophotometer is a standard technique in the determination of the band gap of semiconductors such as TiO<sub>2</sub> [209].

*Table 3.5 shows different treatments for Ti/TiO<sub>2</sub> samples for UV/Vis Diffuse Reflectance Spectroscopy.*

Samples	Treatments of TiO <sub>2</sub> nanotubes
a	As anodized.
b	As anodized → annealed under N <sub>2</sub> at 280°C.
c	As anodized → annealed under Air at 280°C.
d	As anodized → photoreduced in MeOH.
e	As anodized → photoreduced in MeOH → annealed under N <sub>2</sub> at 280°C.
f	As anodized → annealed under N <sub>2</sub> at 280°C → photoreduced in MeOH.
g	As anodized → Electrochemical reduced in DMF -(0.1M)TBAP → annealed under N <sub>2</sub> at 280°C.
h	As anodized → Electrochemical reduced in ACN -(0.1M)TBAP → annealed under N <sub>2</sub> at 280°C.

The colours of the nanotubes vary according to the atmosphere used in calcination. In oxygen, nitrogen, argon and air they become white, dark grey to blue, grey blue and grey yellow in colour, respectively.

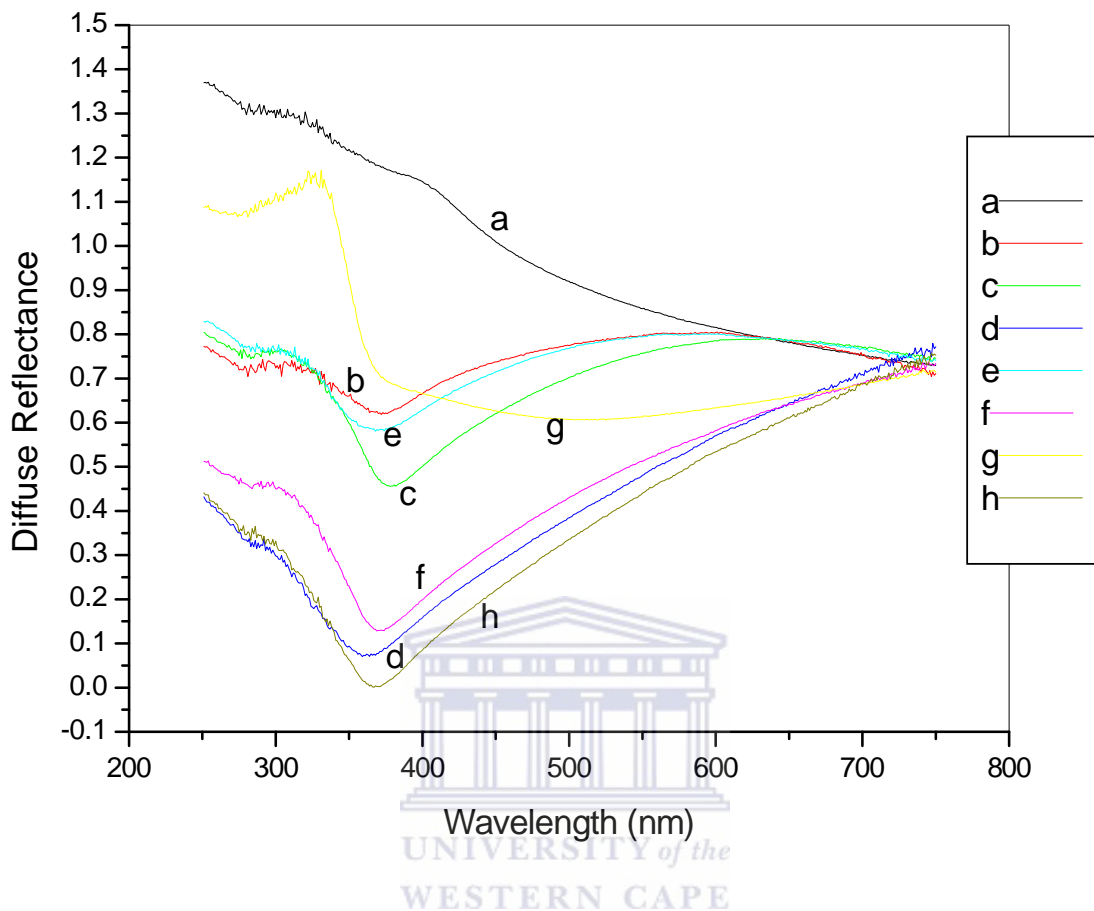


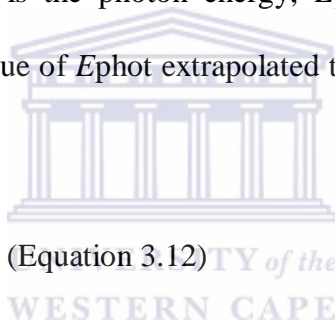
**Figure 3.29** UV/Vis Diffuse Reflectance spectroscopy showing spectrum results of titanium dioxide nanotubes film on titanium substrate.

Ti/TiO<sub>2</sub> nanotube samples were placed in the sample beam of the spectrometer while still in their layer structure on the titanium metal substrate with CaSO<sub>4</sub> in the reference beam. The UV/Vis DRS was calibrated by establishing the base-line with the reference material (CaSO<sub>4</sub>) in the sample beam. Figure 3.29 shows absorption spectra of TiO<sub>2</sub> nanotubes samples (treated in various conditions, as shown in table 3.5). It can be clearly seen that the absorption edges range between 350 nm and 400 nm. The absorption spectra vary from each other due to different treatment employed.

The occurrence of this absorption is known to be caused by the presence of structural defects that possess energy state within the band gap. Other absorption edges shifted to the lower energy, towards visible-light region.

In order to determine accurate band gaps of TiO<sub>2</sub> nanotubes samples, the data from UV/vis DRS were used in an Equation 3.12, see figure 3.30 as an example (for sample h in figure 3.29). The results of band gaps for TiO<sub>2</sub> nanotubes samples are summarized in the table 3.6.

Figures (4.28) show the  $(\alpha h\nu)^{1/2}$  versus  $E_{\text{phot}}$  plot for an indirect transition, where  $\alpha$  is the absorption coefficient and  $E_{\text{phot}}$  is the photon energy,  $E_{\text{phot}} = (1239/\lambda)$  eV, and  $\lambda$  is the wavelength in nanometers. The value of  $E_{\text{phot}}$  extrapolated to  $\alpha = 0$  gives an absorption energy, which corresponds to the band gap.



$$\alpha h\nu = C (h\nu - E_g)^n$$

(Equation 3.12)

Where C is a constant. For indirect band gap  $n = 2$  and for direct band gap  $n = 1.5$ . Note that some authors exclude the  $h\nu$  factor on the left-hand side in (equation 3.12), this has only a minor influence on the value of  $E_g$  obtained [210-211].

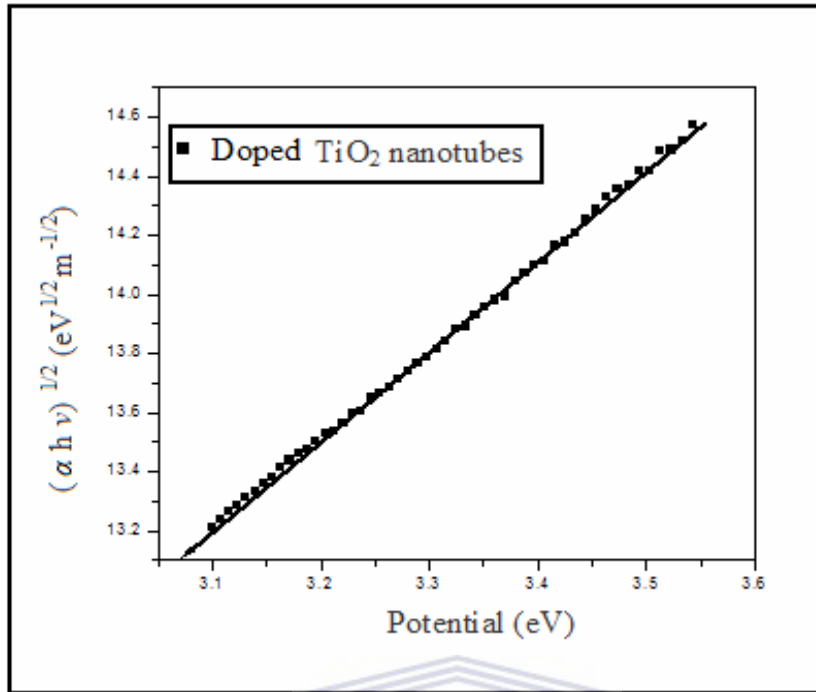
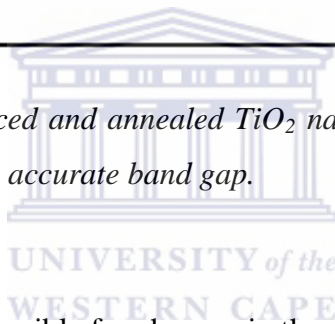


**Figure 3.30** Tauc plots of reduced and annealed  $\text{TiO}_2$  nanotubes (sample(h) in figure 3.27), showing possible fits to obtain the accurate band gap.



The structural modification is responsible for changes in the shape of the fundamental absorption edge. The result shows a narrowed band gap which is below 3.1 eV for doped  $\text{TiO}_2$  nanotubes, as shown in figure 3.30.

**Table 3.6** Shows band gaps results of Ti/TiO<sub>2</sub> samples in figure 3.29.

Samples	Band Gaps of TiO <sub>2</sub> samples
a	3.14 eV
b	3.00 eV
c	2.98 eV
d	3.07 eV
e	3.01 eV
f	3.04 eV
g	2.95 eV
h	3.08 eV

The results show that an amorphous TiO<sub>2</sub> nanotube has a larger band gap of 3.14 eV compared to 3.00 eV of annealed TiO<sub>2</sub> nanotube in nitrogen atmosphere, as shown in table 3.6(a,b). Thus it appears annealing TiO<sub>2</sub> nanotubes sample in nitrogen atmosphere reduces the band gap.

However, it can be seen that TiO<sub>2</sub> nanotubes annealed in nitrogen atmosphere (with a band gap of 3.00 eV) have a higher band gap than those annealed in air atmosphere (with a band gap of 2.98 eV). This may be due to experimental error, see table 3.6(b, c). However, R.P. Vitiello et al. reported TiO<sub>2</sub> nanotubes annealed in air atmosphere with a band gap of 3.2 eV [84].

Sample that was reduced in DMF-TBAP solution and annealed in nitrogen atmosphere has the lowest band gap of 2.95 eV, see table 3.6(g). Published results on the band gaps have been found

to be 2.67–3.54 eV for different compositions in  $\text{TiO}_{2-x}\text{N}_x$  thin films [95]. The samples that were used in UV-DRS were not washed and thus more work is recommended to validate uncertainties of experimental errors.

### 3.6 XPS Measurements.

The nitrogen signals were all too small to show qualitative evidence for nitrogen doping. However, binding energies values of Ti 2p electrons indicate that dopant nitrogen locates at an oxygen site in  $\text{TiO}_2$  nanotubes [84]. This is illustrated by XPS spectra in figure 3.31 - 3.32.

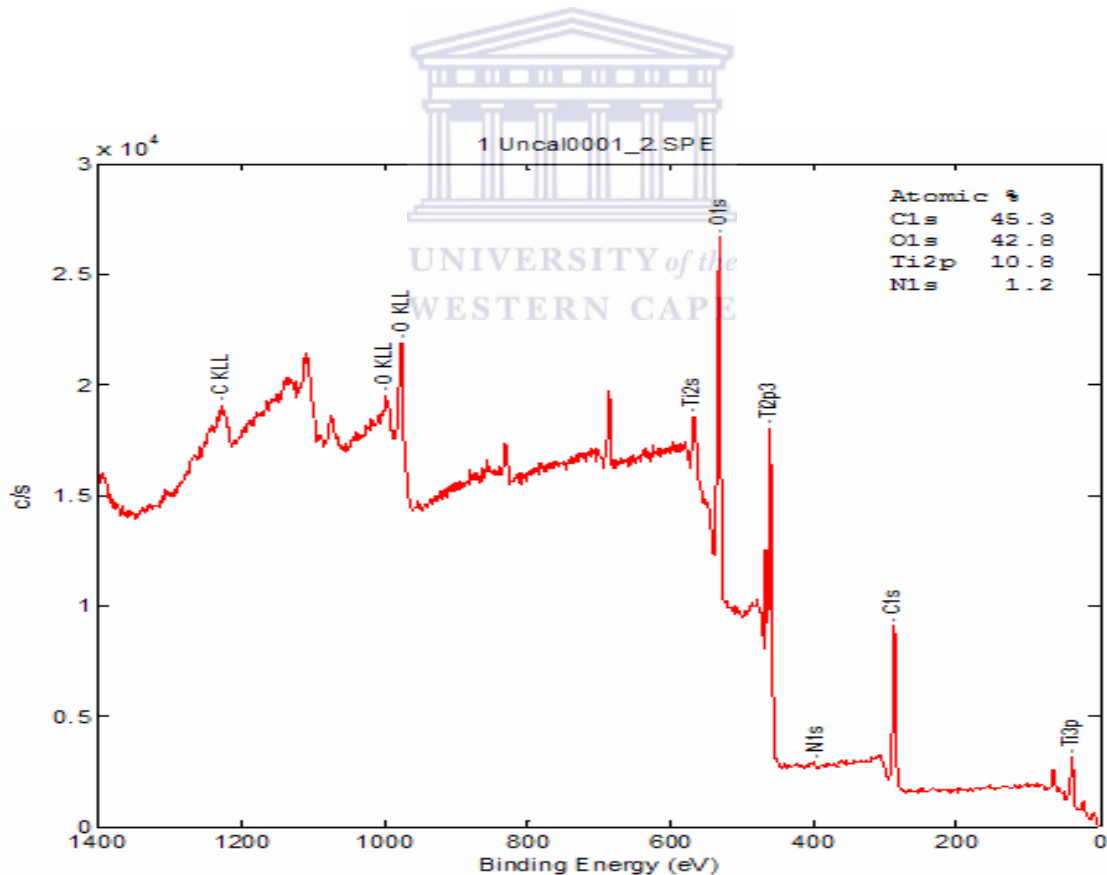


**Figure 3.31** XPS spectra of (reduced and annealed at 280°C in nitrogen)  $\text{TiO}_2$  nanotubes sample.

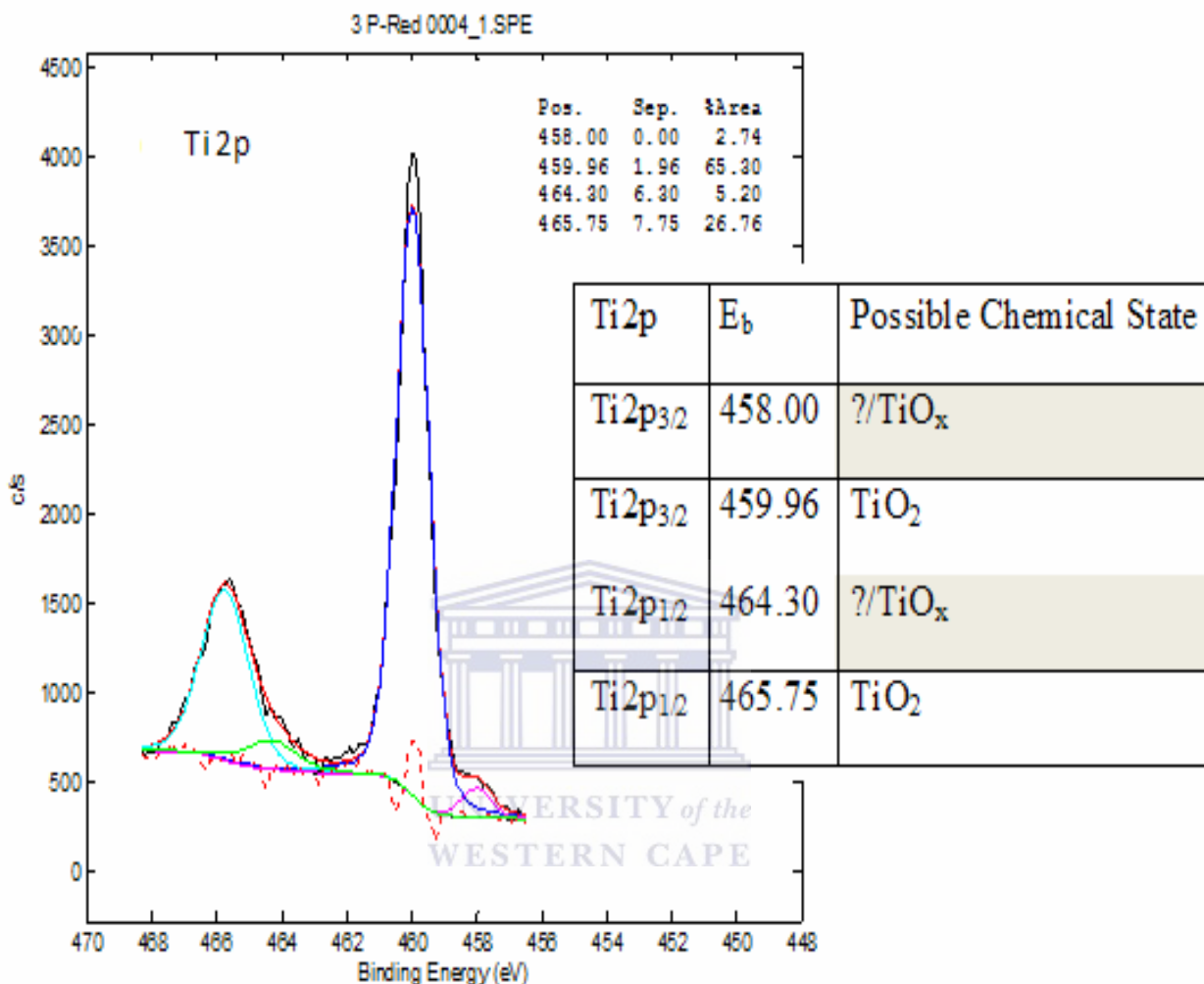


**Figure 3.32** XPS spectra of Ti 2p sample of (reduced and annealed at 280°C in nitrogen) TiO<sub>2</sub> nanotube.

Figures 4.31 and 4.32 show the TiO<sub>2</sub> nanotubes sample that was reduced in ACN-TBAP solution and annealed at 280°C in nitrogen atmosphere was used for XPS analysis.

The binding energies of Ti 2p<sub>3/2</sub> and Ti 2p<sub>1/2</sub> are observed to be at 458.00 and 464.30 eV, which can be assigned to Ti<sup>4+</sup> (TiO<sub>2</sub>), with a peak separation of 6.3 eV between these two peaks. It

should be noted that the Ti  $2p_{3/2}$  peak (458.00 eV), was notably lower than the standard data (459.96 eV) [212-213]. Such a shift toward lower binding energy indicates the successful incorporation of nitrogen and carbon into the  $TiO_2$  lattice. After doping (when the N atom replaces the O atom of the lattice), the valence state of the Ti cation may be reduced. Mixing of N(2p) states with O(2p) states results in a reduction of the band gap. It is known that the conduction and valence bands of  $TiO_2$  are attributed to the Ti 3d and O (2p) orbitals, respectively. Because the N(2p) orbital has higher potential energies than O (2p), the increase in nitrogen incorporation should result in the higher negative potential of the valence band compared to that of pure  $TiO_2$ , leading to a narrower band gap.

The binding energy of the Ti  $2p_{3/2}$  peak shifts to lower energies when the valence state of  $Ti^{4+}$  is reduced to  $Ti^{3+}$  and  $Ti^{2+}$ . Thus, the observed Ti  $2p_{3/2}$  binding energy after nitrogen treatment can be attributed to the formation of O—Ti—N bonding by partially substituting the oxygen atom in the  $TiO_2$  lattice with a nitrogen or carbon atom. A substantial portion of the doped nitrogen is not directly bound to Ti [99]. This shifts the binding energies of the Ti 2p electrons to the observed lower values [214-217]. XPS and elemental analyser results show that all  $TiO_2$  nanotubes consist of nitrogen atoms in  $TiO_2$  nanotube, see table 3.8.

### **3.7 Light element analysis.**

The elemental composition of carbon and nitrogen in  $TiO_2$  nanotubes was determined by use of an elemental analyser. The elemental analysis data for carbon and nitrogen was used with

conjunction with RBS data (for titanium). The empirical formula (shown in table 3.8) for the TiO<sub>2</sub> nanotubes samples was calculated.

*Table 3.7 shows different treatments for Ti/TiO<sub>2</sub> samples for elemental analyser (EA).*

samples	Treatments of TNTs
E1	As anodized.
E2	As anodized → annealed under N <sub>2</sub> at 280°C.
E3	As anodized → annealed under N <sub>2</sub> at 280°C → photoreduced in MeOH.
E4	As anodized → Electrochemical reduced in DMF -(0.1M)TBAP → annealed under N <sub>2</sub> at 280°C.
E5	As anodized → Electrochemical reduced in ACN -(0.1M)TBAP → annealed under N <sub>2</sub> at 280°C.
E6	As anodized → photoreduced in MeOH → annealed under N <sub>2</sub> at 280°C.
E7	As anodized → photoreduced in MeOH.
E8	As anodized → annealed under O <sub>2</sub> at 280°C
E9	As anodized → annealed under O <sub>2</sub> at 480°C

The TiO<sub>2</sub> nanotubes (which was treated by various condition, see table 3.7) were used to determine sub-stoichiometry. The elemental composition of light elements namely, nitrogen and carbon were obtained by using elemental analyser. Their concentrations in weight percentage are shown in table 3.8. The compositions Ti metal was obtained by using RBS analysis program RUMP and these were used in conjunction with elemental analysis data for carbon and nitrogen to determine sub-stoichiometry of TiO<sub>2</sub> nanotubes, as shown in table 3.8. The calculation for sub-stoichiometry of TiO<sub>2</sub> nanotubes is in section 2.9.2.

**Table 3.8** Shows elemental composition data of nitrogen and carbon of TiO<sub>2</sub> nanotubes samples (from elemental analyser) to calculate empirical formula.

Sample name	N wt.%	C wt.%	O wt.%	Ti wt.%	Elemental Composition of TiO <sub>2</sub> nanotubes
E1	0.18	4.31	36.86	58.65	TiO <sub>1.7</sub> N <sub>0.01</sub> C <sub>0.29</sub>
E2	0.57	2.57	37.94	58.92	TiO <sub>1.8</sub> N <sub>0.03</sub> C <sub>0.17</sub>
E3	0.34	3.75	36.93	58.98	TiO <sub>1.73</sub> N <sub>0.02</sub> C <sub>0.25</sub>
E4	0.97	4.33	35.50	59.20	TiO <sub>1.65</sub> N <sub>0.06</sub> C <sub>0.29</sub>
E5	1.55	4.63	34.49	59.33	TiO <sub>1.60</sub> N <sub>0.09</sub> C <sub>0.31</sub>
E6	0.90	4.38	35.32	59.40	TiO <sub>1.66</sub> N <sub>0.05</sub> C <sub>0.29</sub>
E7	0.41	4.33	38.68	59.58	TiO <sub>1.69</sub> N <sub>0.02</sub> C <sub>0.29</sub>
E8	0.02	0.78	39.40	59.80	TiO <sub>1.95</sub> N <sub>0.001</sub> C <sub>0.05</sub>
E9	0.004	0.66	39.40	59.94	TiO <sub>1.96</sub> N <sub>0.0002</sub> C <sub>0.04</sub>

The results in table 3.8 show that all TiO<sub>2</sub> nanotubes samples contained nitrogen and carbon. Amorphous TiO<sub>2</sub> nanotubes sample was annealed at 280°C in nitrogen atmosphere then the concentration of nitrogen increased by a factor of 3.2 wt% while carbon concentration decreased

by a factor of 1.7 wt%, see table 3.8(E1,E2). However, when amorphous TiO<sub>2</sub> nanotubes sample were annealed at 280°C in oxygen atmosphere both concentrations of nitrogen and carbon decreased by a factor of 9 wt% and 5.5 wt% , respectively (see table 3.8(E1,E8)). Furthermore, when the temperature was at 480°C in oxygen atmosphere for the same duration, both concentrations of nitrogen and carbon decreased by a factor of 45 wt% and 6.5 wt% , respectively (see table 3.8(E1,E9)). At this stage anatase TiO<sub>2</sub> nanotube was almost pure.

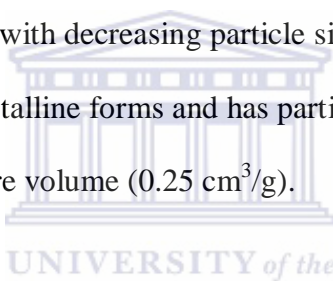
The TiO<sub>2</sub> nanotubes sample (E5) that was reduced electrochemically in ACN-TBAP solution and annealed at 280°C in nitrogen atmosphere has the highest amount of nitrogen and carbon than those in table 3.8. This sample has increased by a factor of 8.6 wt% and 1.1 wt% for nitrogen and carbon, respectively (compared to amorphous TiO<sub>2</sub> nanotubes sample (E1)). When amorphous TiO<sub>2</sub> nanotubes sample was reduced in DMF-TBAP solution and annealed at 280°C in nitrogen atmosphere for the same duration both concentrations increased by a factor of 5.4 wt% and 1.0 wt% for nitrogen and carbon, respectively (see table 3.8(E4)).

The TiO<sub>2</sub> nanotubes sample (E7) that was reduced photochemically in methanol showed an increase in concentration of nitrogen and carbon by a factor of 2.3 wt% and 1.0 wt%, respectively (relative to amorphous TiO<sub>2</sub> nanotubes sample). However, upon annealing the reduced sample (E7) in nitrogen atmosphere at 280°C the concentration of nitrogen and carbon increased by a factor of 5.0 wt% and 1.0 wt%, respectively (compared to amorphous TiO<sub>2</sub> nanotubes sample, see table 3.8(E6)).

When sample E2 was photochemically reduced in methanol it showed a decrease of nitrogen concentration by a factor of 1.7 wt% and increase of carbon concentration by a factor of 1.5 wt% compared to sample E2 in table 3.8.

### **3.8 Photocatalytic efficiency measurements.**

These results are only very qualitative because the particle size, specific surface areas and pore size were not measured for TiO<sub>2</sub> nanotubes. The photocatalytic activity of TiO<sub>2</sub> depends on its phase structure, crystallite size, specific surface areas and pore structure. Moreover, photocatalytic activity is increased with decreasing particle size [218]. Degussa P25 consists of a mixture of 4:1 anatase to rutile crystalline forms and has particle size (26 nm), crystallite size (21 nm), surface area (56 m<sup>2</sup>/g) and pore volume (0.25 cm<sup>3</sup>/g).



However, TiO<sub>2</sub> nanotube shows higher photocatalytic activity than Degussa P25 despite the particle size and other mentioned factors. The TiO<sub>2</sub> nanotubes sample that was reduced in ACN-TBAP solution and annealed at 280°C in nitrogen atmosphere was used for photocatalytic activity test since it has the highest amount of dopant, see table 3.8(E5).

Anatase is generally regarded as the more photochemically active phase of titanium dioxide, possibly due to the combined effect of lower rates of recombination (of electrons and holes) and higher surface adsorption of light. Despite the fact that the band gap of rutile is smaller than that of anatase, pure phase rutile is photo-catalytically inactive [218]. The photocatalytic efficiency of the TiO<sub>2</sub> nanotube sample was compared with that of Degussa P25.

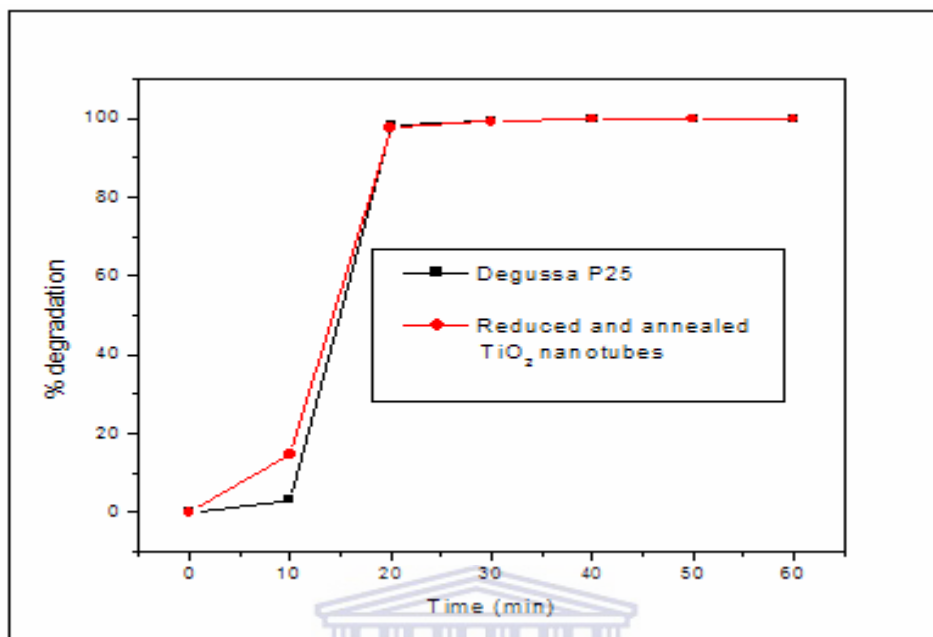


**Figure 3.33** Degussa P25 (TiO<sub>2</sub>) vs. TiO<sub>2</sub> nanotubes in 10 ppm of methylene blue (MB) solution under irradiation of UV.

UNIVERSITY of the  
WESTERN CAPE

Upon UV irradiation, both TiO<sub>2</sub> nanotubes and Degussa P25 (TiO<sub>2</sub>) degrade 100% of 10 ppm MB within 20 minutes, see figure 3.33.

There was remarkable change when the reactions were performed in sunlight. TiO<sub>2</sub> nanotubes show higher photocatalytic activity for first hours when reaction was exposed to sunlight and degradation of MB solution reaches maximum within 3 hours, as shown in figure 3.34. The results show more photo-response (in sunlight) of TiO<sub>2</sub> nanotubes than Degussa P25. This may attributed to the reduced band gap and large surface area which leads to an improvement in efficiency.

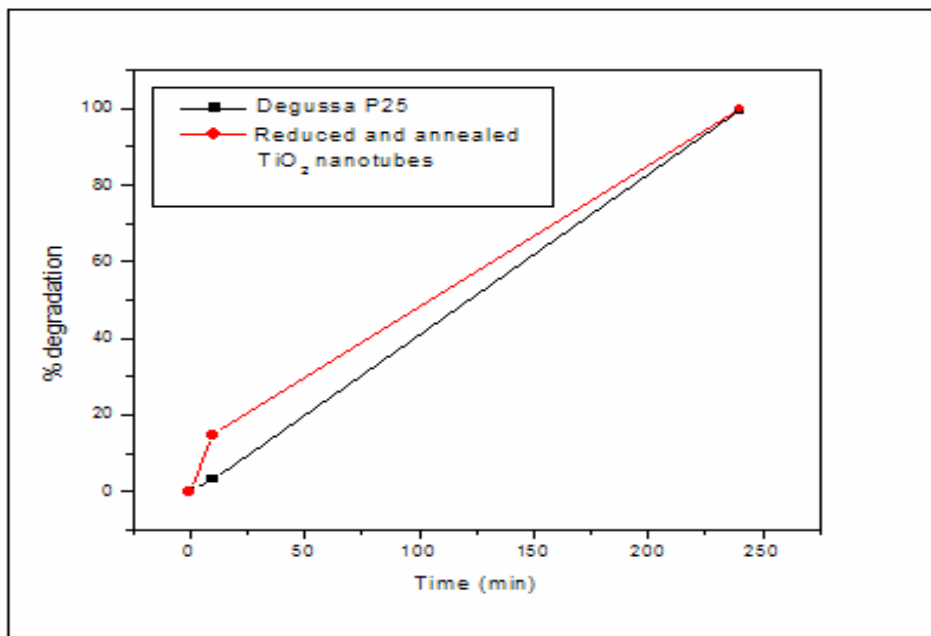


**Figure 3.34** Degussa P25 (TiO<sub>2</sub>) vs. TiO<sub>2</sub> nanotubes in 10 ppm of methylene blue solution exposed to sunlight for 3 hours.

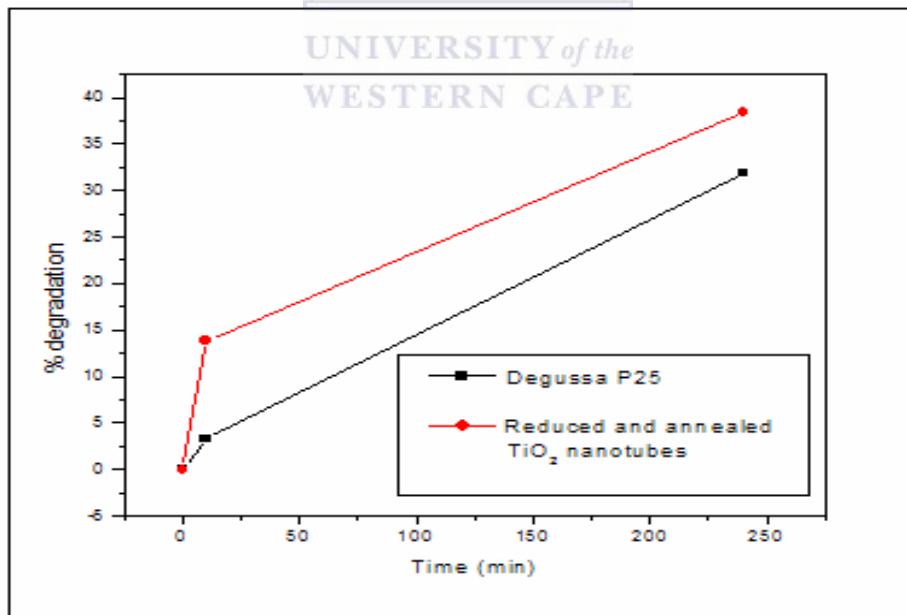


**Figure 3.35** Degussa P25 (TiO<sub>2</sub>) Vs TiO<sub>2</sub> nanotubes in 50 ppm of methylene blue solution expose to sunlight for 3 hours.

The TiO<sub>2</sub> nanotube shows significantly more degradation of 50 ppm MB compared to that when using Degussa P25 during 3 hours irradiation (sunlight) experiments, as shown in Fig 4.35. Reduced TiO<sub>2</sub> nanotubes have a greater photocatalytic activity compared to Degussa P25. Moreover, the reduced TiO<sub>2</sub> nanotubes produce a more efficient oxidative environment than Degussa P25 possibly due to the narrowed band gap.



# CHAPTER 4

## Conclusion

An electrolytic cell for the preparation of TiO<sub>2</sub> nanotubes was successfully designed and constructed. The electrolytic conditions required to reproducibly prepare TiO<sub>2</sub> nanotubes were established. The apparatus was successfully modified to prepare nanotubes on the circular face of a cylindrical titanium rod which was then used to study the nanotubes using cyclic voltammetry.

SEM and TEM studies established the morphology of the nanotubes as vertically orientated arrays relative to the plain of the titanium metal face on which they were prepared. The nanotubes are closed on the array face adjacent to the metal and open ended on the opposite array face. The nanotubes are between 35-50 μm long with constant internal diameter of 98 nm and the wall thickness of 21 nm.

The as grown nanotubes are yellowish white in colour and consist of amorphous TiO<sub>2</sub>. Upon calcination at 280°C they become crystalline adopting the anatase structure. The colours of the nanotubes vary according to the atmosphere used in calcination. In oxygen, nitrogen, argon and air they become white, dark grey to blue, grey blue and grey yellow in colours, respectively.

CV studies established a positive correlation between crystallinity and conductivity. Conductivity increases are associated with surface state intermediate levels in the band gap of TiO<sub>2</sub>. Doping by carbon and nitrogen was established by elemental analysis, XPS and RBS. Doping appears to reduce the width of the band gap but only to a small extent.

Reduction of the TiO<sub>2</sub> nanotubes either photochemically or electrochemically turns the nanotubes blue in colour but they appear to maintain their nanotube arrays morphology. The blue colour is associated with reduced valance states of titanium ( $Ti^{4+} \rightarrow Ti^{3+} \rightarrow Ti^{2+}$ ) which in turn increase the conductivity of TiO<sub>2</sub> and its reactivity with nitrogen as seen by increased nitrogen doping.

This study has established that TiO<sub>2</sub> nanotubes can be prepared using relatively easily method in the laboratory for further investigation. Reduction of the TiO<sub>2</sub> nanotubes does affect the nanotube morphology and hence provides a reduced TiO<sub>2</sub> nanotubes structure which is more conductive and reactive than TiO<sub>2</sub> powders. This combination of properties has the potential to be used advantageously to improve the photocatalytic efficiency of TiO<sub>2</sub> when using visible light.



# REFERENCES

- [1] M. Adachi, Y. Murata, M. Harada, Y. Yoshikawa, *Chem.Lett.*, **29** (2000) 942.
- [2] S. Z. Chu, S. Inoue, K. Wada, D. Li, H. Haneda, S. Awatsu, *J.Phys.Chem.*, B **107** (2003) 6586.
- [3] S. Uchida, R. Chiba, M. Tomiha, N. Masaki, M. Shirai, *Electrochem.*, **70** (2002) 418.
- [4] M. Adachi, Y. Murata, I. Okada, Y. Yoshikawa, *J.Electrochem.Soc.*, **150** (2003) G48.
- [5] G. K. Mor, K. Shankar, M. Paulose, O. K. Varghese, C. A. Grimes, *NanoLett.*, **6** (2006) 215.
- [6] M. Paulose, K. Shankar, O.K. Varghese, G. K. Mor, B. Hardin, C. A. Grimes, *Nanotech.*, **17** (2006) 1.
- [7] O. K. Varghese, D. Gong, M. Paulose, K. G. Ong, E. C. Dickey, C. A. Grimes, *Adv.Mater.*, **15** (2003) 624.
- [8] G. K. Mor, M. A. Carvalho, O. K. Varghese, M. V. Pishko, C. A. Grimes, *J.Mater.Res.*, **19** (2004) 628.
- [9] O. K. Varghese, G. K. Mor, C. A. Grimes, M. Paulose, N. Mukherjee, *J.Nanosci.Nanotechnol.*, **4** (2004) 733.
- [10] M. Paulose, O. K. Varghese, G. K. Mor, C. A. Grimes, K. G. Ong, *Nanotech.*, **17** (2006) 398.
- [11] B. O'Regan, M. Grätzel, *Nature*, **353** (1991) 737.
- [12] J. M. Macak, P. Schmuki, *Electrochimica Acta.*, **52** (2006) 1258.
- [13] S. Livraghi, A. Votta, M. C. Paganini, E. Giamello, *Chem.Commun.*, **4** (2005) 498.
- [14] A. Hagfeldt, M. Grätzel, *Acc.Chem.Res.*, **33** (2000) 269.
- [15] I. Onal, S. Soyer, S. Senkan, *Surf.Sci.*, **600** (2006) 2457.
- [16] S. J. Culp, F. A. Beland, *J.Am.Coll.Toxicol.*, **15** (1996) 219.
- [17] O. K Varghese, M. Paulose, T. J. LaTempa, C. A. Grimes, *NanoLett.*, **9** (2009) 731.
- [18] D. F. Ollis, H. Al-Ekabi., *Photocatalytic Purification and Treatment of Water and Air* (Elsevier, Amsterdam, 1993).
- [19] G. K. Mor, K. Shankar, M. Paulose, O. K. Varghese, C. A. Grimes, *NanoLett.*, **5** (2005) 191.
- [20] S. K. Mohapatra, M. Misra, V. K. Mahajan, K. S. Raja, *J.Phy.Chem.*, C **111** (2007) 8677.

- [21] A. Mills, R. H. Davies, D. Worsely, *Chem.Soc.Rev.*, **22** (1993) 417.
- [22] G. Munuera, J. P. Espinos, A. Fernandez, P. Malet, A. R. Gonzalez, *J.Chem.Soc.Faraday Trans.*, **86** (1990) 3441.
- [23] N. N. Lichtin, M. Avudaithai, *Res.Chem.Intermed.*, **20** (1994) 755.
- [24] K. Kalyanasundaram, M. Grätzel, *Coordination Chem. Rev.*, **117** (1998) 347.
- [25] A. Salomonsson, *New materials for gas sensitive field-effect device studies*, Dissertation No. 957 (2005)
- [26] A. L. Linsebigler, G. Lu, J. T. Yates, *Chem.Rev.*, **95** (1995) 735
- [27] H. Tang, K. Prasad, R. Sanjines, P. E. Schmid, F. Levi, *J.Appl.Phys.*, **75** (1994) 2042.
- [28] J-G. Li, T. Ishigaki, X. Sun, *J.Phys.Chem., C* **111** (2007) 4969.
- [29] <http://ruby.colorado.edu/~smyth/min/tio2.html>, 15/12/2009.
- [30] D. Y. Lee, W. J. Lee, J. S. Song, J. H. Koh, Y. S. Kim, *Comp.Mat.Sci.*, **30** (2004) 383.
- [31] L. Forro, O. Chauvet, D. Emin, L. Zuppiroli, H. Berger, F. Levy, *J.Appl.Phys.*, **75** (1994) 633.
- [32] D. Reyes-Coronado, G. Rodríguez-Gattorno, M. E. Espinosa-Pesqueira, C. Cab, R. de Coss, G. Oskam, *Nanotechn.*, **19** (2008) 145605.
- [33] N. Martin, C. Rousselot, D. Rondot, F. Palmino, R. Mercier, *Thin Solid Films*, **300** (1997) 113.
- [34] L. Vayssiers, *on solar hydrogen and nanotechnology*, (2009).
- [35] G. Campet, A. Deshayes, J. C. Frison, N. Treuil, J. Portier, *Active and Passive Elec. Comp.*, **21** (1998) 123.
- [36] V. S. Bagotsky, *fundamental of electrochemistry*, (2<sup>nd</sup> edition, 2005).
- [37] L. Kronik, Y. Shapira, *Surf.Interface Anal.*, **31** (2001) 954.
- [38] J. S. Yuan, J. J. Liou, *Semiconductor device physics and simulation* (2<sup>nd</sup> edition, 1998).
- [39] S. Na-Phattalung, M. F. Smith, K. Kim, M. H. Du, S. H. Wei, S. B. Zhang, S. Limpijumnong, *Phys.Rev.*, B **73** (2006) 125205.
- [40] A.V. da Rosa, *Fundamentals of renewable energy processes*, (2<sup>nd</sup> edition, 2009).
- [41] M. M. Halmann, *Photodegradation of water pollutants*, (1995)
- [42] K. T. Ranjit, B. Vishwanathan, *Ind.J.Chem.*, A **35** (1996) 443.
- [43] M. R. Hoffmann, S. T. Martin, W. Choi, D. W. Bahnemann, *Chem.Rev.*, **95** (1995) 69.

- [44] M. Schiavello, *Electrochem. Acta.*, **38** (1993) 11.
- [45] T. L. Villarreal, P. Bogdanoff, P. Salvador, N. Alonso-Vante, *Sol. Energy Mat. Sol. Cells*, **83** (2004) 347.
- [46] J. A. Navio, R. I. Bickley, *Surface and intersurface analysis*, **22** (1994) 417.
- [47] A. Mills, R. Davies, *J. Photochem. Photobiol. A: Chem.*, **85** (1995) 173.
- [48] <http://www.pestbegone.net/products/m-3.htm>, 15/12/2009
- [49] A. J. Bard, *Science*, **207** (1980) 139.
- [50] M. Schiavello, *Ed. Photocatalysis and Environment*; (Kluwer Academic Publishers: Dordrecht, 1988).
- [51] A. Fujishima, K. Honda, *Nature*, **37** (1972) 238.
- [52] A. J. Bard, *J. Phys. Chem.*, **86** (1982) 172.
- [53] M. Gärtzel, *Ed. Energy Resource through photochemistry and Catalysis*, (Academic Press: New York., 1983).
- [54] K. Kalyanasundaram, M. Gärtzel, E. Pelizzetti, *Coord. Chem. Rev.*, **69** (1986) 57.
- [55] N. Serpone, E. Pelizzetti, *Photocatalysis: Fundamentals and Applications*, (Wiley, New York, 1989).
- [56] E. Pelizzetti, M. Schiavello, *Eds Photochemical Conversion and Storage of Solar Energy*, (Kluwer Academic Publishers: Dordrecht, 1991).
- [57] J. J. Pietron, D. R. Rolison, *J. Non-Cryst. Solids*, **350** (2004) 107.
- [58] V. Štengl, S. Bakardjieva, J. Šubrt, L. Szatmary, *Microporous Mesoporous Mater.*, **91** (2006) 1.
- [59] C. Kormann, D. W. Bahnemann, M. R. Hoffmann, *J. Phys. Chem.*, **92** (1988) 5186.
- [60] M. Schiavello, H. Dordrecht, *Photoelectrochemistry, Photocatalysis, and Photoreactors: Fundamentals and Developments*, (Kluwer Academic Publishers, Boston, MA., 1985).
- [61] K. M. Reddy, S. V. Manorama, A. R. Reddy, *Mater. Chem. Phys.*, **78** (2002) 239.
- [62] M. Radecka, M. Rekas, A. Trenczek-Zajac, K. Zakrzewska, *Journal of Power Sources*. **181** (2008) 46.
- [63] A. Gilbert, J. Baggott, *Essentials of Molecular Photochemistry*; CRC Press: Boca Raton, (1991)

- [64] H. Gerischer, *J.Electroanal.Chem.*, **58** (1975) 263.
- [65] A. J. Bard, *J.Photochem.*, **10** (1980) 59.
- [66] X. Zhang, J. Wen, C. Sun, *Appl.Phys.*, A **76** (2003) 261.
- [67] D. F. Ollis, *Cat.Tech.*, **2** (1998) 149.
- [68] R. W. Matthews, *J.Phys.Chem.*, **91** (1987) 3328.
- [69] A. Fujishima, K. Hashimoto, T. Watanabe, *TiO<sub>2</sub> Photocatalysis: Fundamentals and Applications*, (BKC, Inc., Tokyo, 1999).
- [70] A. Fujishima, T. N. Rao, *Pure and Appl.Chem.*, **70** (1998) 2177.
- [71] A. Fujishima, T. N. Rao, D. A. Tryk, *Photochem.Photobiol. C:Photochem.Rev.*, **1** (2000) 1.
- [72] N. G. Schrauzer, N. Strampach, L. N. Hui, R. Palmer, J. Salehi, *Proc.Natl.Acad.Sci.*, **80** (1983) 3873.
- [73] G. N. Schrauzer, T. D. Guth, *J.Am.Chem.Soc.*, **99** (1977) 7189.
- [74] W. Li, Y. Wang, H. Lin, S. I. Shah, C. P. Huang, D. J. Doren, S. A. Rykov, J. G. Chen, M. A. Barteau, *Appl.Phys.Lett.*, **83** (2003) 4143.
- [75] M. Gratzel, *J.Photochem.Photobiol. A—Chem.*, **164** (2004) 3.
- [76] M. Gratzel, *App.Phys.*, **421** (2003) 586.
- [77] M. Gratzel, *Electrochem.*, **70** (2002) 397.
- [78] D. Dvoranova, V. Brezova, M. Mazur, M. A. Malati, *Appl.Catal. B-Environ.*, **37** (2002) 91.
- [79] K. Wilke, H. D. Breuer, *J.Photochem.Photobiol. A-Chem.*, **121** (1999) 49.
- [80] K. Wilke, H. D. Breuer, *Phys.Chem.-Int. J.Res.Phys.*, **213** (1999) 135.
- [81] J-M. Herrmann, J. Disdier, P. Pichat, *Chem.Phys.Lett.*, **108** (1984) 618.
- [82] W. Y. Choi, A. Termin, M. R. Hoffmann, *J.Phys.Chem.*, **98** (1994) 13669.
- [83] S. Sakthivel, H. Kisch, *Chem.Int.Ed.*, **42** (2003) 4908.
- [84] R. P. Vitiello, J. M. Macak, A. Ghicov, H. Tsuchiya, L. F. P. Dick, P. Schmuki, *Electrochem.Comm.*, **8** (2006) 544.
- [85] A. Ghicov, J. M. Macak, H. Tsuchiya, J. Kunze, V. Haeublein, L. Frey, P. Schmuki, *Nano.Lett.*, **6** (2006) 1080.
- [86] G. K. Mor, O. K. Varghese, M. Paulose, K. Shankar, C. A. Grimes, *Sol. Energy Mater. Sol. Cells*, **90** (2006) 2011.

- [87] K. Noworyta, J. Augustynski, *Solid State Lett.*, **7** (2004) E31.
- [88] Y. Xie, *Electrochim.Acta.*, **51** (2006) 3399.
- [89] L. Lin, W. Lin, Y. Zhu, B. Zhao, Y. Xie, *Chem.Lett.*, **34** (2005) 284.
- [90] M. I. Litter, J. A. Navio, *J.Photochem.Photobiol.*, **98** (1996) 171.
- [91] M. A. Fox, M.T. Dulay, *Chem.Rev.*, **93** (1993) 341.
- [92] R. Asahi, T. Morikawa, T. Ohwaki, K. Aoki, Y. Taga, *Science*, **293** (2001) 269.
- [93] T. Morikawa, R. Asahi, T. Ohwaki, K. Aoki, Y. Taga, *J.Appl.Phys.Lett.*, **40** (2001) L561.
- [94] X. B. Chen, Y. B. Lou, A. C. S. Samia, C. Burda, J. L. Gole, *Adv.Funct.Mater.*, **15** (2005) 41.
- [95] P. G. Wu, C. H. Ma, J. K. Shang, *Appl.Phys., A* **81** (2005) 1411.
- [96] Y. Suda, H. Kawasaki, T. Ueda, T. Ohshima, *Thin Solid Films*, **475** (2005) 337.
- [97] H. Irie, S. Washizuka, Y. Watanabe, T. Kako, K. Hashimoto, *J.Electrochem.Soc.*, **152** (2005) E351.
- [98] S. Sato, R. Nakamura, S. Abe, *Appl.Catal. A-Gen.*, **284** (2005) 131.
- [99] K. Shankar, K. C. Tep, G.K. Mor, C. A. Grimes, *J.Phys. D: Appl.Phys.*, **39** (2006) 2361.
- [100] V. M. Khomenko, K. Langer, H. Rager, A. Fett, *Phys.Chem.Miner.*, **25** (1998) 338.
- [101] V. E. Henrich, G. Dresselhaus, H. J. Zeiger, *Phys.Rev.Lett.*, **36** (1976) 1335.
- [102] R. L. Kurtz, R. Stock-Bauer, T. E. Madey, *Surf.Sci.*, **218** (1989) 178.
- [103] M. Nolan, S. D Elliot, J. S Mulley, R. A. Bennet, M. Basham, P. Mulheran, *Phys.Rev., B* **77** (2008) 235424.
- [104] M. A. Henderson, W. S. Epling, C. H. F. Peden, C. L. Perkins, *J.Phys.Chem., B* **107** (2003) 534.
- [105] E. Serwicka, M. W. Schierkamp, R. N. Z. Schindler, *Naturforsch.*, **36a** (1981) 226.
- [106] P. F. Chester, *J. Appl. Phys.*, **32** (1961) 2233.
- [107] T. Sekiya, T. Yagisawa, N. Kamiya, D. D. Mulmi, S. Kurita, Y. Murakami, T. Kodaira, *J.Phys.Soc.Jpn.*, **73** (2004) 703.
- [108] J. Nerlov, S. V. Christensen, S. Wichel, E. H. Pedersen, P. J. Møller, *Surf.Sci.*, **371** (1997) 321.
- [109] P. Le Fe`vre, J. Danger, H. Magnan, D. Chandesris, J. Jupille, S. Bourgeois, M-A. Arrio, R. Gotter, A. Verdini, A. Morgante, *Phys.Rev., B* **69** (2004) 155421.

- [110] A. G. Thomas, W. R. Flavell, A. R. Kumarasinghe, A. K. Mallick, D. Tsoutsou, G. C. Smith, R. Stockbauer, S. Patel, M. Grätzel, R. Hengerer, *Phys.Rev.*, B **67** (2003) 035110.
- [111] P. Krüger, S. Bourgeois, B. Domenichini, H. Magnan, D. Chandesris, P. Le Fe`vre, A. M. Flank, J. Jupille, L. Floreano, A. Cossaro, A. Verdini, A. Morgante, *Phys.Rev.Lett.*, **100** (2008) 055501.
- [112] R. F Howe, M. Grätzel, *J.Phys.Chem.*, **89** (1985) 4495.
- [113] R. P. Müller, J. Steinle, H. P. Boehm, *Z.Naturforsch.*, **45b** (1990) 864-870.
- [114] P. Pichat, J. Herrman, J. Disdier, M. Mozzanega, *J.Chem.*, **5** (1981) 627.
- [115] J. F. Houlihan, R. J. Pollock, *Electrochimica Acta.*, **28** (1983) 585.
- [116] Y. Wada , A. Morikawa, *Bull.Chem.Soc.*,**60** (1987) 3509.
- [117] S. Yagmagata, S. Nakalayashi, K. M. Sancier, A. Fujishima, *Bull.Chem.Soc.Jpn.*, **93** (1988) 267.
- [118] K. Iseda, *Chem.Express*, **5** (1990) 729.
- [119] K. Iseda, *Bull.Chem.Soc.Jpn.*, **64** (1991) 1160.
- [120] U. Kaluza, *Doctoral thesis, Univ,Heidelberg.*(1969); J. Steninle, *Doctoral thesis , Univ münchen* (1974).
- [121] D. Bahnemann, A. Henglien, J. Lilie, L. Spanhel, *J.phys.Chem.*, **88** (1984) 709.
- [122] R. S Davidson, C. L. Morrison, J. Abraham, *J.Photochem.*, **24** (1984) 27.
- [123] L. F. Schneemeyer, M. S. Wrighton, A. Stacy, M. J. Sienko, *Appl.Phys.Lett.*, **36** (1980)701
- [124] N. S. Lewis, M. S. Wrighton, *J. Phys. Chem.*, **88** (1984) 2009.
- [125] C. G. Zoski, *Handbook of electrochemistry*, (1<sup>st</sup> edition, 2007).
- [126] L. Nadjjo, *J.Electroanal.Chem.*, **108** (1980) 29.
- [127] P. A. Kohl, A. J. Bard, *J.Am.Chem.Soc.*, **99** (1977) 7531.
- [128] D. Laser, A. J. Bard, *J.Phys.Chem.*, **80** (1976) 459.
- [129] S. N. Frank, A. J, Bard, *J.Am.Chem.Soc.*, **97** (1975) 7427.
- [130] P. A. Kohl, A. J. Bard, *J.Electrochem.Soc.*, **126** (1979) 1.
- [131] G. Redmond, D. Fitzmaurice, *J.Phys.Chem.*, **97** (1993) 1426.
- [132] P. Qu , G. J. Meyer, *Langmuir*, **17** ( 2001) 6720.

- [133] C. A. Kelly, F. Farzad, D. W. Thompson, J. M. Stipkala, G. J. Meyer, *Langmuir*, **15** (1999) 7047.
- [134] A. G. Mamalis, L.O.G. Vogtlander, A. Markopoulos, *Precision Engineering*, **28** (2004) 16
- [135] G. L Hornyak, H. F Tibbals, J. Dutta, J. J. Moore., *Introduction to nanocience and nanotechnology*,(2009)
- [136] S. Kaneco, Y. Chen, P. Westerhoff , J. C. Crittenden; *Scripta Materialia*. **56** (2007) 373.
- [137] A. L. Linsebigler, G. Lu Jr., J. T. Yatus, *J.Phys.Chem.*, **99** (1995) 7626.
- [138] P. Pillai, K. S. Raja, M. J. Misra, *Power Source*, **161** (2006) 524.
- [139] Y .Xie, *Nanotech.*, **17** (2006) 3340.
- [140] X. Zhang, B. Yao, L .Zhao, C. Liang, L. Zhang, Y. Mao, *J.Electrochem.Soc.*, **148** (2001) G398.
- [141] S. J. Limmer, T. P. Chou, G. Z. Cao, *J.Mater.Sci.*, **39** (2004) 895.
- [142] S. Yoo, S. A. Akbar, K. H. Sandhage, *Adv.Mater.*, **16** (2004) 260.
- [143] M. Adachi, Y. Murata, I. Okada, S. Yoshikawa, *J.Electrochem.Soc.*, **150** (2000) G488.
- [144] Y.C. Zhu, H.L. Li, Y. Koltypin, Y. R. Hachon, A. Gedanken, *Chem.Commun.*, **24** (2001) 2616.
- [145] T. Y. Peng, A. Hasegawa, J. R. Qiu, K. Hirao, *Chem.Mater.*, **15** (2003) 2011.
- [146] H. Tsuchiya, J. M. Macak, L. Taveira, E. Balaur, A. Ghicov, K. Sirotna, P. Schmuki, *Electrochem.Comm.*,**7** (2005) 576.
- [147] K. Zhu, N. R. Neale, A. Miedaner, A. J. Frank, *NanoLett.*, **7** (2007) 69.
- [148] M. Adachi, Y. Murata, J. Takao, J. Jiu, M. Sakamoto, F. Wang, *J.Am.Chem.Soc.*, **126** (2004) 14943.
- [149] Z. Miao, D. S. Xu, J. H. Ouyang, G. L. Guo, X. S. Zhao, Y. Q. Tang, *NanoLett.*, **2** (2002) 717.
- [150] M. Paulose, G. K. Mor, O. K. Varghese, K. Shankar, C. A. Grimes, *J.Photochem.Photobio. A: Chem.*, **178** (2006) 8.
- [151] V. P. Parkhutik , V. I. Shershulsky, *J.phys.D:Appl.Phys.*, **25** (1992) 1258.
- [152] D. W. Gong, C. A Grimes, O. K Varghese, W. Hu, R. S. Singh, Z. Chen, E.C. Dickey, *J.Mater.Res.*, **16** (2001) 3331.
- [153] X. Liu, P. K. Chu, C. Ding, *Mater.Sci.Eng.*, R **47** (2004) 49.

- [154] R. Chiesa, E. Sandrini, M. Santin, G. Rondelli, A. Cigada, *J.App.Biomater. Biomechanics*, **1** (2003) 91.
- [155] N. K. Kuromoto , R. A. Simão , G. A. Soares , *Mater. Characterization*, **58** (2007) 114
- [156] G.K. Mor, O. K. Varghese, M. Paulose, N. Mukherjee, C. A. Grimes, *J.Mater.Res.*, **18** (2003) 2588.
- [157] Q. Cai, M. Paulose, O.K. Varghese, C.A. Grimes, *J.Mater.Res.*, **20** (2005) 230.
- [158] K. Shankar, M. Paulose, G.K. Mor, O.K. Varghese, C.A. Grimes, *J.Phys. D: Appl.Phys.*, **38** (2005) 3543.
- [159] K. Shankar, K. C. Tep, G. K. Mor, C.A. Grimes, *J.Phys.*, D **39** (2006) in press.
- [160] C. Ruan, M. Paulose, O. K. Varghese, G. K. Mor, C.A. Grimes, *J.Phys.Chem.*, B **109** (2005) 15754.
- [161] J. M. Macak, H. Tsuchiya, P. Schmuki, *Angew.Chem.Int.Ed.*, **44** (2005) 2100.
- [162] J. M. Macak, K. Sirotna, P. Schmuki, *Electrochim.Acta.*, **50** (2005) 3679.
- [163] L. V. Taveira, J. M. Macak, H. Tsuchiya, L. F. P. Dick, P. Schmuki, *J.Electrochem.Soc.*, **152** (2005) B405.
- [164] A. Ghicov, H. Tsuchiya, J.M. Macak, P. Schmuki, *Electrochem.Commun.*, **7** (2005) 505.
- [165] J.M. Macak, H. Tsuchiya, L. Taveira, S. Aldabergerova, P. Schmuki, *Angew.Chem.Int.Ed.*, **44** (2005) 7463.
- [166] M. Paulose, K. Shankar, S. Yoriya, H. E. Prakasam, O.K Varghese, G. K. Mor, T. A. Latempa, A. Fitzgerald, C. A. Grimes, *J.Phys.Chem.*, B **110** (2006) 16179.
- [167] G. Korotcenkov, *Mater.Sci.Eng.*, B **139** (2007) 1.
- [168] D. W. Gong, C. A. Grimes, O.K. Varghese, *J.Mater.Res.*, **16** (2001) 331.
- [169] S. Z. Chu, S. Inoue, K. Wada, S. Hishita, K. Kurashima, *J.Electrochem.Soc.*, **152** (2005) B116.
- [170] H. Masuda, K. Kanazawa, M. Nakao, A. Yokoo, T. Tamamura, T. Sugiura, H. Minoura, K. Nishio, *Adv.Mater.*, **15** (2003) 159.
- [171] J. E. Wijnhoven, W. Vos, *Science*, **281** (1998) 802.
- [172] W. Z. Wang, O. K. Varghese, M. Paulose, C. A. Grimes, *J.Mater.Res.*, **19** (2004) 417.

- [173] Z. R. Tian, J. A. Voigt, J. Liu, B. McKenzie, H. F. Xu, *J.Am.Chem.Soc.*, **125** (2003) 12384.
- [174] P. Hoyer, *Langmuir*, **12** (1996) 1411.
- [175] Y. S. Chen, J. C. Crittenden, S. Hackney, L. Sutter, D.W. Hand, *Environ.Sci.Technol.*, **39** (2005) 1201.
- [176] S. K. Mohapatra, V. K. Mahajan, M. Misra, *Nanotech.*, **18** (2007) 445705.
- [177] K. Shankar, G. K. Mor, H. E. Prakasam, S. Yoriya, M. Paulose, O. K. Varghese, C. A. Grimes, *Nanotech.*, **18** (2007) 065707.
- [178] P. V. Kamath, M. F. Ahmed, *J.App.Electrochem.*, **23** (1993) 225.
- [179] E. S. Steigerwalt, G. A. Deluga, D. E. Cliffel, C. M. Lukehart, *J.Phys.Chem.*, **105** (2001) 8097.
- [180] M. T. Postek, K. S. Howard, A. H. Johnson, K. L. McMicheal, *Scanning Electron Microscopy: A Student 's Handbook*, M. T. Postek Jr. and Ladd Research Industries, Inc., 1980.
- [181] P. Kubelka, F. Munk, *Z.Tech.Phys.*, **12** (1931) 593.
- [182] L. Yang, B. Kruse, *J.Opt.Soc.Am.*, **A 21** (2004) 1933.
- [183] J.F. Moulder, W.F. Stickle, P.E. Sobol, K.D. Bomben, *Handbook of X-ray Photoelectron Spectroscopy*, ed. J. Chastain, Perkin-Elmer Corp., Minnesota (1979).
- [184] D. Briggs, M.P. Seah, *Practical Surface Analysis vol 1: Auger and X-ray Photoelectron Spectroscopy*, John Wiley and Sons, Chichester (1990)
- [185] R. Asmatulu, A. Karthikeyan, D. C. Bell, S. Ramanathan, M. J. Aziz, *J.Mater.Sci.*, **44** (2009) 4613.
- [186] G. Patermarakis, H.S. Karayannis, *Electrochim.Acta.*, **40** (1995) 2647.
- [187] D.D. Macdonald, *J.Electrochem.Soc.*, **140** (1993) L27.
- [188] J. W. Diggle, T. C. Downie, C. W. Goulding, *Electrochim.Acta.*, **15** (1970) 1079.
- [189] G. C. Wood, J.P. O'Sullivan, *Electrochim.Acta.*, **15** (1970) 1865.
- [190] G. Patermarakis, P. Lenas, G. Papayiannis, *Electrochim.Acta.*, **36** (1991) 709.
- [191] A. P. Li, F. Müller, A. Birner, K. Nielsch, U. Gösele, *J.Appl.Phys.*, **84** (1998) 6023.
- [192] O. Jessensky, F. Müller, U. Gösele, *Appl.Phys.Lett.*, **72** (1998) 1173.

- [193] V. Zwilling, E. Darque-Ceretti, A. Boutry-Forveille, D. David, M. Y. Perrin, M. Aucouturier, *Surf.Interface Anal.*, **27** (1991) 629.
- [194] J.-L. Delplancke, R. Winand, *Electrochim.Acta.*, **33** (1988) 1551.
- [195] Y-T. Sul, C.B. Johansson, Y. Jeong, T. Albrektsson, *Med.Eng.Phys.*, **23** (2001) 329.
- [196] B. J. Hwang, J. R. Hwang, *J.Appl.Electrochem.*, **23** (1993) 1056.
- [197] J. Siejka, C. Ortega, *J. Electrochem. Soc.: Solid State Sci.Technol.*, **124** (1977) 883.
- [198] G. E. Thompson, *Thin Solid Films*, **192** (1997) 297.
- [199] M. M. Lohregel, *Mat.Sci.Eng. R: Report.*, **11** (1993) 243.
- [200] N. Khalil, J. S. Leach, *Electrochim.Acta.*, **31** (1986) 1279.
- [201] U. Diebold, *Appl.Phys.*, A **76** (2003) 681.
- [202] M. C. Buzzeo, C. Hardacre, R. G. Compton, *Chem.Phys.Chem.*, **7** (2007) 176.
- [203] G. Boschloo, D. Fitzmaurice, *J.Phys.Chem.*, B **103** (1999) 7860.
- [204] S. H. Kang, J-Y. Kim, Y. Kim, H. S. Kim, Y-E. Sung, *J.Phys.Chem.*, C **111** (2007) 9614.
- [205] U. Diebold, J. Lehman, T. Mahmoud, M. Kuhn, G. Leonardelli, W. Hebenstreit, M. Schmid, P. Varga, *Surf.Sci.*, **411** (1998) 137.
- [206] A. Ghicov, H. Tsuchiya, J. M. Macak, P. Schmuki, *Phys.Stat.Sol.*, **203** (2006) R28.
- [207] P. Xiao, D. Liu, B. B. Garcia, S. Sepehri, Y. Zhang, G. Cao, *Sensors and Actuators*, B **134** (2008) 367.
- [208] G. Tamir, B-D. Moti, K. Itshak, S. Raya, R. A. Ze'ev, B-J. Eshel, H. Yael, *Nanotech.*, **18** (2007) 035201.
- [209] A. B Murphy, *Solar energy materials and solar cells*, **91** (2007) 1326.
- [210] J. I. Pankove, *Optical Processes in Semiconductors*, (Dover, NewYork, 1971).
- [211] C. R. Aita, Y-L. Liu, M. L. Kao, S. D. Hansen, *J.Appl.Phys.*, **60** (1986) 749.
- [212] R. Wang, N. Sakai, A. Fujishima, T. Watanabe, K. Hashimoto, *J.Phys.Chem.*, B **103** (1999) 2188.
- [213] M. Takeuchi, Y. Onozaki, Y. Matsumura, H. Uchida, T. Kuji, *Nuclear Instrum. Meth.Phys.Res.*, B **206** (2003) 259.
- [214] D. Mardare, D. Luca, C-M. Teodorescu, D. Macovei, *Surf.Sci.*, **601** (2007) 4515.
- [215] L. Lei, Y. Su, M. Zhou, X. Zhang, X. Chen, *Mater.Res.Bull.*, **42** (2007) 2230.

- [216] S. Jian, L. Jun, C. Yun-Fa, *Acta Phys.Chim.Sin.*, **24** (2008) 1283.
- [217] D. C. Hurum, A. G. Agrios, K. A. Gray, *J.Phys.Chem., B* **107** (2003) 4545.
- [218] K. Joseph Antony Raj, B. Viswanathan, *Ind.J.Chem., A* **48** (2009) 1378.

